

Pure crystal phase nanowires : growth and optical properties

Citation for published version (APA):

Assali, S. (2015). *Pure crystal phase nanowires : growth and optical properties*. [Phd Thesis 1 (Research TU/e / Graduation TU/e), Applied Physics and Science Education]. Technische Universiteit Eindhoven.

Document status and date:

Published: 01/09/2015

Document Version:

Publisher's PDF, also known as Version of Record (includes final page, issue and volume numbers)

Please check the document version of this publication:

- A submitted manuscript is the version of the article upon submission and before peer-review. There can be important differences between the submitted version and the official published version of record. People interested in the research are advised to contact the author for the final version of the publication, or visit the DOI to the publisher's website.
- The final author version and the galley proof are versions of the publication after peer review.
- The final published version features the final layout of the paper including the volume, issue and page numbers.

[Link to publication](#)

General rights

Copyright and moral rights for the publications made accessible in the public portal are retained by the authors and/or other copyright owners and it is a condition of accessing publications that users recognise and abide by the legal requirements associated with these rights.

- Users may download and print one copy of any publication from the public portal for the purpose of private study or research.
- You may not further distribute the material or use it for any profit-making activity or commercial gain
- You may freely distribute the URL identifying the publication in the public portal.

If the publication is distributed under the terms of Article 25fa of the Dutch Copyright Act, indicated by the "Taverne" license above, please follow below link for the End User Agreement:

www.tue.nl/taverne

Take down policy

If you believe that this document breaches copyright please contact us at:

openaccess@tue.nl

providing details and we will investigate your claim.

Pure crystal phase nanowires: growth and optical properties

PROEFSCHRIFT

ter verkrijging van de graad van doctor aan de Technische Universiteit Eindhoven, op gezag van de rector magnificus, prof.dr.ir. F.P.T. Baaijens, voor een commissie aangewezen door het College voor Promoties, in het openbaar te verdedigen op dinsdag 1 september 2015 om 16.00 uur

door

Simone Assali

geboren te Reggio Emilia, Italië

Dit proefschrift is goedgekeurd door de promotoren en de samenstelling van de promotiecommissie is als volgt:

voorzitter: prof.dr.ir. G.M.W. Kroesen
1e promotor: prof.dr. E.P.A.M. Bakkers
copromotor(en): dr. J.E.M. Haverkort
leden: prof.dr. L. Samuelson (Lund University)
prof.dr. C. Ronning (University of Jena)
prof.dr. A. Fiore
prof.dr. J. Arbiol (Universitat de Barcelona)
prof.dr. A. Meijerink (UU)

A catalogue record is available from the Eindhoven University of Technology Library.

Pure crystal phase nanowires: growth and optical properties, by Simone Assali

ISBN: 978-90-386-3892-8

The work described in this thesis has been carried out in the group of Photonics and Semiconductor Nanophysics, at the Department of Applied Physics of the Eindhoven University of Technology, The Netherlands.

The research leading to the presented results has received funding from Dutch Organization for Scientific Research (NWO-VICI 700.10.441).

Printed by Ipskamp Drukkers.

Contents

1	Introduction	3
1.1	Nanowires	3
1.1.1	VLS growth	7
1.1.2	Growth regimes	8
1.1.3	Sidewall growth	8
1.2	Crystalline structure	9
1.2.1	Defects	9
1.2.2	WZ/ZB interfaces	10
1.3	Scope of this thesis	11
2	Calculated band structure of wurtzite GaP	13
2.1	Crystal Hamiltonian	13
2.1.1	First Brillouin zone of the ZB and WZ crystals	14
2.1.2	Band symmetry	14
2.2	Methods to calculate the band structure	15
2.2.1	Empirical pseudopotential method	15
2.2.2	Density functional theory	16
2.3	Zinc blende band diagram	17
2.4	Wurtzite band structure	17
2.4.1	Splitting of the valence band	18
2.4.2	Effective masses	18
2.4.3	Selection rules	19
2.4.4	Transition matrix elements	19
2.5	Excitons	22
2.5.1	Phonon modes	23
2.5.2	Bound excitons	24
2.6	Donor-Acceptor pairs	25
3	Experimental methods and techniques	27
3.1	Substrate patterning	27
3.1.1	Nanoimprint lithography	28
3.1.2	Electron beam lithography	29
3.1.3	Pre-growth substrate cleaning	29
3.2	Metalorganic vapor phase epitaxy	30

3.3	Scanning electron microscopy	32
3.4	Transmission electron microscopy	33
3.5	X-ray diffraction	36
3.6	Optical characterization techniques	37
3.6.1	Photoluminescence spectroscopy	37
3.6.2	Photoluminescence excitation spectroscopy	38
3.6.3	Optical setup overview	38
4	Growth and structural characterization of WZ GaP nanowires	41
4.1	Nanowire growth	42
4.1.1	Growth parameters	42
4.1.2	Uniformity of GaP nanowire arrays	42
4.2	Crystalline structure	43
4.2.1	Pure WZ crystal phase	43
4.2.2	Effect of the temperature on the SF density	44
4.2.3	HCl passivation	46
4.2.4	AlGaP shell	47
4.2.5	X-ray diffraction	50
5	Crystal phase control in GaP wires	51
5.1	Growth of WZ/ZB interfaces	51
5.2	Control of the ZB length	53
5.2.1	Effect of the Ga precursor	53
5.2.2	Approaching the ML control	56
5.3	Tuning the WZ growth	58
5.4	Nucleation model for the WZ and ZB growths	60
5.5	WZ/ZB superlattice	61
5.6	Conclusion and applications	64
6	Optical characterization of WZ GaP wires	65
6.1	Optical data: low excitation power (below 1 W/cm ²)	65
6.1.1	PL spectra	66
6.1.2	Time-resolved PL	67
6.2	Optical data: medium-high excitation power (above 1 W/cm ²)	69
6.2.1	Power series	69
6.2.2	Internal quantum efficiency and non-radiative efficiency	74
6.2.3	Phonon replicas	75
6.2.4	Lifetime of the exciton lines	75
6.2.5	PL in polarization	76
6.2.6	PL 3-100 K	77
6.2.7	PLE measurements on vertical and horizontal wires	79
6.3	Interpretation of the experimental results	82
6.3.1	Donor acceptor pair recombination	82
6.3.2	Burstein-Moss bandfilling	82
6.3.3	Bound exciton character of the A- and B-lines	83
6.3.4	Direct band gap excitonic character of the A-, B-, and C-lines	83
6.3.5	High internal quantum efficiency of the A- and C-lines	84

6.3.6	Free exciton nature of the C-line	84
6.3.7	Assignment of the A-, B-, and C-peaks	85
6.3.8	Discussion of the PLE spectra	85
6.3.9	Stokes shift	86
6.3.10	Transitions with the Γ_{7c} conduction bands	87
6.3.11	Polarization dependence in PL-PLE	87
6.4	Conclusion	88
7	Determination of the dielectric constant	89
7.1	Fabry-Pérot modes	89
7.2	Finesse and end facets reflectivity	90
7.3	Refractive index	93
7.4	Dielectric constant	94
8	Applications and outlook	95
8.1	On the road to green LEDs	95
8.1.1	Tunability of the optical emission	95
8.1.2	p-n junctions for LEDs	96
8.2	Solar water splitting	98
8.2.1	Behavior of a PEC cell	98
8.2.2	Nanowires versus substrate	101
8.3	Hexagonal Silicon	102
A	Appendix	105
A.1	Estimation of IQE and NRE	105
A.2	PL spectra showing the B-line	108
A.3	Additional PLE measurements	108
	References	109
	List of abbreviations	121
	Summary	123
	Acknowledgments	125
	List of publications	127
	Curriculum vitae	129

Chapter 1

Introduction

Thinner, lighter, and more powerful laptops, smartphones, and tablets are continuously supplied to the market, with a constant need for more efficient devices. Dissipation of heat is one of the limiting factors in the efficiency of the integrated circuits. To reduce this issue new architectures are proposed that require the development of transistors more compact in size. This trend follows Moore's law¹, which predicts that the number of transistors per square centimeter on integrated circuits should double every two year, achieving higher performances with a smaller amount of material. Thus, the transistors must be continuously reduced down in size with the development of nano-structures, where the dimensions are in the 10^{-9} m range. These structures are fabricated following two main routes. The *top-down* approach, consisting of a combination of lithographic and etching techniques, is used in the manufacturing process of the silicon technology, where transistors have been recently scaled down to 14 nm in size². The second fabrication route follows the *bottom-up* approach, where structures are assembled using atoms as building blocks. This approach allows, for instance, the synthesis of semiconductor nanowires (NWs).

1.1 Nanowires

In 1964, a method for the growth of *bottom-up* nanowires was discovered by Wagner and Ellis at Bell Labs, which was called the vapor-liquid-solid (VLS) growth mechanism, where three phases contribute in the nanowire growth³. This method was originally observed in the growth of silicon wires, and further developed from the early 1990s in many laboratories around the world⁴⁻⁷. By using this method, nanowires with diameters ranging from 5 to 100 nm and lengths up to few tens of microns are commonly grown, resulting in a very large aspect ratio, hence in a mono-dimensional (1D) structure. Band gap engineering in semiconductors by changing the chemical composition of the materials is limited by the constraints on the lattice mismatch between the different semiconductor, which results in the

nucleation of defects and dislocations. However, different III-V semiconductor materials can be combined within the same nanowire due to the strain relaxation in the radial direction, with the possibility to form axial and radial heterostructures. Axial heterostructures are used in single nanowire quantum dot LEDs⁸ and in nanowire-based solar cell devices^{9,10}. In Fig. 1.1a the InP array with an axial pn-junction shows a record efficiency of 13.8%, achieved by covering only 10.2% of the substrate surface⁹. Core/shell heterostructures are commonly used in the GaN-based nanowire LEDs^{11,12}, where $\text{In}_x\text{Ga}_{1-x}\text{N}/\text{GaN}$ multi quantum wells (MQWs) provide high intensity optical emission in the blue range of the spectrum (Fig. 1.2)¹³.

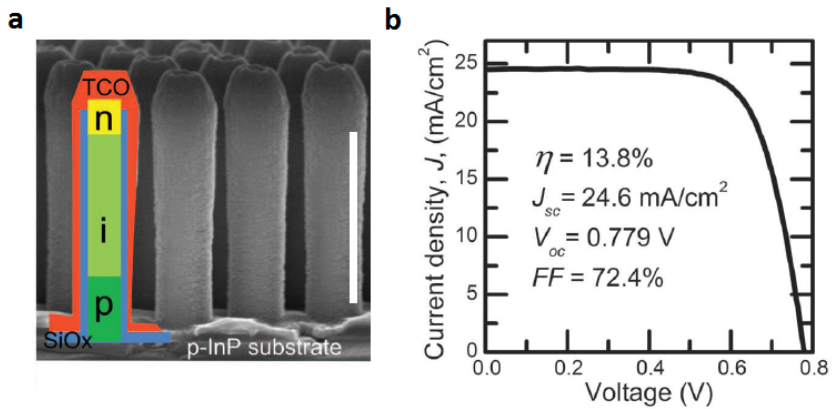


Figure 1.1: (a) Side view SEM image of InP NW-array solar cell device. Scalebar: 1 μm . (b) The 1-sun current-voltage curve for the highest efficiency cell. Adapted from Ref.⁹.

Furthermore, the strain relaxation in nanowires allows the group IV semiconductors to be integrated in the III-V materials. The scanning electron microscopy (SEM) image in Fig. 1.3a shows the axial stacking of Si, GaP, and GaAs segments within the same nanowire¹⁴. The radial growth of a Si shell around a twinning superlattice GaP wire in Fig. 1.3b transfers the crystal structure of the core into the shell, without the nucleation of defects¹⁵.

The 1D nature of the wire enhances waveguiding of the emitted light from the nanowire, with the formation of Fabry-Pérot modes along the wire axis^{16,17}. In those structures the lasing regime can be achieved, with high intensity optical emission at the end facets of a ZnO nanowire shown in Fig. 1.4a-b¹⁸. Furthermore, by combining ZnO nanowires with a n-type ZnO film an electrically-pumped optical emission is observed, with peaks related to the Fabry-Pérot modes in the wires (Fig. 1.4d-e)¹⁹. A wide range of nanowire-based devices has been developed in the last decade, such as sensors²⁰, lithium ion batteries²¹, thermoelectric devices²² and quantum devices²³. Furthermore, the detection of Majorana fermions was recently demonstrated in InSb nanowire devices²⁴.

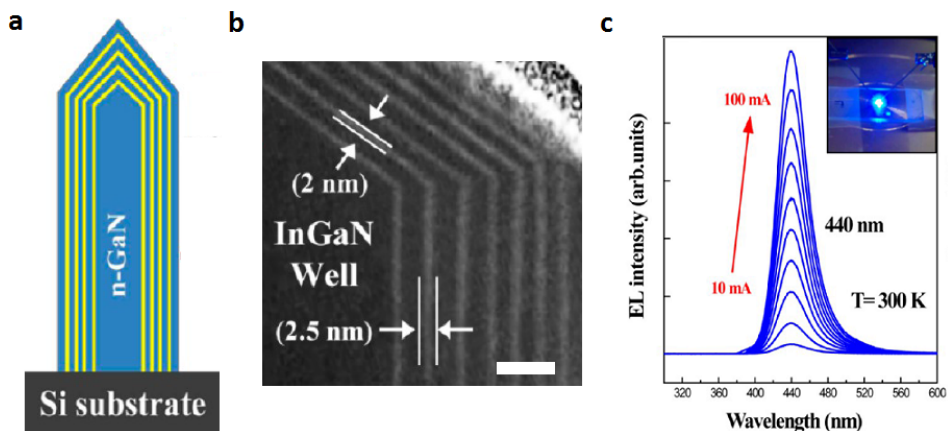


Figure 1.2: (a) Schematic of a coaxial $\text{In}_x\text{Ga}_{1-x}\text{N}/\text{GaN}$ MQW/ n-GaN NW grown on Silicon. (b) HRTEM image of the MQW region of the nanowire. Scalebar: 30 nm. (c) Electroluminescence (EL) intensity of the NW-LED device as a function of injection currents. Inset: optical image of the EL emission from the NW-LED. Adapted from Ref. ¹³.

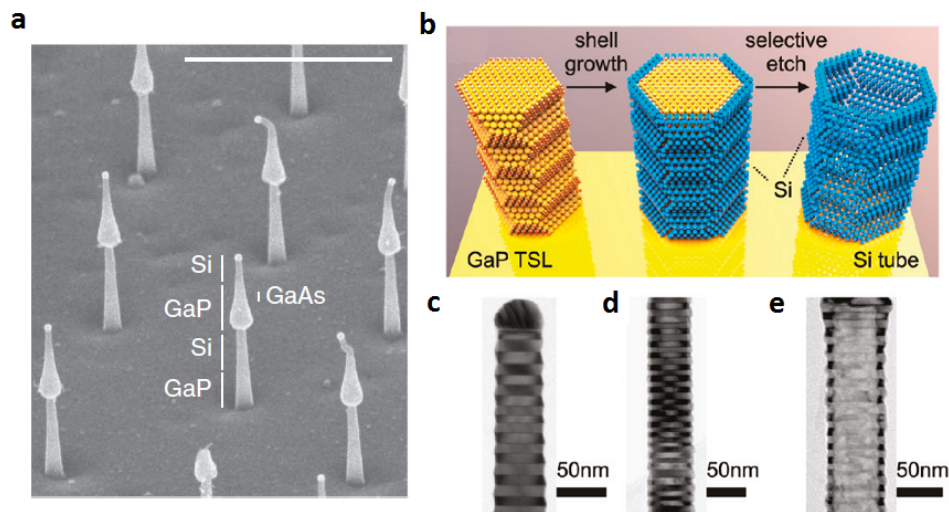


Figure 1.3: Integration of Si with III-V semiconductors. (a) SEM picture of an array of GaP-Si-GaP-GaAs-GaP-Si (hybrid Si/GaAs) nanowires. Tilting angle 45° . Scale bar: $1 \mu\text{m}$. Adapted from Ref. ¹⁴. (b) Schematic representation of the fabrication process for a twinning superlattice (TSL) Si nanotube. (c-e) TEM images of the steps in (b): TSL GaP nanowire (c), a similar nanowire after growth of a Si shell (d), and remaining Si shell after a selective wet chemical etch (e). Adapted from Ref. ¹⁵.

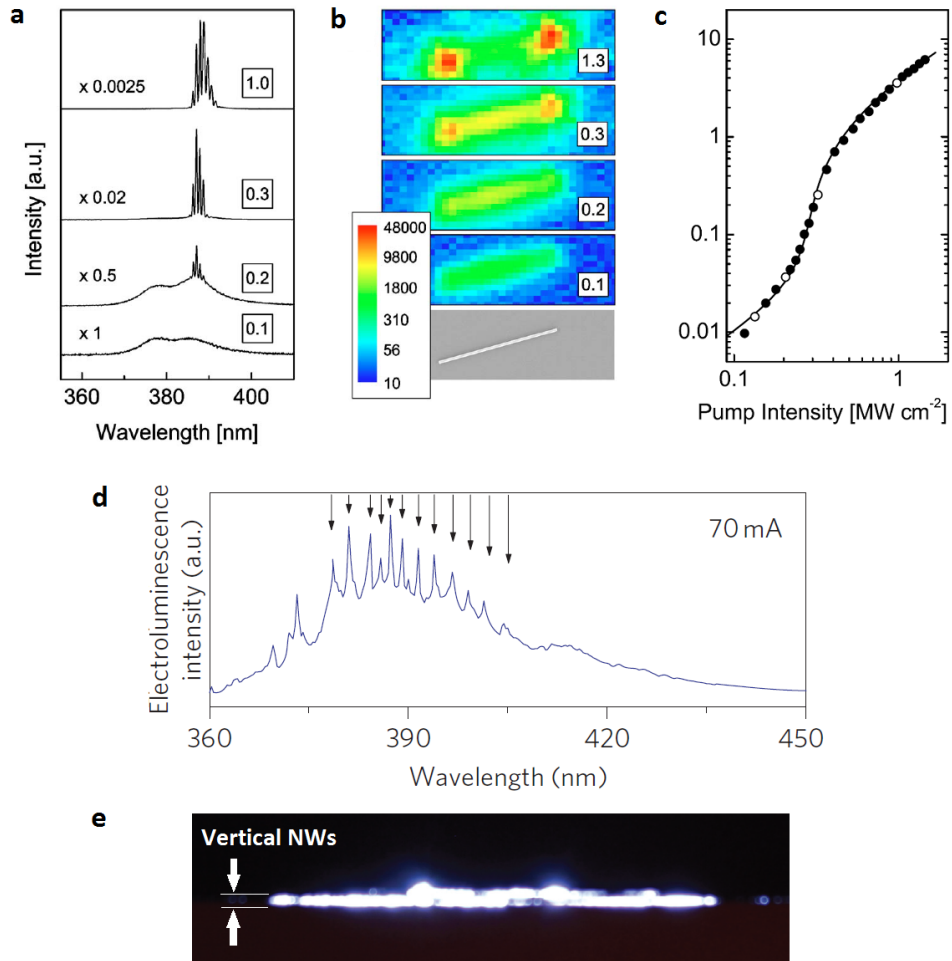


Figure 1.4: (a) PL spectra vs pump intensity of ZnO nanowire showing lasing. (b) SEM and CCD images under different pump intensities. The labels indicate the pump intensity in units of MW-cm⁻², while the color scale indicates the number of counts. (c) Pump intensity dependence of the total output power (circles) for the same nanowire. The open circles correspond to the spectra in (a). Adapted from Ref.¹⁸. (d) Electroluminescence spectra of a ZnO nanowire/device. Arrows represent quasi-equidistant peaks. (e) Side-view optical microscope image of the operating device. Adapted from Ref.¹⁹.

1.1.1 VLS growth

The semiconducting nanowires investigated in this thesis are grown from a gold nanoparticle using the VLS growth method. When the substrate is heated in the reactor chamber gold droplets are formed. The additional supply of the group III (Ga) precursor results in the formation of liquid Au-Ga alloy with the substrate, as shown in Fig. 1.5. The continuous supply of the precursor material from the gas phase brings the gold particle into saturation, eventually reaching a high enough supersaturation to start the nucleation at the droplet-substrate interface. Layer by layer growth occurs under the gold droplet, which is lifted up with the nucleation of a new layer. Dynamic equilibrium between the precursors supplied from the gas phase, transport through the droplet, and crystal growth at the gold-nanowire interface is reached during the nanowire growth. The metal particle acts as a catalyst, reducing the activation energy and allowing lower growth temperatures compared to bulk²⁵.

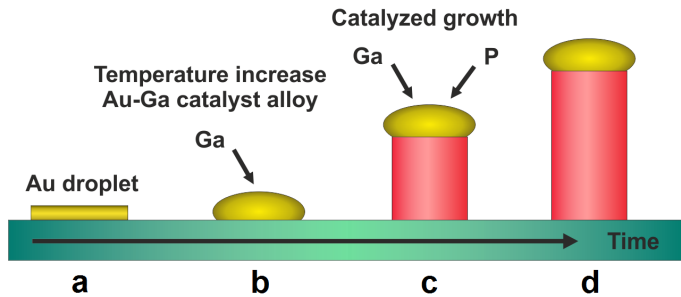


Figure 1.5: Different stages in the VLS growth mechanism. The metal particles on the substrate (a) are heated to form an alloy with the substrate and the precursor gases (b). When the supersaturation is reached, the layer by layer growth of the nanowire begins (c). The constant supply of the precursors from the gas phase ensure the VLS growth under the gold droplet (d).

Nanowires can be grown in periodic array patterns, with the diameter and position controlled using nanoimprint lithography and electron-beam lithography, as described in chapter 3. This allows studying the diffusion lengths, diffusion rate and supersaturation during the nanowire growth. The diffusion length of the precursor on the substrate surface determines the amount of material available for the growth per wire. This influences the supersaturation $\Delta\mu$, given by the difference in the thermodynamical potential per molecule between, for instance, the gas phase and the liquid phase. The diffusion rate determines how fast the material is transported through a specific phase. The small size of the gold catalyst results in a large surface to volume ratio and the Gibbs-Thompson effect can play a role, with an increase of the effective pressure in the gold particle due to the droplet curvature²⁶. This can affect the diffusion rate, thus the growth rate of the nanowire. The supersaturation is also determined by the pressure and the composition of the gold particle. Thus, a complex interdependence of diffusion, supersaturation and surface kinetics is observed in the nanowire growth.

1.1.2 Growth regimes

The density of the nanowires determines whether competitive growth, synergetic growth or independent growth is observed, as illustrated in Fig. 1.6a-c²⁵. The diffusion lengths over the substrate (λ_S) and through the gas phase (λ_g) are the main parameters that discriminate between the growth regimes. In case of both regime overlap ($\lambda_g \approx \lambda_S$) competitive growth occurs between the nanowires. If there is no overlap ($\lambda_g > \lambda_S$) the independent growth is observed. Synergetic growth takes place in between the two former growth regimes, where the interaction between the nanowires is possible only through the gas phase. The gold particle decomposes the group III precursor, which then contributes to the gas diffusion. Thus, nanowires with bigger diameters will decompose more material, resulting in higher diffusion through the gas phase and in an enhancement of the growth rate of the surrounding thin nanowires (Synergetic effect), as shown in Fig. 1.6d.

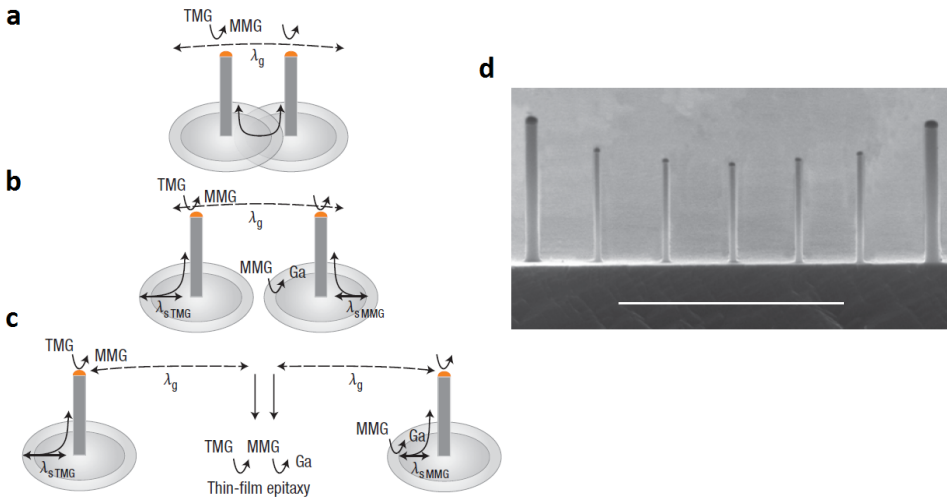


Figure 1.6: Diffusion regimes during nanowire growth. (a) Competitive growth, (b) synergetic growth and (c) independent growth regimes. The tri-methylgallium (TMG) decomposes in mono-methylgallium (MMG) at the gold droplet or at the substrate surface, contributing to the gas diffusion or to the surface diffusion, respectively. (d) Side-view SEM image of nanowires with different diameter. The thicker nanowires decompose more group III precursor, increasing the local supersaturation and enhancing the growth rate of the neighbouring thin wires (Synergetic effect). Scalebar: 1 μm . Adapted from Ref. ²⁵.

1.1.3 Sidewall growth

In the growth of III-V semiconductors the group III precursors usually have a longer diffusion length compared to the group V²⁷, contributing mainly through direct impingement on the catalyst particle in the nanowire growth (Fig. 1.7a). Thus, the group V molecules adsorbed on the substrate surface mainly contribute to the planar (2D) growth rather than to the axial nanowire growth. In this

situation the nanowire growth occur predominantly by direct impingement of the precursor at the gold droplet and untapered nanowires are observed. However, when the sample temperature is increased the catalytic effect of the gold particle becomes less predominant²⁵, resulting in a similar activation energy for both VLS and layer growth. The surface diffusion of the precursors from the substrate and the incorporation at the side walls induce lateral growth, and tapered nanowires are observed (Fig. 1.7b). By increasing the group V precursor flow the surface diffusion of group III adatoms decreases and the nucleation of a 2D layer on the nanowire side facets becomes favorable.

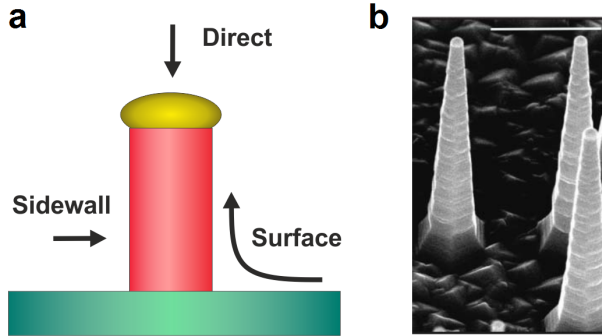


Figure 1.7: (a) Schematic representation of the processes during the nanowire growth. (b) SEM image of tapered InP wires (tilting angle 45°). Scalebar: $1 \mu\text{m}$. Adapted from Ref.²⁸.

1.2 Crystalline structure

Nanowires offer new possibilities in the control of the crystalline structure of the semiconductors. Bulk materials are grown with the zinc blende (ZB) crystal phase in the face centered cubic lattice. Instead, in nanowires also the wurtzite (WZ) crystal structure can be obtained. In a III-V material, one monolayer is composed of a pair of one group III and one group V atom. Fig. 1.8 shows the ABCABC stacking of the monolayers (each letter represent a monolayer) along the $\langle 111 \rangle$ crystallographic direction of the ZB phase and the ABAB stacking along the $\langle 0001 \rangle$ c-axis of the WZ phase.

The crystal structure determines the electrical, thermal, and optical properties of semiconductors²⁹. Theoretical calculations predict indirect to direct band gap transition in III-V materials such as gallium phosphide when the crystalline structure is changed from ZB into WZ^{30,31}. The band structure of WZ GaP will be discussed in more detail in chapter 2.

1.2.1 Defects

In the WZ phase the misplacement of a single monolayer (ML) results in the stacking sequence ABAB|CBCB, where AB|C is defined as a stacking fault, which is a single unit of the ZB structure. In the ZB phase, the misplacement of a single

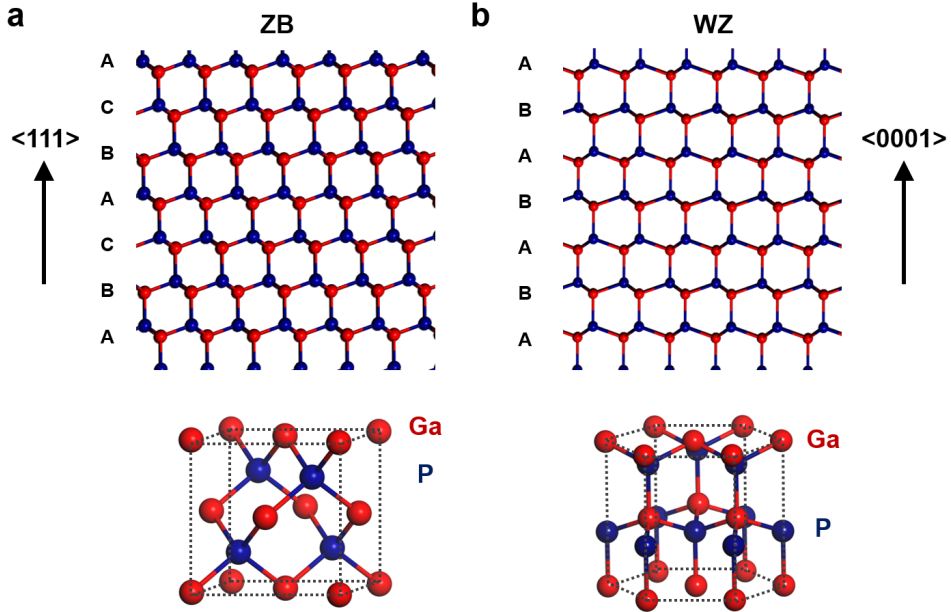


Figure 1.8: (a-b) Atoms stacking sequence and unit cell for the ZB (a) and WZ (b) crystal structures.

monolayer induces the stacking sequence ABCACBA where a twin plane **A** is observed, defined as the mirror plane between two segments rotated by 60° from each other. A single twin will not result in a stacking fault and no WZ segments are observed. The combination of two sequential twin planes or a stacking sequence of ABCA|C|A is required to observe WZ phase (4 MLs) in the ZB structure. In GaP, the thickness of a WZ monolayer is 0.317 nm ³², while in ZB phase this value reduces to 0.315 nm ³³. Thus, the smallest WZ segment in the ZB phase has a length of 1.268 nm (ABAB), while the smallest ZB segment in the WZ phase has a length of 0.945 nm (ABC).

1.2.2 WZ/ZB interfaces

In III-V semiconductors a band offset between the WZ and ZB structures is predicted²⁹⁻³¹, which results in the confinement of electron and holes in the former crystal segments, and the formation of crystal phase quantum well (CPQW) and quantum dot (CPQD) structures³⁴. Furthermore, nanowires with a periodic structure which consists of WZ/ZB segments results in a superlattice. For instance, this structure can be used to increase the scattering of the phonons and enhance the properties of thermoelectric devices³⁵. Recent developments in the nanowire growth have demonstrated the possibility to achieve atomically sharp WZ/ZB interfaces in nanowires³⁶, as shown for InAs wires in Fig. 1.9³⁷.

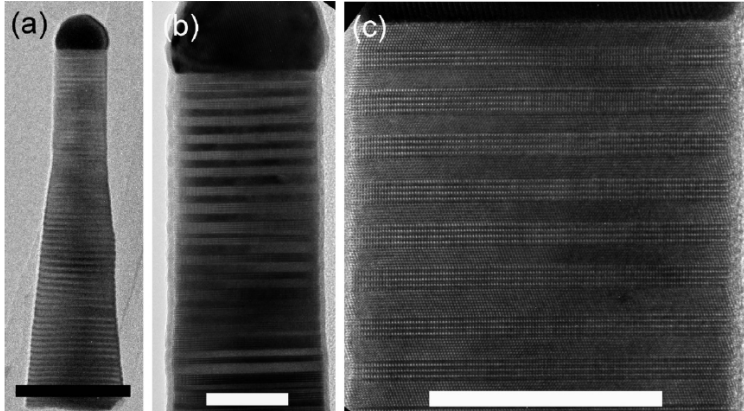


Figure 1.9: (a-c) TEM images of a InAs nanowire superlattice, defined by 60 periods of alternating ZB and WZ structure (each eight monolayers thick). Scalebars: (a) 80 nm, (b-c) 20 nm. Adapted from Ref.³⁷.

1.3 Scope of this thesis

In this thesis the growth of defect-free WZ Gallium Phosphide nanowires is developed to achieve a direct band gap emission in this material system. The direct band gap nature of WZ GaP is studied using photoluminescence techniques, which allow a correlation of optical properties with the predicted band structure. Furthermore, the growth of defect-free and atomically sharp WZ/ZB interface for quantum confined systems is achieved.

This thesis consists of 8 chapters, including this introductory chapter.

In chapter 2 the predicted band structure of WZ GaP calculated with the density-functional-theory (DFT) method is shown. The selection rules and the transition matrix elements for the transitions between the three valence bands and the two conduction bands are discussed.

In chapter 3 the methods and techniques used in the growth and characterization of the nanowires are presented. Nanoimprint lithography and electron beam lithography are used to pattern the arrays of catalyst prior to the growth in the metalorganic vapor phase epitaxy (MOVPE) reactor. The purity of the WZ crystal structure of the nanowires is studied using high resolution transmission electron microscopy (HRTEM) and x-ray diffraction (XRD) measurements. The optical properties of the nanowires are investigated using photoluminescence (PL) and photoluminescence excitation (PLE) spectroscopy in the range of temperatures from 4 K to 100 K.

In chapter 4 the growth of the WZ GaP wires is discussed. The combination of high growth temperature, low V/III ratio and the use of HCl gas promote the pure WZ crystal structure, without any tapering observed. The capping of the nanowires with a wider band gap AlGaP shell shows perfect epitaxy with no defects nucleated at the interface between the core and the shell.

The controlled switch during the nanowire growth between WZ and ZB crys-

tal phases is presented in chapter 5. Defect-free and atomically sharp interfaces between WZ/ZB segments are observed, with positions and sizes of the homojunctions controlled by the supply of the Ga precursor. The stability and reproducibility of this growth process allows the growth of WZ/ZB superlattice structures.

In chapter 6 the optical properties of WZ GaP wires are discussed using PL-PLE measurements. In the low excitation power regime, donor-acceptor pair (DAP) emission at 2.088 eV related to the direct band gap is observed, with a short lifetime of ~ 0.8 ns. At higher excitation powers, high energy bound excitons and free exciton states are visible in both PL-PLE spectra. Furthermore, the experimental data are correlated with the predicted band structure of WZ GaP.

In chapter 7 the waveguiding properties of the WZ GaP/ $\text{Al}_{0.4}\text{Ga}_{0.6}\text{P}$ core/shell nanowires are discussed. Fabry-Pérot cavity modes are observed in the wires, which allow an estimation of the refractive index and of the dielectric constant of WZ GaP.

In the final chapter 8 the applications related to the WZ GaP nanowires are shown. Ternary compound WZ $\text{Al}_x\text{Ga}_{1-x}\text{P}$ and $\text{GaAs}_y\text{P}_{1-y}$ nanowires allow tunability of the emission wavelength of the wires in the range 1.797-2.232 eV. This can be beneficial for the next generation of white LEDs. Due to the direct band gap nature of the nanowires, p-type WZ GaP wire arrays shows a huge increase in efficiency for photoelectrochemical production of hydrogen compared to bulk GaP layers. Lastly, the growth of a hexagonal Silicon shell grown around the WZ GaP core is shown. According to the predicted band structure this could lead to more efficient Si-based optical devices.

Chapter 2

Calculated band structure of wurtzite GaP

In this chapter, we illustrate the role of the crystal symmetry in the band structure of GaP. Theoretical calculations of the GaP band structure indicate a transition from the indirect band gap in the ZB phase into a direct band gap in the WZ phase. The transitions between the three valence bands and the two conduction bands are discussed based on the selection rules and on the transition matrix elements.

2.1 Crystal Hamiltonian

The general non-relativistic wave function is given by the solution of the time-independent Schrödinger equation:

$$\hat{H}|\Psi\rangle = E|\Psi\rangle, \quad (2.1)$$

where $|\Psi\rangle$ is the wave function describing the stationary states of the system, E is the set of energy eigenvalues belonging to those stationary states, and \hat{H} is the Hamiltonian operator describing the system. The Hamiltonian of a semiconductor crystal consists of several terms describing the various interactions in the crystal. In general it can be written as³⁸:

$$\begin{aligned} \hat{H} = & \sum_i \frac{p_i^2}{2m_i} + \sum_j \frac{P_j^2}{2M_j} + \frac{1}{2} \sum_{j',j} \frac{Z_j Z_{j'} e^2}{4\pi\epsilon_0 |\mathbf{R}_j - \mathbf{R}_{j'}|} \\ & - \sum_{j,i} \frac{Z_j e^2}{4\pi\epsilon_0 |\mathbf{r}_i - \mathbf{R}_j|} + \frac{1}{2} \sum_{i,i'} \frac{e^2}{4\pi\epsilon_0 |\mathbf{r}_i - \mathbf{r}_{i'}|}, \end{aligned} \quad (2.2)$$

where \mathbf{r}_i denotes the position of the i th electron, \mathbf{R}_j is the position of the j th nucleus, Z_j is the atomic number of the nucleus, \mathbf{p}_i and \mathbf{P}_j are the momentum

operators of the electrons and nuclei, respectively, and e is the electronic charge. \sum' means that the summation is only over pairs of indices which are not identical. A large number of simplifications are needed to solve the Hamiltonian in (2.2). The electrons have to be separated in valence electrons and core electrons in order to associate the core electrons with the nuclei to form ion cores. The Born-Oppenheimer approximation, where the ions are treated as stationary particles respect to the motion of the electrons, reduces the Hamiltonian in (2.2) to:

$$\hat{H} = H_{\text{ions}}(\mathbf{R}_j) + H_e(\mathbf{r}_i, \mathbf{R}_{j0}) + H_{e\text{-ion}}(\mathbf{r}_i, \delta\mathbf{R}_j), \quad (2.3)$$

where $H_{\text{ions}}(\mathbf{R}_j)$ is the Hamiltonian describing the ionic motion, $H_e(\mathbf{r}_i, \mathbf{R}_{j0})$ is the Hamiltonian for the electrons with the ions frozen in their equilibrium positions \mathbf{R}_{j0} , and $H_{e\text{-ion}}(\mathbf{r}_i, \delta\mathbf{R}_j)$ describes the change in the electronic energy as a result of the displacements $\delta\mathbf{R}_j$ of the ions from their equilibrium positions.

The mean-field approximation can be used to assume that every electron experiences the same average potential $V(\mathbf{r})$. Thus, the Schrödinger equations describing the motion of each electron will be identical and given by:

$$\left(\frac{p^2}{2m} + V(\mathbf{r})\right)\Psi_n(\mathbf{r}) = E_n\Psi_n(\mathbf{r}), \quad (2.4)$$

where $\Psi_n(\mathbf{r})$ and E_n are the wavefunction and energy of an electron in an eigenstate labeled by n , respectively. The problem is reduced to finding the effective potential and solving the equation to find the one-particle wave functions. Since the electrons are moving in a crystal, the effective potential will depend on the characteristics and symmetry of this crystal.

2.1.1 First Brillouin zone of the ZB and WZ crystals

In a periodic crystal the electron wavefunctions can be written as a linear combination of the Bloch waves:

$$\Psi_{\mathbf{nk}}(\mathbf{r}) = \sum_k A_k u_{\mathbf{nk}}(\mathbf{r}) \exp(i\mathbf{k} \cdot \mathbf{r}), \quad (2.5)$$

where A_k are the linear coefficients, $u_{\mathbf{nk}}(\mathbf{r})$ is a function with the periodicity of the crystal and the set of wave vectors \mathbf{k} correspond to the set of allowed Bloch wave vectors for the crystal. Due to the periodicity of the crystal, the full information about the band structure can be found by restricting the wave vectors to the first Brillouin zone. In Fig. 2.1 the first Brillouin zone for the ZB and WZ crystal structure are shown.

The center of the Brillouin zone is the Γ -point. In the ZB reciprocal lattice, the three most important high-symmetry points are the X-K-L points, which lie on the $\langle 100 \rangle$, $\langle 110 \rangle$, and $\langle 111 \rangle$ oriented surfaces of the Brillouin zone, respectively. The A-point in the WZ reciprocal lattice lies on the hexagonal $\langle 0001 \rangle$ surface, while the M-point lies on the $\langle 1-100 \rangle$ surface.

2.1.2 Band symmetry

Symmetry operations can be identified in the unit cell of a periodic crystal using the Group theory, obtaining a set of irreducible representations of the point group

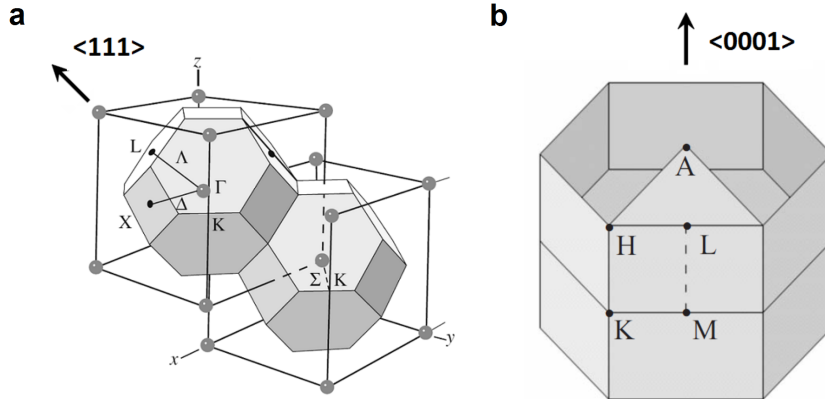


Figure 2.1: (a) First Brillouin zone of zinc blende crystal structure. Adapted from Ref.³⁸. (b) First Brillouin zone of the wurtzite crystal structures. Adapted from Ref.³⁰.

of the crystal³⁸. This set of representations defines how the wave functions of a crystal with wave vector \mathbf{k} at the center of the Brillouin zone (Γ point) transform. Since the electrons in the crystal move in presence of a periodic potential, their Bloch functions can be classified according to these irreducible representations, which are commonly labeled as Γ with a subscript i .

2.2 Methods to calculate the band structure

The band structure can be calculated using two independent methods known as empirical pseudopotential and density functional theory (DFT).

2.2.1 Empirical pseudopotential method

In a crystal the electrons can be divided into two groups: outer (valence) electrons in the higher energy states, forming the bonds with other atoms, and inner (core) electrons in the lower energy states closer to the nucleus³⁸. The wave function can be separated into a smooth pseudowave function for the valence states and a separate wave function for the core states. The pseudowave function is a good approximation of the real wave function away from the core region and can thus be used to calculate properties which depend only on the valence electron states. The true potential can be approximated by a smooth, effective pseudopotential for the valence electrons. The pseudopotential V_{pp} can be expanded in terms of reciprocal lattice vectors \mathbf{G} ³⁰:

$$V_{pp}(\mathbf{r}) = \sum_{\mathbf{G}, \alpha} V_{\alpha}^{FF}(\mathbf{G}) S_{\alpha}(\mathbf{G}) \exp(i\mathbf{k} \cdot \mathbf{r}), \quad (2.6)$$

where $V_{\alpha}^{FF}(\mathbf{G})$ is the pseudopotential form factors and $S_{\alpha}(\mathbf{G})$ is the structure factor. The pseudopotential form factors depend on the atomic species that form

the crystal, while the structure factors depend only on the reciprocal lattice vectors and the positions of the atoms within the primitive cell. Thus, the different structure factors determine the difference in the calculated band structures of the ZB and WZ crystal phases. In the empirical pseudopotential method, the form factors are obtained by fitting the calculated energy eigenvalues to the experimental data. Next, the ZB pseudopotential form factors can be transferred to the WZ crystal, assuming that the effects of local structure around an atom are dominant over the small difference in long-range order between the two polytypes. Instead, the structure factors can be calculated from the primitive cell parameters of the ideal WZ structure.

2.2.2 Density functional theory

In density functional theory (DFT) the dependence on the external potential $V(\mathbf{r})$ is replaced by the dependence on the electron density $n(\mathbf{r})$ ^{39,40}. In this approach, the electron density is the variable for the calculation of the total energy of the system using the Hohenberg-Kohn energy functionals⁴¹. Based on the variational principle, the energy functional for a given density provides the upper limit of the ground state energy of the system. When the electron density is expanded in terms of one-particle basis states, minimization of the energy functional becomes possible, resulting in the ground state electron density. Since the DFT is based on one-particle states, the local density approximation (LDA) is introduced to include the electron-electron interactions. Within the LDA, small spatial variations of the electron density occur and the contribution of electron-electron interactions (exchange and correlation energies) to the ground state energy can be calculated. The DFT procedure is the following: an initial value for the local electron density is chosen to calculate the effective potential and energy functionals. Next, the Schrödinger equation is solved, obtaining the single-particle wave functions. These wave functions are used to calculate the electron density via:

$$n(\mathbf{r}) = \sum_i |\Psi_i(\mathbf{r})|^2. \quad (2.7)$$

The next iteration starts with this new electron density and the process continues until the calculation converges to a self-consistent solution. In more advanced implementations, spin-orbit interactions can be taken into account. Furthermore, a better approximation than LDA is the LDA-1/2, where the quasi-particle structure is taken into account, with both valence and conduction bands which are half occupied by the quasi-particle⁴². This method is well suited for the estimation of the band gap measured through the optical excitation. The LDA-1/2 method can give rise to a minor underestimation of the lattice constants, which results in an overestimation of the energy gaps of around 2.9%⁴². However, this deviation is not expected to play a role in the band alignment between WZ and ZB crystal phases³¹.

2.3 Zinc blende band diagram

The band structure for the ZB Gallium Phosphide calculated using the empirical pseudopotential method is shown in Fig. 2.2⁴³. The ZB structure has an indirect band gap, with the minimum of the conduction band close to the X-point in the first Brillouin zone at an energy of 2.338 eV respect to the valence band maximum. The second indirect minimum at the L-point is at an energy of 2.72 eV, while the direct minimum at the Γ point is at 2.886 eV.

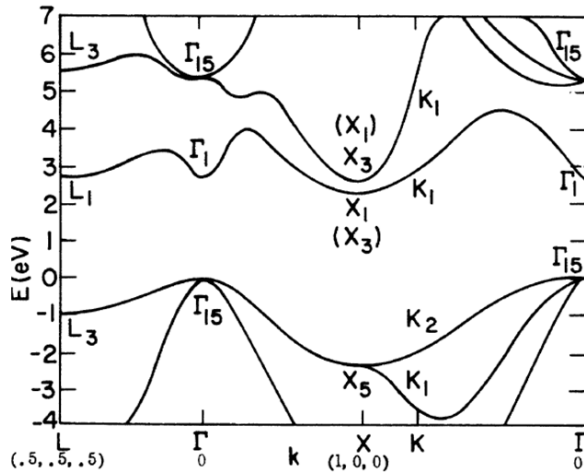


Figure 2.2: Band structure of ZB GaP calculated using the empirical pseudopotential method. Adapted from Ref. ⁴³.

2.4 Wurtzite band structure

The calculation of the band structure for the WZ GaP in Fig. 2.3a is performed solving the quasiparticle equation in the LDA-1/2 approximation which includes the spin-orbit interaction³¹. Because of the similarities between ZB and WZ when viewed along the $\langle 111 \rangle$ cubic crystal axis, a folding relationship between the two structures exists^{29,44}. In the WZ phase 4 atoms/cells are present, while the ZB phase has only 2 atoms/cell. As a consequence, two points on the Γ -L line in ZB fold onto the Γ -A line in WZ²⁹. Thus, the conduction band minima at the ZB Γ - and L-points give rise to two Γ -minima in WZ, Γ_{8c} at 2.123 eV (derived from L_{1c}) and Γ_{7c} at 2.888 eV (derived from Γ_{1c})³¹. Similarly, the conduction band minimum at the X-point in the ZB phase (X_{1c}) is folded onto the $2/3$ Γ -M direction of the WZ Brillouin zone at an energy of 2.351 eV. Consequently, the WZ GaP becomes a (quasi) direct semiconductor in which the lowest optical transitions are almost dipole forbidden. Because of the reduced symmetry, WZ does have an additional crystal field splitting not seen in ZB, which lifts the degeneracy of the valence band. Due to the strong crystal field splitting and spin-orbit interaction

three valence bands with Γ_{9v} , Γ_{7v+} and Γ_{7v-} symmetries can be identified (Fig. 2.3b).

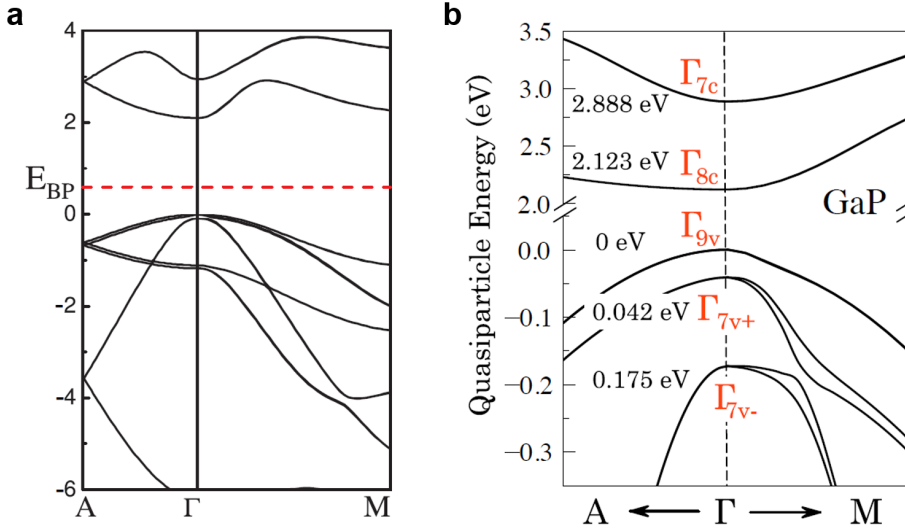


Figure 2.3: (a) Predicted band structure for WZ GaP calculated with the DTF-LDA-1/2 method. Adapted from Ref.³¹. (b) Uppermost valence and lowest conduction bands near the Γ -point⁴⁵.

2.4.1 Splitting of the valence band

From the band structure in Fig. 2.3 we can derive the most important splitting parameters of the valence bands. Within the quasicubic approximation (where the anisotropy of the spin-orbit interaction is neglected) only the crystal-field splitting Δ_{CF} (characterizing the hexagonal crystal field) and the spin-orbit splitting Δ_{SO} of the pure p-states are relevant. The $\mathbf{k}\cdot\mathbf{p}$ perturbation theory within the quasicubic approximation at the Γ point gives:

$$E_v(\Gamma_{9v}) - E_v(\Gamma_{7v\pm}) = \frac{1}{2}[(\Delta_{CF} + \Delta_{SO}) \mp \sqrt{(\Delta_{CF} - \frac{1}{3}\Delta_{SO})^2 + \frac{8}{9}\Delta_{SO}^2}]. \quad (2.8)$$

The values obtained from the calculation in Ref.³¹ are reported in Tab. 2.1.

2.4.2 Effective masses

The effective mass for electrons and holes for WZ GaP are listed in Tab. 2.2³¹. High values for the heavy-hole masses are found along the c-axis (A-direction), while much smaller values are obtained in the direction perpendicular to the c-axis (M-direction). Similar consideration hold for the light-hole masses, while

Structure	E _g (eV)	Δ _{CF} (eV)	Δ _{SO} (eV)	ΔE _v (meV)	ΔE _c (meV)
WZ (Γ)	2.123	0.135	0.083	135	-474
WZ (M)	2.266			135	-389
ZB (Γ)	2.790	0	0.082	0	0
ZB (X)	2.330			0	-460

Table 2.1: Characteristic parameters of the WZ and ZB band structures from approximate QP calculations including spin-orbit interaction for the WZ and ZB crystal structures. The band offsets ΔE_c and ΔE_v are measured with reference to E_c and E_v in the ZB phase. Adapted from Ref. ³¹.

opposite behavior is found for the split-off band. The Γ_{7c} conduction band masses (e2) are less anisotropic and rather small. The electron masses related to the Γ_{8c} conduction bands (e1) are much larger in the ΓA direction and, hence, are more anisotropic.

m_{hh}^A	m_{lh}^A	m_{so}^A	m_{e1}^A	m_{e2}^A	m_{hh}^M	m_{lh}^M	m_{so}^M	m_{e1}^M	m_{e2}^M
1.13	0.87	0.13	1.18	0.16	0.28	0.31	0.52	0.18	0.25

Table 2.2: Effective heavy-hole (hh), light-hole (lh), spin-orbit split-off masses and electron (e) masses in the lowest (1) or second lowest (2) conduction band at Γ for wurtzite III-V compounds. The masses are evaluated along the ΓA direction in the hexagonal BZ. All effective masses are given in units of the free-electron mass m . Adapted from Ref. ³¹.

2.4.3 Selection rules

The selection rules for the optical transitions derived from group theory are listed in Tab. 2.3⁴⁶. The transitions labeled as weak are allowed only due to the spin-orbit interaction. The optical transitions from the Γ_{9v} valence band into the Γ_{8c} conduction band are allowed only for polarization of the light perpendicular to the c-axis, while all the other transitions with the Γ_{8c} conduction band are forbidden. Different is the situation for the Γ_{7c} conduction band, where strong transitions are observed for excitation perpendicular (from Γ_{9v}, Γ_{7v+}) or parallel to the c-axis (from Γ_{7v-}).

2.4.4 Transition matrix elements

The absorption process is quantum mechanically described by the coupling of electron and photons using the time-dependent perturbation theory. If $\mathbf{H}' = \mathbf{H}_{em}$ is the perturbation operator (electromagnetic field) the transition probability per time W_{cv} for electrons from the valence band state 'v' to the conduction band 'c' is given by the Fermi golden rule⁴⁷:

$$W_{cv} = \frac{2\pi}{\hbar} |H'_{cv}|^2 \delta(E_c - E_v - \hbar\omega), \quad (2.9)$$

2. Calculated band structure of wurtzite GaP

Transition	X,Y	Z
$\Gamma_{9v} \rightarrow \Gamma_{8c}$	Weak	-
$\Gamma_{7v+} \rightarrow \Gamma_{8c}$	-	-
$\Gamma_{7v-} \rightarrow \Gamma_{8c}$	-	-
$\Gamma_{9v} \rightarrow \Gamma_{7c}$	Strong	-
$\Gamma_{7v+} \rightarrow \Gamma_{7c}$	Strong	Weak
$\Gamma_{7v-} \rightarrow \Gamma_{7c}$	Weak	Strong

Table 2.3: Selection rules for the optical transitions in WZ GaP. Derived from Ref. ⁴⁶.

where $\hbar\omega$ is the photon energy, E_v (E_c) is the energy of the initial (final) state. H'_{cv} is the matrix element:

$$H'_{cv} = \langle \Psi_c | \mathbf{H}_{em} | \Psi_v \rangle, \quad (2.10)$$

where Ψ_v and Ψ_c are the wavefunctions of the unperturbed initial and final states, respectively. In the electric dipole approximation the perturbation Hamiltonian can be written as:

$$\mathbf{H}_{em} = -\frac{q}{m} \mathbf{A} \cdot \mathbf{p} \approx q\mathbf{r} \cdot \mathbf{E}, \quad (2.11)$$

where \mathbf{A} is the vector potential, \mathbf{p} is the momentum of the electron, and \mathbf{E} is the electric field. Thus, the transition probability per time W_{cv} is found to be proportional the transition matrix element M_b :

$$| \langle \Psi_c | \mathbf{H}_{em} | \Psi_v \rangle |^2 = \frac{e^2 |A|^2}{m^2} M_b^2, \quad (2.12)$$

with

$$M_b^2 = \frac{1}{3} |\mathbf{p}_{cv}(\mathbf{k})|^2, \quad (2.13)$$

where \mathbf{p}_{cv} is the transition dipole momentum between the conduction band and valence band states. The wave-vector dependence of the transition matrix element is generally small and thus neglected. However, in the case of WZ GaP strong \mathbf{k} -dependence of the the momentum matrix element is predicted, as it will be discussed later. Furthermore, the transition matrix element is also dependent on the polarization of the incident light respect to the crystallographic axes (c-axis in WZ), hence the indexes \perp , \parallel are added to obtain $|\mathbf{p}_{cv}^{\perp/\parallel}(\mathbf{k})|^2$. The transition matrix element can be related to the oscillator strength of the band absorption edge f using⁴⁷:

$$f_{cv}^{\perp/\parallel} = \frac{e^2}{\epsilon_0 m \omega_{cv}^2} \frac{2 |\mathbf{p}_{cv}^{\perp/\parallel}(\mathbf{k})|^2}{m \hbar \omega_{cv}}, \quad (2.14)$$

where $\hbar\omega_{cv}$ is the energy of the former transition. The oscillator strength f is a dimensionless quantity that expresses the probability of absorption or emission of

the electromagnetic radiation in the transitions between the valence and conduction band levels. A strong overlap of the electronic wavefunctions results in a high oscillator strength for the optical transition. However, even if a significant spatial overlap of the wavefunctions exists, the resonant photon must induce a large transition dipole momentum \mathbf{p}_{cv} . If the symmetry of the valence and conduction bands involved in the electronic transition is similar, the resulting transition dipole moment is negligible and a weak oscillator strength holds⁴⁸.

2.4.4.1 Γ point

The momentum matrix elements for the WZ GaP calculated with the LDA-1/2 approach at the Γ point are shown in Tab. 2.4^{31,45}. The symmetry considerations discussed in Tab. 2.3 are reproduced by the DFT calculations. The oscillator strength for the $\Gamma_{9v} \rightarrow \Gamma_{8c}$ transition is very weak in perpendicular polarization (0.005), while the transitions between the other two valence bands Γ_{7v+} , Γ_{7v-} and the Γ_{8c} conduction band are predicted to be 0. On the contrary, the transitions with the Γ_{7c} conduction band are strong. Higher intensity for the perpendicular excitation is predicted for the $\Gamma_{9v} \rightarrow \Gamma_{7c}$ and $\Gamma_{7v+} \rightarrow \Gamma_{7c}$ transitions, while preferred parallel polarization is expected for the $\Gamma_{7v-} \rightarrow \Gamma_{7c}$ transition.

	Transition energy (eV)	Momentum matrix element $ \mathbf{p}_{cv}^{\perp/\parallel}(0) ^2$	
		\perp	\parallel
$\Gamma_{9v} \rightarrow \Gamma_{8c}$ (Γ_{7c})	2.123 (2.888)	0.005 (0.1158)	0 (0)
$\Gamma_{7v+} \rightarrow \Gamma_{8c}$ (Γ_{7c})	2.165 (2.929)	0 (0.1041)	0 (0.0378)
$\Gamma_{7v-} \rightarrow \Gamma_{8c}$ (Γ_{7c})	2.340 (3.104)	0 (0.0110)	0 (0.3409)

Table 2.4: Predicted values for the transition energies and momentum matrix elements of the optical transitions near the Γ point between the three highest valence bands and two lowest conduction bands. Adapted from Ref.^{31,45}.

2.4.4.2 Wave-vector dependence

The influence of a finite \mathbf{k} vector along the Γ -A and Γ -M directions for the optical transitions with the Γ_{8c} conduction band are shown in Figure 2.4⁴⁵. In perpendicular polarization, the oscillator strength of the $\Gamma_{9v} \rightarrow \Gamma_{8c}$ transition remains very weak until a point along the Γ -M line where mixing of the Γ_{8c} and Γ_{7c} states occur and enhancement in the oscillator strength is observed. Similar wave-vector dependence is predicted in the parallel polarization for the $\Gamma_{9v} \rightarrow \Gamma_{8c}$ transition and for both polarizations for the $\Gamma_{7v+} \rightarrow \Gamma_{8c}$ transition, but with a zero oscillator strength at the Γ point. For the $\Gamma_{7v-} \rightarrow \Gamma_{8c}$ transition the situation is similar to the previous transitions, but in this case a strong enhancement in the transition matrix element is predicted at large \mathbf{k} vectors along both the Γ -A and

2. Calculated band structure of wurtzite GaP

Γ -M directions.

The wave-vector dependence of the transition matrix element for the $\Gamma_{9v} \rightarrow \Gamma_{7c}$ transition is discussed in Ref. ³¹. High value in the oscillator strength is predicted in the perpendicular polarization, with a limited dependence on the \mathbf{k} vector. Instead in the parallel configuration non-zero transition matrix element is found outside the Γ point along the Γ -M line.

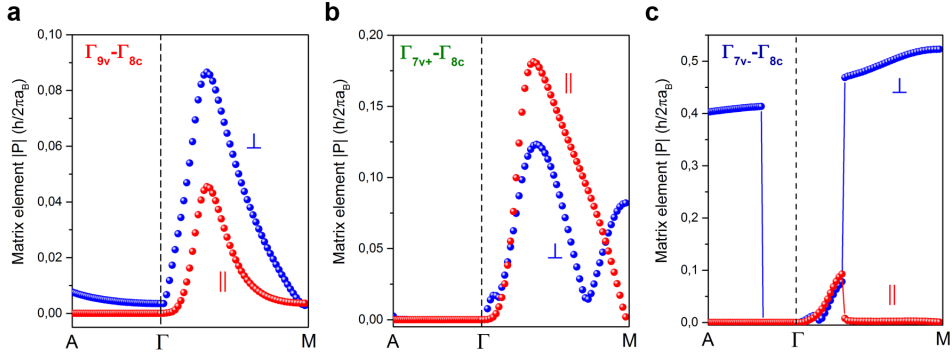


Figure 2.4: Wave-vector dispersion of the momentum transition matrix elements calculated for WZ GaP for the $\Gamma_{9v} \rightarrow \Gamma_{8c}$, $\Gamma_{7v+} \rightarrow \Gamma_{8c}$, and $\Gamma_{7v-} \rightarrow \Gamma_{8c}$ transitions. For each transition, the two curves correspond to polarization perpendicular (blue) and parallel (red) to the c -axis⁴⁵.

2.5 Excitons

An electron in the conduction band and a hole in the valence band can form a hydrogen-like state due to the mutual Coulomb interaction which is called an exciton state. The energy levels for the exciton in the Wannier-Mott approach are described by⁴⁷:

$$E_n = E_G - \frac{\mu e^4}{2\epsilon_r^2 \epsilon_0^2 \hbar^2 n^2}, \quad (2.15)$$

where μ is the reduced effective mass $\mu^{-1} = m_e^{-1} + m_h^{-1}$, ϵ_r is the dielectric constant, ϵ_0 is the permittivity of vacuum, and n is the level occupied by the electron. The exciton binding energy E_n^b for the n^{th} level is $E_n^b = -E_n$. The values for the exciton reduced masses calculated for optical transitions with the Γ_{8c} and the Γ_{7c} conduction bands using the effective masses in Tab. 2.2 are listed in Tab. 2.5.

	μ_{hh}^A	μ_{lh}^A	μ_{so}^A	μ_{hh}^M	μ_{lh}^M	μ_{so}^M
Γ_{8c}	0.58	0.50	0.12	0.11	0.11	0.13
Γ_{7c}	0.14	0.14	0.07	0.13	0.14	0.17

Table 2.5: Reduced effective masses for optical transitions with the Γ_{8c} and the Γ_{7c} conduction bands.

Due to the significant anisotropy of the kinetic energies of electrons and holes along the Γ -A and Γ -M directions, the exciton reduced effective masses is obtained by average of the reduced masses according to the following formula⁴⁵:

$$\frac{1}{\mu} = \frac{1}{3} \left[\frac{1}{\mu_{\Gamma A}} + \frac{2}{\mu_{\Gamma M}} \right]. \quad (2.16)$$

The values estimated from the previous formula are listed in Tab. 2.6, showing that the exciton will most likely form along the Γ -M direction. Furthermore, an enhancement in the transition matrix elements is also expected along the Γ -M directions, as previously discussed in Fig. 2.4.

	hh	lh	so
μ_{8c}	0.15	0.15	0.13
μ_{7c}	0.13	0.14	0.12

Table 2.6: Exciton reduced effective masses for optical transitions with the Γ_{8c} and the Γ_{7c} conduction bands.

The radius of the exciton a_n can be estimated from⁴⁷:

$$a_n = \frac{a_0 \epsilon_r}{\mu}, \quad (2.17)$$

where a_0 is the Bohr radius.

The values of the exciton binding energies and radius for $n=1,2,3$ excitons obtained using the masses in Tab. 2.6 for the Γ_{8c} conduction band are shown in Tab. 2.7. For the dielectric constant, the value of $\epsilon_r^{WZ}=15$ as described in chapter 7 is used in the calculations.

n	E_n^A (meV)	$\Delta E_{n-(n-1)}^A$ (meV)	E_n^B (meV)	$\Delta E_{n-(n-1)}^B$ (meV)	E_n^C (meV)	$\Delta E_{n-(n-1)}^C$ (meV)	Radius (nm)
1	9.1	-	9.3	-	7.7	-	5.3
2	2.3	6.8	2.3	7.0	1.9	5.8	5.2
3	1.0	1.3	1.0	1.3	0.9	1.1	6.2

Table 2.7: Exciton binding energies and radius for the WZ GaP $n=1,2,3$ excitons with the Γ_{8c} conduction band.

2.5.1 Phonon modes

The momentum selection rule for the free-exciton recombination allows only excitons with $\mathbf{k} \approx 0$ to recombine⁴⁷. Excitons with large \mathbf{k} can recombine if a phonon (or several phonons) are involved that provide the necessary momentum $\mathbf{q} = \mathbf{k}_1 - \mathbf{k}_2$, with \mathbf{k}_1 (\mathbf{k}_2) being the wavevector of the initial (intermediate) exciton state. The *zero-phonon* line at energy E_0 is then accompanied by phonon replicas below E_0 at integer multiples of the phonon energy $\hbar\omega_{ph}$:

$$E_n = E_0 - n\hbar\omega_{\text{ph}}. \quad (2.18)$$

The phonon dispersion of a three-dimensional crystal with N atoms per primitive unit cell is composed of $3N$ branches. Three of these branches are acoustic branches (neighbouring atoms in phase) and the remaining $3N-3$ are the optical branches (neighbouring atoms in opposite phase)⁴⁷. Since the displacement of the atoms can vary along the chain of atoms (longitudinal wave) or perpendicular to the chain of atoms (transverse wave), four different lattice vibrations exist: TA, LA, TO, and LO. The phonon dispersion curve for the WZ GaP crystal phase can be derived from the dispersion curve for the ZB GaP at the Γ - and L-points⁴⁹. The phonon dispersion of the WZ structure along the $\langle 0001 \rangle$ direction ($\Gamma \rightarrow A$) can be approximated by folding the phonon dispersion of the ZB structure along the $\langle 111 \rangle$ direction ($\Gamma \rightarrow L$), allowing the ZB phonons at the L-point to be also observed in the WZ structure^{50,51}. In the WZ structure, there is anisotropy in the macroscopic electric field induced by polar phonons⁵¹. Thus, depending on the crystalline direction, three types of phonon modes can be observed: axial A- and B-types ($\parallel c$ -axis), and planar E-type ($\perp c$ -axis). In the case of WZ GaP, group theory predicts eight phonon normal modes at the Γ point⁵¹: $2A_1+2E_1+2B_1+2E_2$, with one A_1 and one E_1 acoustic modes, while the remaining six modes are optical. The room temperature phonon energies for the TA/LA and TO/LO phonon modes for ZB GaP from Ref.⁵² are listed in Table. 2.8. The energy value of the low-temperature phonon modes is expected to be few meV higher than the room-temperature value⁵³.

Point	Phonon mode	Energy (meV)
$\Gamma(000)$	TO	45.3
$\Gamma(000)$	LO	49.9
L(111)	TA	10.7
L(111)	LA	26.7
L(111)	TO	44.0
L(111)	LO	46.5

Table 2.8: Room temperature phonon energies for the TA/LA and TO/LO phonon modes of ZB GaP. Adapted from Ref.⁵².

2.5.2 Bound excitons

Excitons can localize at impurities or potential fluctuations present in the semiconductor sample forming bound exciton (BE) states. In bulk ZB GaP the iso-electronic Nitrogen impurities form BE-complexes which results in the 'A-line' emission at 2.317 eV (at 4 K)⁵⁴. The transition energy of the bound-exciton can be written as:

$$E^{\text{BE}} = E^{\text{FE}} + E_b^{\text{BE}}, \quad (2.19)$$

where E^{FE} is the energy of the free exciton (E_n) and E_b^{BE} is the localization energy of the bound exciton. A transition involving an exciton bound to a neutral donor or to a neutral acceptor are denoted as (D^0, X) or (A^0, X) , respectively.

2.6 Donor-Acceptor pairs

Optical transitions between the electron and hole of a ionized donor-acceptor pair (DAP) can be observed in semiconductors. The free electron and the ionized donor return into the neutralized state upon the release of an energy E_D . At the same time, assuming that the donor and acceptor are separated by a distance R , the ionized acceptor and the free electron interact via Coulomb potential. Next, the hole and the ionized acceptor form a neutral acceptor, with a release of energy E_A . Thus, the energy of the photon emitted from the neutral DAP is described by⁵⁵:

$$\hbar\omega = E_g - (E_D + E_A) + \frac{1}{4\pi\epsilon_0} \frac{e^2}{\epsilon_r R}. \quad (2.20)$$

The last term describes the Coulomb interaction between the electron and the hole. For increasing carrier concentration, the DAP distance decreases, hence a blue-shift of the energy of the emitted photon is expected. In GaN bulk samples doped with Mg, DAP emission involving isolated Mg acceptors and spatially separated deep Mg related donors is observed, with a strong blue-shift of the peak energy with increasing excitation power of ~ 70 meV/decade⁵⁶. Similarly, heavily Zn-doped InP bulk samples show DAP transitions between interstitial Zn-donor levels and substitutional Zn-acceptor levels, with a blue-shift of the PL energy with increasing excitation power of ~ 40 meV/decade⁵⁷.

Chapter 3

Experimental methods and techniques

In this chapter, we discuss the experimental methods and techniques used for the growth and characterization of nanowire samples. The first step in the sample preparation is substrate patterning, followed by growth in a metalorganic phase epitaxy (MOVPE) reactor. The nanowire morphology is investigated using scanning microscopy (SEM), while the crystal purity of the material is assessed by transmission electron microscopy (TEM) and x-ray diffraction (XRD) techniques. The optical properties of the nanowires are studied by photoluminescence (PL) and photoluminescence excitation (PLE) spectroscopy measurements.

3.1 Substrate patterning

Nanoimprint lithography and electron beam lithography (EBL) techniques are used to define the size and position of the catalyst particles to control the diameter and the pitch of the nanowires. The nanoimprint process enables wafer scale patterning with nanometer resolution. However, restriction in the diameter and pitch of the nanowires due to the fixed mask used in the process apply. In the EBL the wide range of tunability in the gold droplet diameter (10 - 400 nm) and pitch (200 nm - 100 μm), together with a high degree of freedom into the design of the array pattern (square, hexagonal, circular, ...) make the EBL suitable for growth mechanism studies⁵⁸ and for any custom-made applications. However, the main limit of the EBL is in the long exposure time, which restrict this process only to small portions of the wafer.

3.1.1 Nanoimprint lithography

In the nanoimprint lithography the patterned arrays of holes are obtained by mechanical deformation of the imprint resist using a flexible stamp made of polydimethylsiloxane (PDMS). A silicon master pattern with arrays of holes obtained using EBL is used to create the flexible PDMS nanoimprint stamp with the protruding pillars.^{59–61} Before patterning, the 2" GaP wafer is cleaned using 10% H_3PO_4 acid. Next, a 300 nm low-molecular weight PMMA (Poly-methyl methacrylate, 35k) layer is spin-coated on the substrate followed by a baking at 150°C for 15 minutes. After that, a layer of silica based sol-gel imprint resist (TMOS-MTMS) is applied by spin coating over the PMMA layer⁶². The PDMS stamp is applied in the still liquid sol-gel resist within 1 minute after the spin coat process. The features in the stamp are filled by capillary forces with the sol-gel resist, as illustrated in Fig. 3.1.

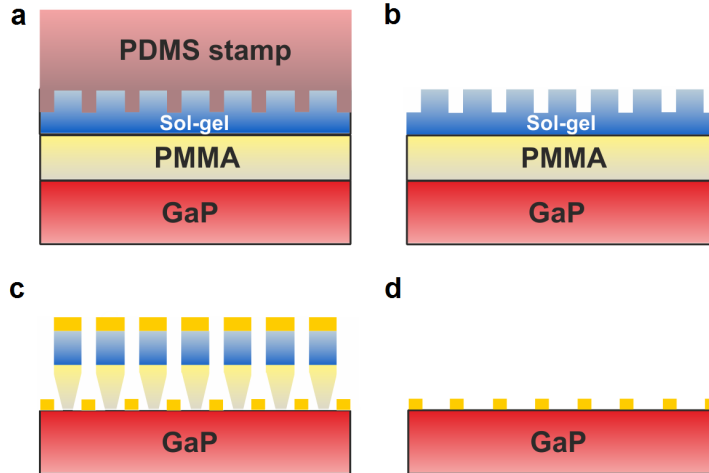


Figure 3.1: Schematic of the nanoimprint lithography process. (a) Application of the PDMS stamp in the liquid sol-gel resist. (b) Removal of the PDMS stamp which leaves the array of holes. (c) RIE etching and gold evaporation. (d) Lift-off.

The sol-gel forms a solid silica glass in 2-3 hours and then the PDMS stamp is slowly removed by peeling, leaving the full 2" wafer patterned with an array of holes. The sol-gel layer left between the bottom of the holes and the PMMA layer is etched using CHF_3 based reactive ion etch (RIE) for 40 s. An O_2 RIE step is used to transfer the pattern of the sol-gel layer into the underlying PMMA layer. The RIE etch stops when the GaP substrate is reached, however a short over etch is used to remove any residuals from the PMMA, leaving the bottom PMMA layer with larger diameter compared to the top sol-gel layer. The Gallium Oxide formed on the wafer surface is removed by 10% H_3PO_4 solution for 1 min and then the gold layer is evaporated. The thickness of the gold layer is used to control the gold droplet diameters. Generally, a 8 nm thick gold layer is chosen to obtain 90-100 nm diameter of the gold droplets. The final step is the lift-off

in acetone which dissolves the PMMA layer, leaving the gold droplets precisely placed in the positions of the array.

3.1.2 Electron beam lithography

In the EBL the pattern is defined by the interaction of the electron beam with the organic resist⁶³. The lithographic steps are shown in Fig. 3.2. The GaP wafer is cleaned using a King's water solution $\text{H}_2\text{O}:\text{HCl}:\text{HNO}_3$ (3:3:2) heated at 80°C. The wafer is dipped into the King's water for 90 s and then rinsed in water for 2 min. Next, a PMMA 950 K 2% layer is spin-coated at 5500 rpm and then baked for 30 min at 175°C. The following step is the e-beam exposure in the Vistec EBPG5000+ machine, which leaves the PMMA layer patterned with arrays of holes.

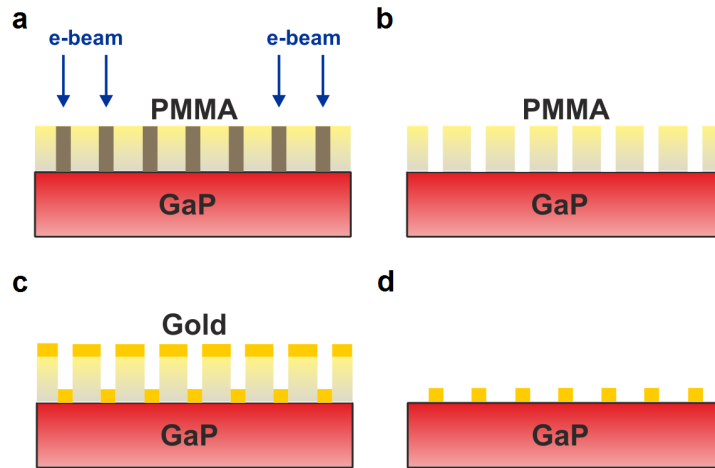


Figure 3.2: Schematic of the EBL process. (a) Electron beam exposure of the PMMA layer. (b) Development of the patterned substrate. (c) Evaporation. (d) Lift-off.

After the e-beam step, the resist is developed using first a Methyl isobutyl ketone (MIBK) and Isopropanol (IPA) (1:3) solution for 80 s and then IPA for 80 s. The 15 s O_2 plasma is used to enhance the opening of the holes in the PMMA. A 7 s HF (AF 87.5 - 12.5 VLSI) step followed by a rinse in water for 2 min is used to remove the oxide residual from the O_2 plasma treatment. Next, the gold layer is evaporated on the wafer and the lift-off process take place in the PRS 3000 solution heated at 70°C for 15 min, followed by 15 min Acetone and 5 min IPA rinse steps.

3.1.3 Pre-growth substrate cleaning

Prior to loading the samples into the nanowire growth machine, the patterned GaP substrate is cleaned with a wet chemical etch which removes any residuals from the lithographic steps. The Pirana solution contains a mixture of sulfuric acid (H_2SO_4 95-98%), 30% hydrogen peroxide (H_2O_2) and water (4:1:1). The

samples are first dipped in the H_2SO_4 for 10 s, then into the Pirana solution for 45 s, followed by H_2SO_4 for 10 s, and finally rinsed in water for 5 min.

3.2 Metalorganic vapor phase epitaxy

Metalorganic vapor phase epitaxy (MOVPE) is an epitaxial crystal growth technique used for growing high quality single crystalline thin films of different materials on a variety of substrates. This method is widely used in the III-V semiconductor optoelectronic industry, such as for Gallium Nitride (GaN) LEDs. In an MOVPE system two types of precursors are used: the hydrides and the metalorganics. For the latter precursors a hydride carrier gas (typically hydrogen) transfers the precursor gases from the bubblers into the reactor. The schematic of a MOVPE machine is shown in Fig. 3.3.

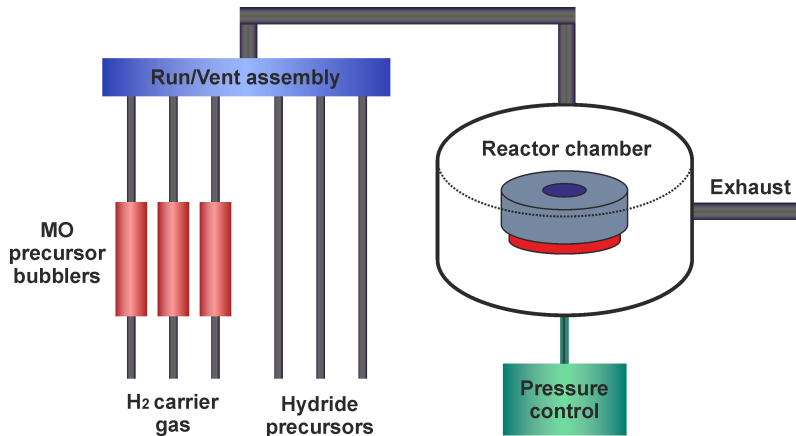


Figure 3.3: Schematic of the MOVPE reactor components.

The temperature of the bubbler and the rate of the carrier gas flow determine the amount of metalorganic precursor transported to the reactor. Epitaxial growth occurs in the reactor chamber, where the wafer is positioned on a rotating susceptor (graphite) maintained at a controlled temperature. Due to the elevated substrate temperature, the metalorganic and hydride precursor pyrolyse, leaving the group III and V as adatoms on the substrate surface. Diffusion of the adatoms over the substrate is influenced by the roughness of the wafer surface. In the final step the atoms bond to the substrate surface to form a new epitaxially grown layer. During growth, two important parameters are the substrate temperature and the V/III ratio of the precursors flow. The complete pyrolysis of both the Tri-methyl Gallium (TMG) and Phosphine (PH_3) precursors requires the temperature to be higher than 570°C (Fig. 3.4)⁶⁴. For temperatures lower than the latter value only a partial decomposition of the precursors occur. In addition, for obtaining high crystal quality, it is beneficial to have high surface mobility of the adatoms. For a high V/III ratio the group III atoms have a low surface mobility, while when the V/III ratio is too low the surface will decompose and the group V atoms evap-

orate, leaving the substrate with group V vacancies. Another critical parameter is the total pressure in the reactor which determines the partial pressures of the source materials, and hence the deposition rate.

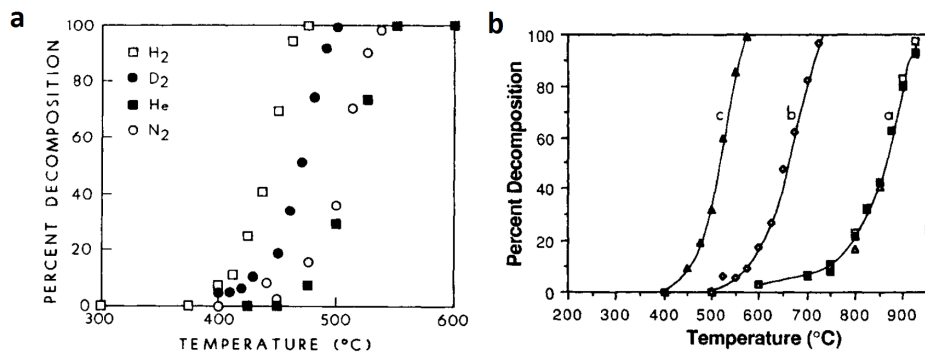


Figure 3.4: (a) Decomposition curves of the TMG precursor versus temperature. The multiple curves relate to the process conditions that apply for different reactor dimensions and background pressures, such as H₂, He, N₂, or D₂. Adapted from Ref.⁶⁴. (b) Decomposition curves of the PH₃ precursor versus temperature. The curve labeled as c is measured in a silica tube with a thin InP coating. Adapted from Ref.⁶⁴.

In this thesis, a vertical (shower head) reactor AIXTRON-CCS is used for the nanowire growth, as shown in Fig. 3.5. In this geometry, the gases are injected in the reactor via the water-cooled shower head surface. Due to injection via many small holes, a homogeneous distribution of the precursors over the whole surface of the wafer, in the direction perpendicular to the substrate, is obtained. The very short distance between the shower head and the substrate (16 mm) ensures fast gas switching. The design of the gas inlet keeps the group V and group III precursors separated until the precursors are injected into the reactor through separate openings, allowing an even distribution of the gases, which results in good uniformity of the growth. The semiconductor wafer is placed on a rotating susceptor heated by a resistive heater, with separated heating zones to ensure a uniform temperature profile across the entire substrate. By using optical sensors mounted on top of the shower head, the *in-situ* substrate temperature profile can be monitored during growth.

The GaP nanowires described in this thesis have been grown using TMG and PH₃ as precursors. During the nanowire growth, Hydrogen Chloride (HCl) gas was introduced into the reactor chamber to prevent the tapering of the nanowires²⁸. Ternary nanowires such as Al_xGa_{1-x}P and GaAs_yP_{1-y} were also grown by adding Tri-Methyl Aluminum (TMAI) or Arsine (AsH₃) precursors during growth.

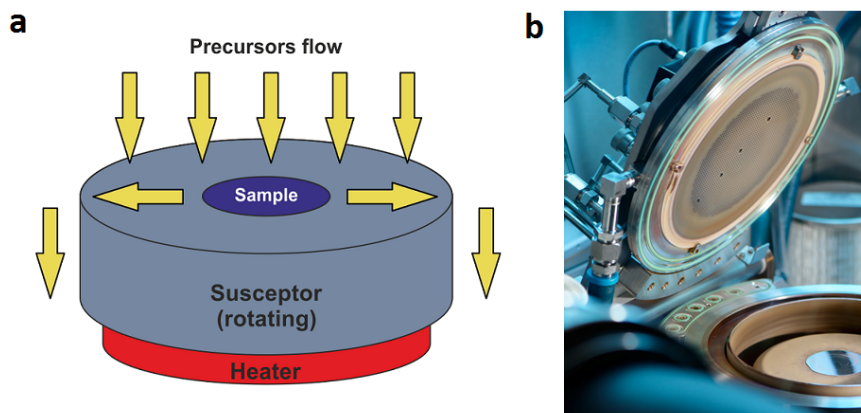


Figure 3.5: (a) Schematic representation of the vertical (shower head) MOVPE reactor geometry. (b) Optical image of the MOVPE reactor.

3.3 Scanning electron microscopy

In Scanning electron microscopy (SEM) the image of the sample is obtained by probing the specimen with a focused electron beam which is scanned across a rectangular area of the sample (raster scanning). A Zeiss Sigma SEM is used to obtain information on the morphology of the nanowires investigated in this thesis. The microscope is operated with an accelerating voltage of 10 kV and the generated secondary electrons are detected by an in-lens detector. The schematic drawing of the SEM column is shown in Figure 3.6⁶⁵. The electron beam is emitted from the electron gun (Schottky emitter) via thermal field emission and accelerated through the column. The beam is then focused using the electromagnetic lenses into a very narrow beam which passes into the scan coil to deflect the beam in the x-y axes, resulting in a raster scan over the rectangular area of the sample. When the beam interacts with the specimen the emission of back-scattered electrons (BSE), secondary electrons (SE), Auger electrons (AE), X-rays, and electromagnetic radiation occurs. The secondary electrons are collected in the annular SE detector placed inside the gun column (in-lens detector) and provide information on the surface topography. Depending on the type of microscope used, a SEM image can provide details of the surface with spatial resolution down to a few nanometers. For instance, by selecting different detectors for the generated electrons it is possible to obtain various types of information on the sample, such as density contrast, surface morphology, and chemical composition.

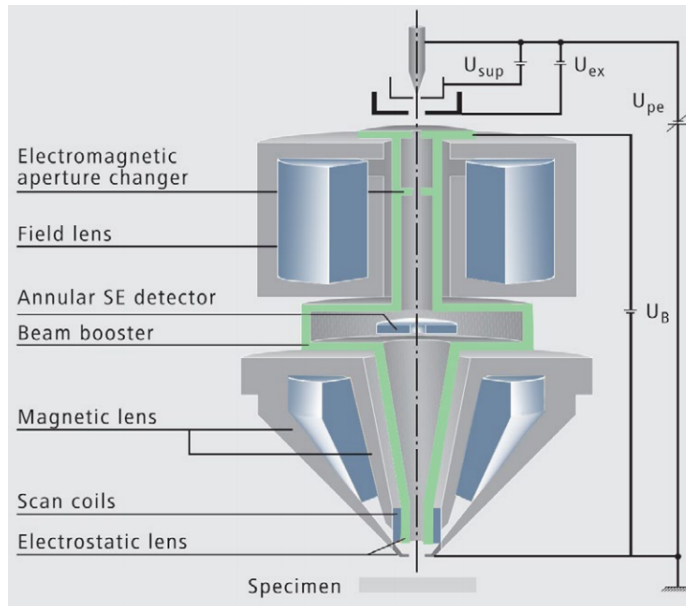


Figure 3.6: Schematic drawing of the Zeiss Sigma column⁶⁵.

3.4 Transmission electron microscopy

The SEM is a powerful tool to investigate the surface morphology of the nanowires. However, due to the limited resolution, no detailed information on the crystallinity of the nanowires can be obtained. Thus, the crystal structure of the nanowires is investigated using Transmission electron microscopy (TEM). Similarly to SEM, an electron beam is used but with higher acceleration voltage (up to 300 kV). Due to the high acceleration voltage the wavelength λ of the electrons is in the order of picometers and the imaging of the sample with atomic resolution becomes possible. To acquire the TEM images in this thesis, the FEI Tecnai F30ST and the JEOL ARM 200F Transmission electron microscopes were used (operated at 300 kV and 200kV, respectively) in three different modes: bright/dark field, high-resolution TEM (HRTEM) and Scanning TEM/High Angle Annular Dark Field (STEM/HAADF) modes. The schematic of a conventional TEM microscope is shown in Fig. 3.7⁶⁶. The electron beam is focused using magnetic lenses and then travels through the sample, where the scattering of the electrons occurs. In bright field TEM mode the transmitted beam is selected using an objective aperture placed in the back focal plane, obtaining the bright-field images. Instead, when one or more of the diffracted beams are selected a dark field image is formed. The transmitted beam is expanded in the bottom section of the microscope and then recorded using an imaging device, resulting in the formation of the sample image.

In the study of the crystal structure of the nanowires the two other TEM modes play a major role:

- High-resolution TEM (HRTEM): with a lattice resolution of 0.1 nm, in the

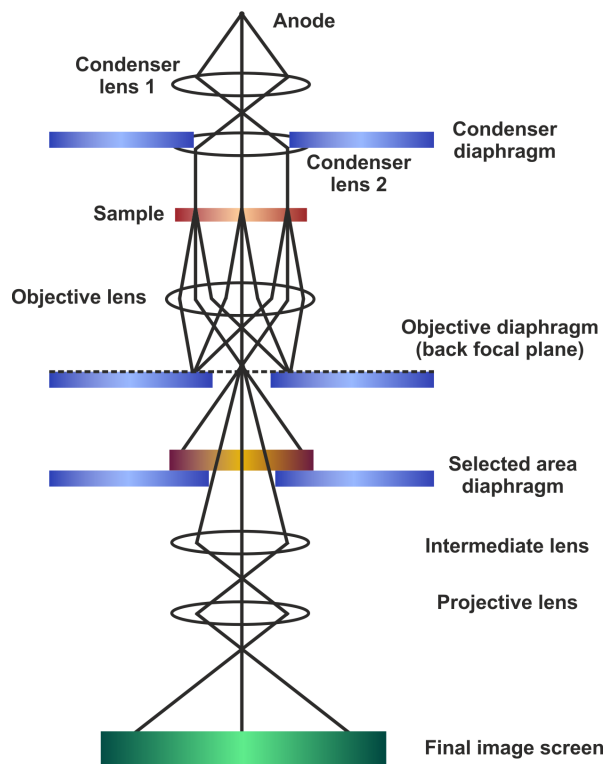


Figure 3.7: Ray diagram for a TEM in imaging mode⁶⁶.

HRTEM mode the transmitted and the scattered beams are used to form an image containing lattice fringes. The lattice fringes are not direct images of the atomic positions but can give information on the lattice spacings and the atomic structure of the crystal. The stacking of the WZ and ZB layers can be distinguished in the HRTEM images.

- Scanning TEM/High Angle Annular Dark Field (STEM/HAADF): the electron beam is focused into a narrow spot and scanned over the specimen in a raster with a scanning coil. The bright detector placed in the microscope axis collects the transmitted beam independently on the beam position on the sample (BFSTEM). Instead, by using a ring-shaped annular dark field (ADF) detector all the diffracted electrons except the transmitted ones are collected (Fig. 3.8). The HAADF image is generated by all the high-angle (>50 mrad) scattered electrons collected in the ADF detector in the STEM mode. Since the contrast in the HAADF images is highly dependent on the local average atomic number, this technique can be used in the investigation of nanowire heterostructures. Furthermore, the atomic positions can be precisely determined in the HRSTEM mode using the 0.07 nm resolution of the JEOL ARM TEM.

When the microscope is operated in the STEM mode, the chemical composition of the nanowires can be quantitatively obtained by Energy dispersive X-ray (EDX) spectroscopy. The electron beam can excite one of the core electrons (K-L-M shells) of the specimen, leaving a hole which is subsequently filled by an electron from an outer shell. The energy difference between the inner and outer shell is released in form of an X-ray emission. The emitted X-rays from the specimen are collected by a EDX spectrometer to form an energy spectrum. The energy of the emitted X-rays is characteristic of the energy difference between the two shells and of the atomic structure of the chemical element. Thus, EDX spectroscopy is a powerful tool in the study of core/shell nanowire heterostructures. An example of the possibilities of EDX for elemental analysis on the nanoscale is presented in Fig. 3.9a, displaying images of a GaAs nanowire covered with alternating layers of $\text{Al}_{0.33}\text{Ga}_{0.77}\text{As}$ and GaAs⁶⁷. The lighter regions correspond to GaAs and the darker regions to $\text{Al}_x\text{Ga}_{1-x}\text{As}$, with the contrast correlating directly with the Al content (Z-contrast). Dark stripes (Al enrichment) form at the nanowire corners, which open up in a low-content Al region constituting the quantum dot. The EDX profiles acquired along the two principal directions of the quantum dot are shown in Fig. 3.9b-c. In the direction from the quantum dot base towards the apex, the Ga signal decreases and the Al signal increases, whereas across the base, the Ga and Al signals remain constant. This information is consistent with a shape in the form of a pyramid⁶⁷.

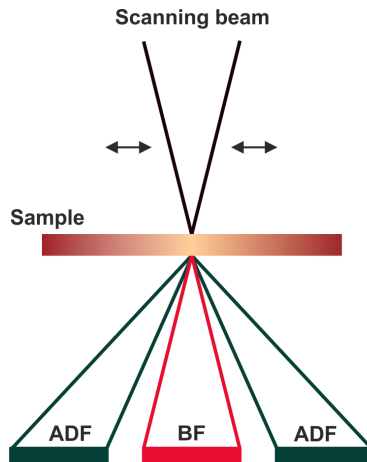


Figure 3.8: Schematic of the STEM showing the geometry of the annular dark field (ADF) detector and the bright field (BF) detector.

The TEM measurements on GaP nanowires shown in this thesis are performed by dr. M. Verheijen, while the TEM images on GaP/Si core/shell nanowires are acquired by dr. S. Conesa-Boj.

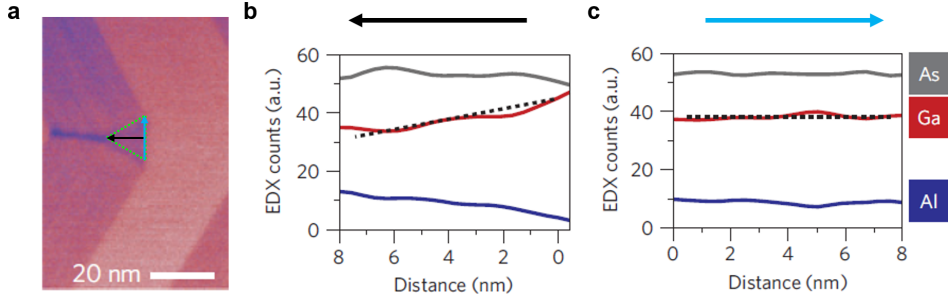


Figure 3.9: (a) Dark-field STEM image of a entire cross-section of a GaAs nanowire coated with multiple $\text{Al}_{0.33}\text{Ga}_{0.77}\text{As}$ shells. The Al-poor quantum dot (dashed green triangle) is located within the fork-like Al-rich stripes. (b-c) EDX profiles along two orthogonal directions of the quantum dot (black and cyan arrows). Adapted from Ref. ⁶⁷.

3.5 X-ray diffraction

When an X-ray beam interacts with a crystal lattice the scattering of the X-rays from the atoms produces a diffraction pattern which contains information about the atomic arrangement within the crystal. According to Bragg's law, the position of the diffraction peaks is determined by the distance between equivalent parallel planes of the atoms d_{hkl} as seen in Fig. 3.10a. Here, the Miller indices (hkl) are used to define the orientation of the set of lattice planes w.r.t. the crystal lattice. Constructive interference of beams diffracted by the set of planes of atoms occurs only when the Bragg's law is satisfied:

$$n\lambda = 2d_{hkl}\sin\theta, \quad (3.1)$$

where n is an integer, λ is the wavelength of the incident light, and θ is the angle between the beam and the scattering planes.

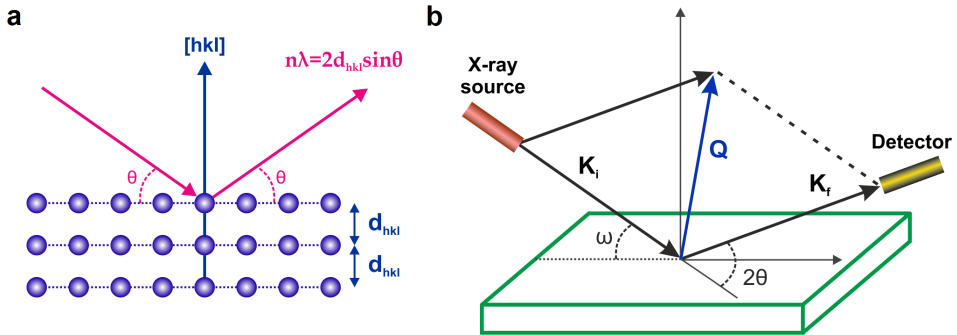


Figure 3.10: (a) Interaction of the X-ray beam with the parallel planes of atoms. (b) Sketch of the geometry for coplanar diffraction measurements.

The X-ray diffraction (XRD) measurements presented in this thesis are performed in the coplanar geometry as illustrated in Fig. 3.10b. The wave-vectors

$\mathbf{K}_{i,f}$ and the momentum transfer \mathbf{Q} in the reciprocal space are in the same plane with the normal to the sample surface. The incident angle ω is defined between the incident wave-vector \mathbf{K}_i and the sample surface, and the angle between the incident beam and the detector direction \mathbf{K}_f is the diffraction angle 2θ . The XRD patterns are acquired by probing the absolute intensity versus the scattering vector \mathbf{Q} . A crystalline sample produces a series of peaks in the diffraction pattern corresponding to the different interplanar spacings d_{hkl} . Furthermore, stacking faults in the nanowires lead to a broadening of the diffraction peaks. The XRD measurements shown in this thesis are performed by dr. D. Krieger.

3.6 Optical characterization techniques

3.6.1 Photoluminescence spectroscopy

Photoluminescence (PL) spectroscopy allows the study of the electronic transitions in a semiconductor material. Band gap transition, excitonic states, and impurity levels can be probed using this technique. The sample is illuminated using a laser with energy $\hbar\omega$ higher than the band gap to promote the formation of electrons in the conduction band and holes in the valence band (Fig. 6.2). Carrier relaxation toward the band edge due to phonon scattering is observed in the ps range⁶⁸. At this stage the formation of excitons can occur. Next, electron and holes recombine with the emission of a photon (radiative recombination). Shallow and deep levels associated with impurities and defects can result in the emission of photon with energy lower than the band gap. However, non-radiative recombination can also occur, where a phonon or an electron (Auger recombination) can be released instead of a photon. Due to the fast carrier relaxation the PL signal is mainly generated from the band edges rather than from higher energy bands.

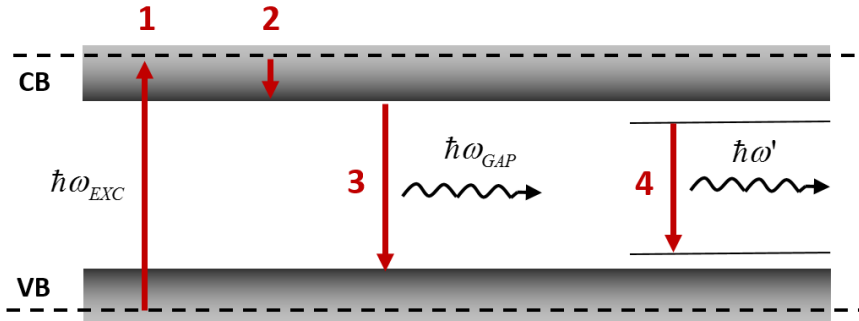


Figure 3.11: Schematic of the photoluminescence processes in the band structure of a semiconductor: 1) excitation, 2) carrier relaxation, 3) radiative recombination, 4) radiative recombination from impurity levels.

3.6.2 Photoluminescence excitation spectroscopy

With Photoluminescence excitation (PLE) spectroscopy we can probe the higher energy bands which are normally not observed in the PL measurements. In PLE spectroscopy the detection energy is fixed, while the change in intensity of the emitted light is measured as a function of the excitation energy. The emission intensity for a given optical transition can be written as³⁸:

$$I_{\text{em}} = P_{\text{abs}}P_{\text{rel}}P_{\text{em}}I_{\text{exc}}, \quad (3.2)$$

where I_{exc} is the intensity of the excitation, P_{abs} is the probability of absorption, P_{rel} the probability of relaxation to a particular emitting state, and P_{em} the probability of radiative recombination from that state. We assume that the electron-hole pair has relaxed to the emitting state and the P_{em} is constant and independent on the excitation energy. The relaxation process depends on the electron-hole pair energy, thus the excitation energy. Since non-radiative processes can be involved in the relaxation process, the emission intensity as a function of the excitation energy is not directly correlated to the absorption coefficient. Assuming that a single recombination channel is active, when the undoped material is grown with good crystal quality the probability of recombination through trap levels is low and P_{rel} is close to 1. This results in the intensity of the excitation I_{exc} of being proportional to the probability of absorption P_{abs} . Assuming that the conduction and valence bands are parabolic close to the band gap^{38,69}, the intensity of the PLE signal I_{PLE} becomes proportional to:

$$I_{\text{PLE}} \propto (E - E_0)^P I_{\text{exc}}, \quad (3.3)$$

where P is an exponent related to the type of the optical transition. For a direct band gap emission $P = 1/2$. In chapter 2, the threefold splitting of the WZ GaP valence band is discussed. Each of these bands will contribute to the PLE signal, with an absorption edge due to the generated free carrier, as shown schematically in Fig. 3.12. For increasing excitation energy the PLE spectrum will follow the intrinsic absorption in Eq. 3.3.

3.6.3 Optical setup overview

The main optical components used in the optical setup are shown in Fig. 3.13. The nanowire sample is mounted in a cryostat cooled down to 4 K using liquid Helium. The optical data are collected in backscattering geometry using a NA=0.7 Nikon 50X CR objective mounted on a XYZ-piezoelectric stage and a 50/50 beam splitter (BS). The spectrometer (focal length 0.30 m) is equipped with 1200 g/mm and holographic 2400 g/mm gratings (500 nm blazing angle), with a PIXIS CCD detector, and with a time correlated single photon counting (SPC) detector (130 ps instrumental resolution). In order to image the nanowires, the combination of a white lamp excitation together with a flip mirror in the detection path is used to send the image of the sample in the CCD camera. The optical emission from the nanowires can also be studied using the polarization optics in both the excitation and the detection paths.

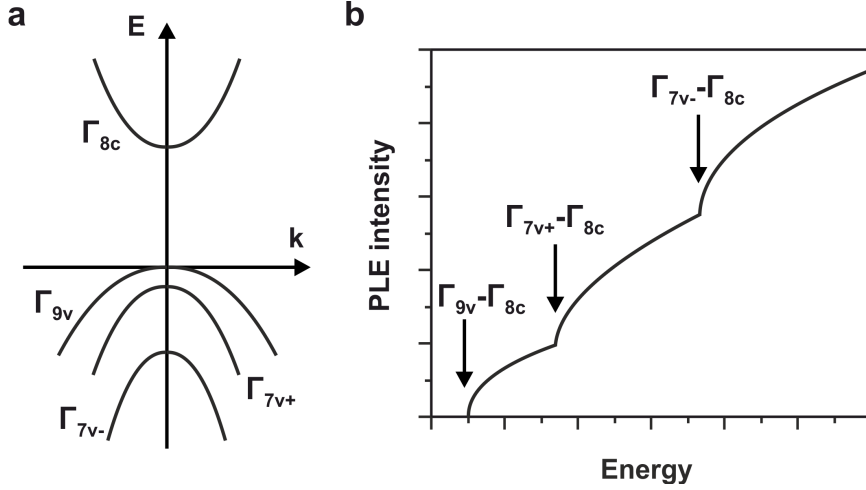


Figure 3.12: (a) Schematic representation of the wurtzite band structure. (b) Schematics of the PLE spectrum. The three onset of absorption are due to the transitions from the three valence bands with the lowest conduction band.

3.6.3.1 Excitation sources

Depending on the type of measurements to be performed, the experimental setup allows an easy switch of the optical excitation sources. Three different excitation sources are used in the PL measurements:

- Continuous-wave laser diode: excitation wavelength 405 nm. Circular excitation spot with diameter of $\sim 1 \mu\text{m}$ at the sample;
- Pulsed laser diode: excitation wavelength 420 nm, 1-80 MHz repetition rate. Circular excitation spot with diameter of $\sim 1 \mu\text{m}$ at the sample;
- Frequency-doubled Titanium-Sapphire laser: excitation wavelength set at 405 nm, 80 MHz repetition rate, beam coupled into $300 \mu\text{m}$ core multi-mode fiber. Circular excitation spot with diameter of $\sim 9 \mu\text{m}$ at the sample.

For the PL measurements on single wires a 1000 mm Cylindrical lens is used to defocus the $1 \mu\text{m}$ circular spot into a rectangular spot of around $1 \mu\text{m} \times 10 \mu\text{m}$ in size.

For the PLE measurements, a plasma-injected white lamp emitting in the range 200-800 nm is coupled into a 0.30 m monochromator equipped with 1200 g/mm grating (500 nm blazing angle). The output beam from the monochromator is coupled into a $300 \mu\text{m}$ core multi-mode fiber, resulting in excitation spot of $\sim 9 \mu\text{m}$ at the sample. The full width at half-maximum (FWHM) for the excitation wavelength is around 1 nm. The combination of shortpass 500 nm and 600 nm filters is used to remove artifacts generated from multiple light scattering in the monochromator. The variable neutral density filter controlled via the LabView

software ensures constant power across the wavelength scan.

The polarization of the excitation source is selected using a combination of a polarizer and a half-wave plate ($\lambda/2$).

3.6.3.2 Detection

The CCD and SPC detectors in the spectrometer collect the signal for the PL and lifetime measurements, respectively. The polarization of the emitted light from the nanowires is studied using a combination of a polarizer and a half-wave plate ($\lambda/2$). The PLE spectra are obtained by selecting the detection wavelength with the side slit and measuring the (PL) intensity at the SPC detector as a function of the excitation wavelength. A 600 nm band pass filter (10 nm FWHM) is used to further select the signal from the nanowires only, avoiding artifacts in the PLE spectrum. The angle between the detection beam and the filter is reduced from 90° to 60° to shift the center filter wavelength up to 595 nm.

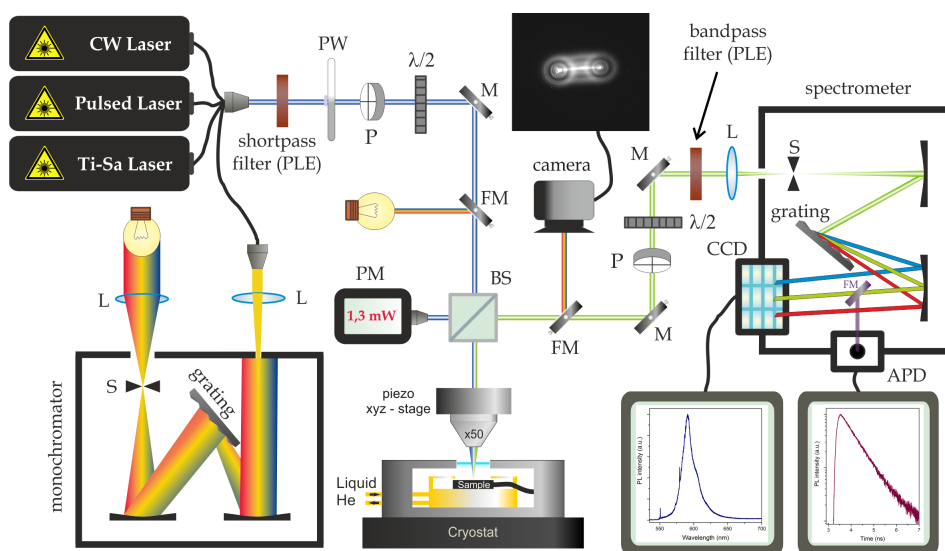


Figure 3.13: Schematics of the optical setup indicating the different configurations used during the measurements.

Chapter 4

Growth and structural characterization of WZ GaP nanowires

The indirect band gap of gallium phosphide with the zinc blende crystal structure³³ severely limits its use for light-emitting devices^{70,71}. Band structure calculations, however, predict a direct band gap for this material in the wurtzite crystal structure^{29,30,42,72}. A unique feature of the VLS nanowire growth mechanism is that well-known semiconductors can be grown with different crystal structures^{15,37,73–76}. The calculated direct band gap energy for wurtzite GaP ranges between 2.18–2.25 eV^{30,42}, and therefore WZ GaP is a promising candidate for light emission in the green-yellow region of the visible spectrum. Similarly, the band gap of Aluminum Phosphide (AlP) is predicted to change from indirect to direct when the structure is converted from cubic to hexagonal, with gap energy of 2.97 eV³⁰. Therefore, by forming ternary $\text{Al}_x\text{Ga}_{1-x}\text{P}$ and $\text{GaAs}_y\text{P}_{1-y}$ compounds, the emission wavelength can theoretically be tuned over a wide range. The transition from indirect to a direct band gap by changing from zinc blende to wurtzite has not yet been demonstrated experimentally for any material at ambient pressure conditions.

In this chapter, we show the Au-assisted VLS growth of pure WZ GaP/ $\text{Al}_{0.4}\text{Ga}_{0.6}\text{P}$ core/shell nanowire arrays over the GaP (111)B substrate using a MOVPE reactor. Nanoimprint lithography and electron-beam lithography are used to control the diameter and pitch of the nanowire arrays. The high growth temperature and the low V/III ratio promote the WZ structure of the nanowires, together with the use of *in-situ* HCl gas to avoid the lateral overgrowth. The high WZ crystalline quality of the sample is demonstrated using TEM microscopy and XRD measurements.

4.1 Nanowire growth

4.1.1 Growth parameters

The GaP nanowires are grown on (111)B oriented zinc blende GaP substrates using the VLS mechanism and patterned gold islands as catalysts in a low-pressure (50 mbar) Aixtron CCS-MOVPE reactor. In order to control the nanowire position two lithography techniques are used; electron beam lithography to fabricate small arrays with varying pitch and diameter (25-50-75-100 nm diameter, 200 nm-5 μ m pitch)²⁵, and nanoimprint lithography to pattern large-scale areas with a constant pitch and diameter (100 nm diameter/500 nm pitch). The high growth temperature of 750°C and the low V/III ratio are expected to promote the formation of the wurtzite crystalline structure^{15,37,73-76}. Prior to growth the GaP patterned substrates are annealed under Phosphine (PH₃) flow at 750°C to remove the oxide on the surface and the organic residuals of the lithographic steps. The nanoimprint and e-beam patterned samples are grown at 750°C for, respectively, 45 min and 20 min using Tri-Methyl Gallium (TMG) and Phosphine (PH₃) as precursor gases at molar fractions of $7.42 \cdot 10^{-5}$ and $1.71 \cdot 10^{-3}$, respectively, with a total flow of 8.2 liters/minute using hydrogen as carrier gas. A V/III ratio of 23 is used⁷⁷. The growth is performed under Hydrogen Chloride gas (HCl) flow (molar fraction $1.22 \cdot 10^{-4}$) to suppress the radial overgrowth of the wires²⁸.

A wider band gap ternary Al_{0.4}Ga_{0.6}P shell is grown around the GaP⁷⁸ core to suppress possible undesirable surface effects that could affect the optical properties of the nanowires. Shells are grown under different conditions compared to axial nanowire growth, and the thickness is controlled by the shell growth time and the composition by the Al/Ga gas input ratio. The growth of the Al_{0.4}Ga_{0.6}P shell is performed at 690°C for 4 min (nanoimprint sample) and 20-240 s (e-beam sample) using TMG, Tri-Methyl Aluminum (TMAI) and PH₃ as precursor gases at molar fractions of $2.7 \cdot 10^{-5}$, $1.5 \cdot 10^{-5}$ and $1.1 \cdot 10^{-2}$, respectively.

4.1.2 Uniformity of GaP nanowire arrays

The cross sectional scanning electron microscopy (SEM) image in Fig. 4.1a shows a uniform array of $6.6 \pm 0.2 \mu$ m long non-tapered nanowires with almost 100% yield defined by nanoimprint lithography. Radial growth, which leads to tapered nanowires, has been totally suppressed by using HCl during growth²⁵. The optical photograph image in Fig. 4.1b shows the large-scale uniformity of a typical sample. The periodicity of the nanoimprint pattern is clearly visible in Fig. 4.1c. The SEM image of e-beam defined nanowire arrays is shown in Fig. 4.1d. The diffusion of the precursors over the GaP substrate during the AlGaP shell growth results in small overgrowth at the bottom of the nanowires.

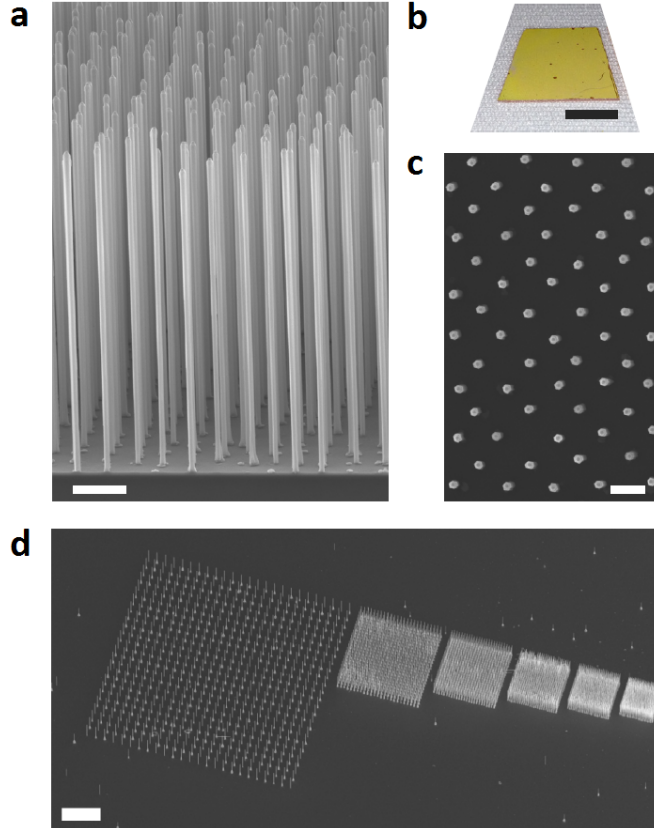


Figure 4.1: (a) Scanning Electron Microscopy (SEM) picture of GaP/Al_{0.4}Ga_{0.6}P core/shell nanowires in a nanoimprint pattern (tilting angle 70°). Scalebar: 1 μ m. We note that although the wires are grown at high temperatures ($T=750^{\circ}\text{C}$), untapered wires are obtained by the use of HCl during growth. (b) Optical image of the nanowires sample. Scalebar: 0.5 cm. (c) SEM top-view image of the same sample as in a showing the periodicity of the nanoimprint pattern. Scalebar: 500 nm. (d) SEM image of GaP/Al_{0.4}Ga_{0.6}P core/shell nanowire arrays grown from Au droplets positioned by electron beam lithography with constant diameter of 100 nm and varying pitch (tilting angle 30°). Scalebar: 20 μ m

4.2 Crystalline structure

4.2.1 Pure WZ crystal phase

In order to assess the crystal structure of the nanowires, high-resolution transmission electron microscopy (HRTEM) studies are performed. In Fig. 4.2 the HRTEM image and the corresponding Fast-Fourier Transform (FFT) demonstrate the wurtzite crystal structure of the GaP nanowires. Typically, less than 1 stacking fault (SF) per micrometer is observed for the tens of wires studied. An example of a whole wire, which has been imaged from top to bottom by TEM is shown in

Fig. 4.3. No significant change in the wire diameter is observed. Furthermore, only four defects are visible in the 12.5 μm long wire, confirming the high purity of the WZ crystal structure. One stacking fault consisting of a twinned ZB segment is shown in the HRTEM image in Fig. 4.4.

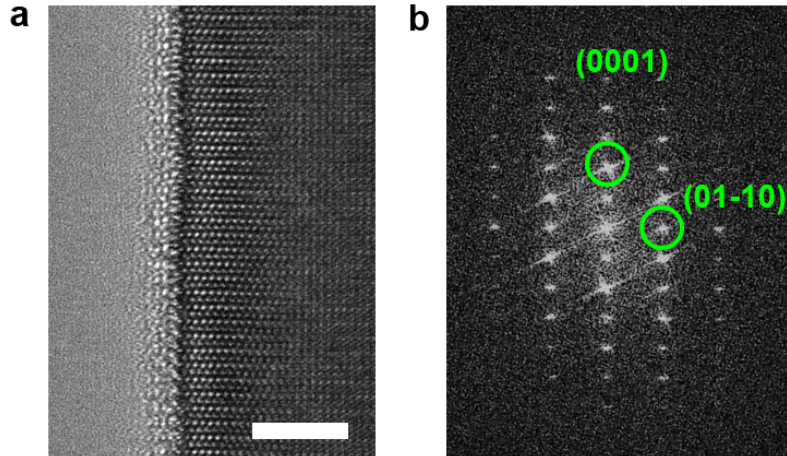


Figure 4.2: (a) HRTEM image viewed in the $\langle 11-20 \rangle$ zone axis showing the pure wurtzite crystal structure. Scalebar: 5 nm. (b) Fast-Fourier Transform image of the wire in (a).

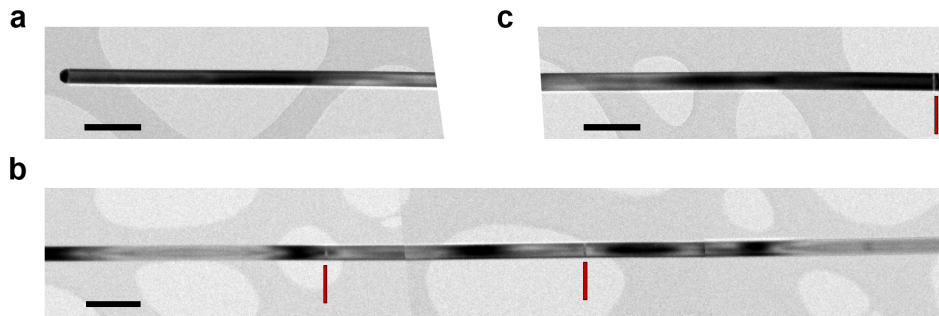


Figure 4.3: (a-c) Bright field TEM images showing the top 0-1.4 μm (a), middle 5.2-9.2 μm (b) and bottom 11.1-12.5 μm (c) segments of one WZ GaP nanowire with 12.5 μm length. Stacking faults are indicated by the red lines. Scale bars: 200 nm.

4.2.2 Effect of the temperature on the SF density

The growth temperature is a critical parameter in the control of the crystalline structure of the nanowires. Previous works on GaP nanowires grown in a MOVPE system showed predominant zinc blende crystal structure below 500°C, whereas at higher temperatures a mixture of domains with zinc blende and wurtzite was

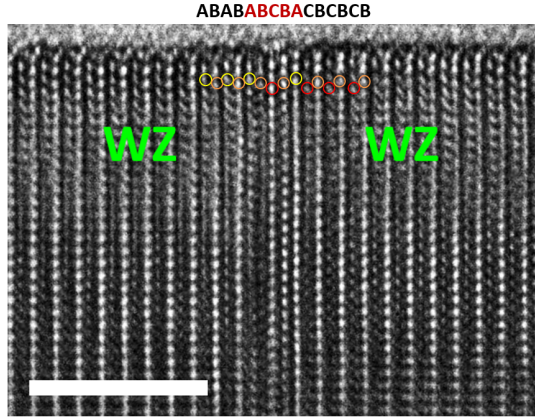


Figure 4.4: HRTEM image of one stacking fault consisting of a twinned ZB segment. Scalebar: 5 nm.

observed^{79,80}. In this thesis, the effect of the temperature on the crystal phase is investigated in the range 660-750°C, as illustrated in Fig. 4.5. The stacking fault density is obtained from the TEM imaging. The increase in the growth temperature results in a steep decrease in the stacking fault density from 50 SF/ μm to less than 1 SF/ μm above 720°C. In chapter 5 the role of the chemical potential in the switch between the WZ and ZB crystal phases will be discussed. The increase in the sample temperature reduces the chemical potential $\Delta\mu$ at the gold droplet⁸¹, reaching values lower than the critical supersaturation $\Delta\mu_C$, where the pure WZ growth is observed⁸².

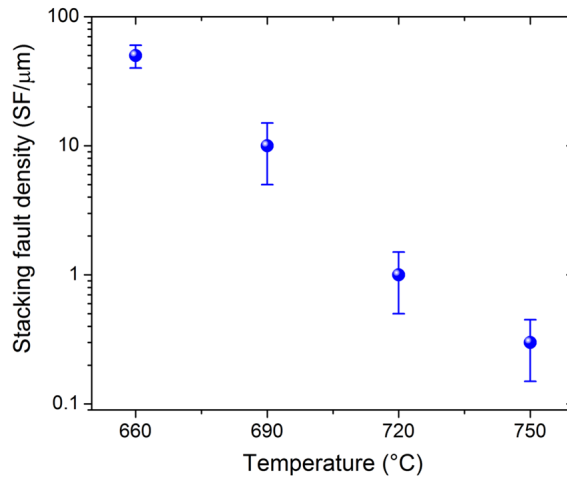


Figure 4.5: Stacking fault density in the nanowires as a function of the growth temperature.

4.2.3 HCl passivation

When the growth temperature increases, the decomposition of the precursors increases⁶⁴, favouring the lateral overgrowth of the nanowires, and tapering can be observed. To avoid tapering, the HCl gas is introduced during the nanowire growth²⁸. The reaction of TMG with HCl results in GaCl species with higher diffusion length due to the higher bond energy compared to the metalorganic species, with predominant cracking of the GaCl at the gold droplet⁸³. This could prevent the decomposition at the side surface of the nanowires which would result in radial growth, hence tapered nanowires. In Fig. 4.6a untapered GaP nanowires grown with a HCl molar fraction of $1.2 \cdot 10^{-4}$ are shown. When the HCl flow is reduced by a factor 2 strong tapering is observed, with the nanowire geometry that evolves to a wide pyramidal base with a narrower top section (Fig. 4.6b). When the HCl gas is removed, very short and irregular pyramids are observed, together with high substrate surface roughness due to 2D layer growth (Fig. 4.6c). Surface Chlorination is generally associated with a reduction in the 2D growth rate and in an increase of the nanowire growth rate⁸⁴. The increase in wire length, together with the critical reduction in the radial overgrowth and 2D layer growth show the passivation effect of the side surface of the nanowires from the Cl-species. Thus, the HCl flow plays a key role in the control of the nanowire morphology.

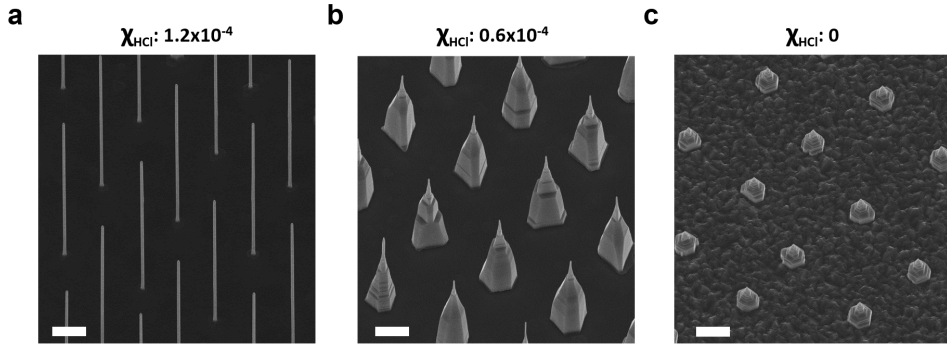


Figure 4.6: SEM images of the GaP nanowires grown using HCl molar fractions of $1.2 \cdot 10^{-4}$ (a), $0.6 \cdot 10^{-4}$ (b) and 0 (c) (tilting angle 30°). Scalebars: $2 \mu\text{m}$.

4.2.4 AlGaP shell

AlGaP shells are grown radially around the GaP core wires to passivate the surface states⁸⁵. The $\text{Al}_{0.4}\text{Ga}_{0.6}\text{P}$ shell lattice matches the core and no defects are nucleated from the interface (Fig. 4.7a). The core/shell structure is visible from the High Angle Annular Dark Field (HAADF) TEM image in Fig. 4.7c and the shell composition and thickness for the different samples have been determined from Energy-Dispersive X-ray (EDX) line scans as shown in Fig. 4.7d.

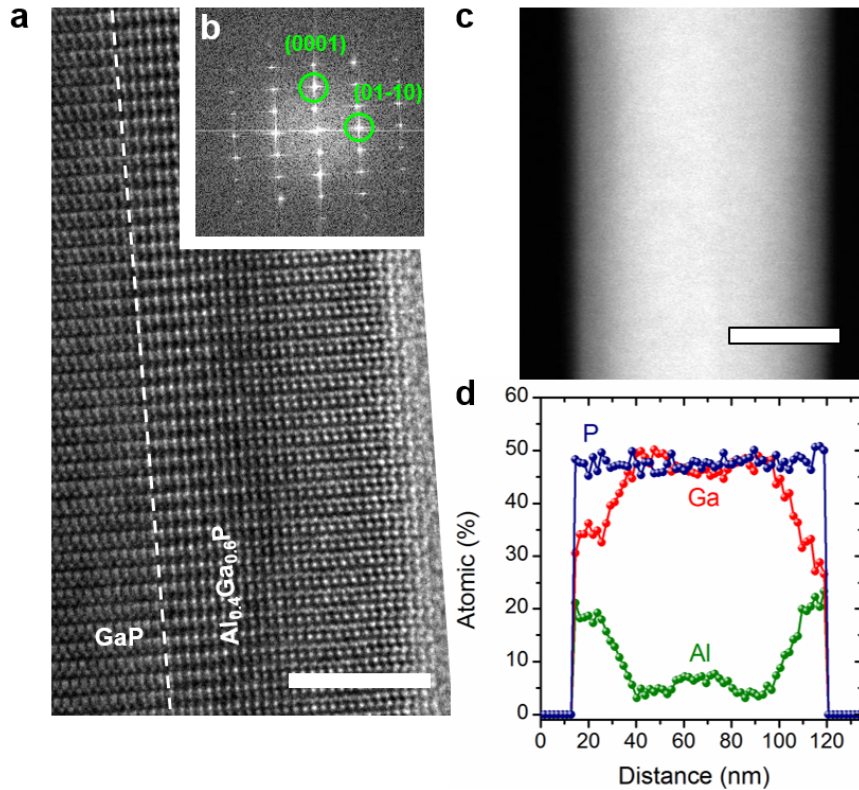


Figure 4.7: (a) HRTEM image showing the pure wurtzite crystal structure. Scalebar: 5 nm. (b) FFT image of the GaP nanowire in (a). (c) HAADF TEM image of a GaP/ $\text{Al}_{0.4}\text{Ga}_{0.6}\text{P}$ core/shell wire, showing the uniformity of the shell. Scalebar: 50 nm. (d) Energy dispersive X-ray (EDX) line scan taken perpendicular to the nanowire axis, showing the GaP/ $\text{Al}_{0.4}\text{Ga}_{0.6}\text{P}$ core/shell structure.

4.2.4.1 Rotation of the side facets

The resulting $\text{Al}_{0.4}\text{Ga}_{0.6}\text{P}$ shell is terminated by $\{2110\}$ facets, while the GaP core wire has $\{1100\}$ facets. This rotation of the side facets, already reported for the AlInP/GaAs system⁸⁶, as seen in Fig. 4.8, is observed for all samples.

As a result of this, the projected thickness of the shell varies across the nanowire producing a small *bump* in the EDX profile. The wire in Fig. 4.8 has a 10 nm thick $\text{Al}_{0.4}\text{Ga}_{0.6}\text{P}$ shell. Important to mention is that AlGaP is nearly lattice matched to GaP^{33} , and as a result no defects are generated in the shell.

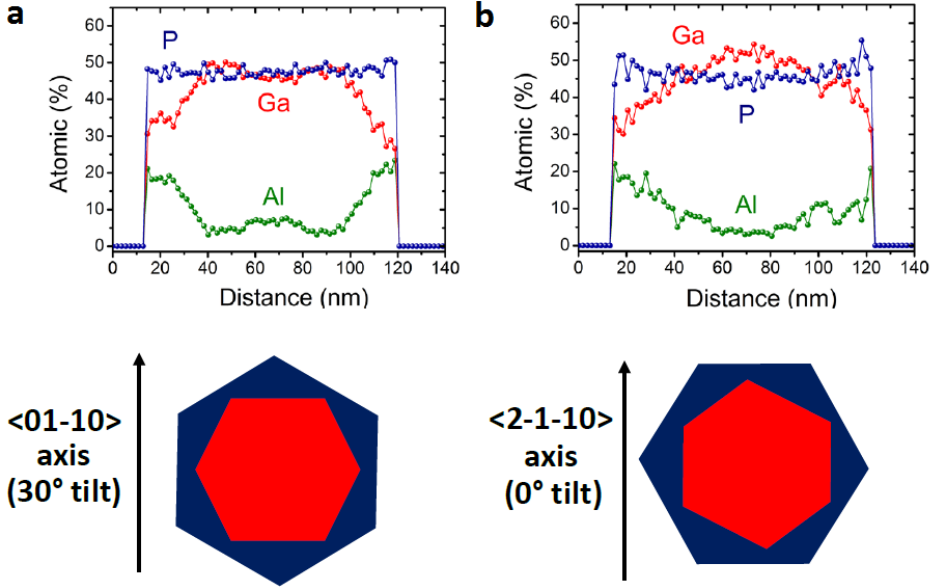


Figure 4.8: Energy dispersive X-ray (EDX) line scans taken perpendicular to the $\text{GaP}/\text{Al}_{0.4}\text{Ga}_{0.6}\text{P}$ nanowire long axis. The nanowire was rotated w.r.t. the incident electron beam direction towards the $\langle 01-10 \rangle$ (30° tilt) and the $\langle 2-1-10 \rangle$ (0° tilt) imaging axis. The schematic displays the rotation of the facets of the AlGaP shell (blue) with respect to the GaP core (red). The two, clearly different EDX profiles are in agreement with the different projected thicknesses of the AlGaP shell.

4.2.4.2 Top axial segment

During the growth of the AlGaP shell VLS growth of a top AlGaP axial segment is observed, as shown in the HDAAF image and in the EDX elemental maps in Fig. 4.9. Compared to the pure WZ structure of the GaP core, the AlGaP segment shows higher SF density due to the increased V/III ratio and lower growth temperature used to promote the uniform radial growth of the shell (Fig. 4.10).

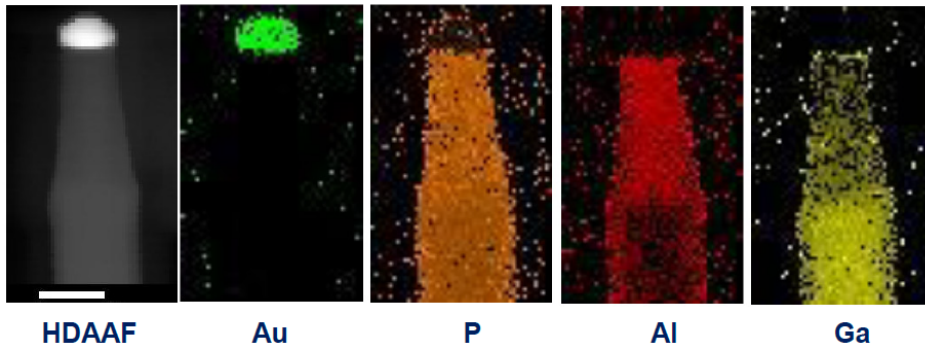


Figure 4.9: HAADF image and EDX elemental maps of a GaP/AlGaP core/shell nanowire. Scale bar: 50 nm.



Figure 4.10: TEM image of a GaP/AlGaP core/shell nanowire showing the mixed phase AlGaP top axial segment. Scale bar: 100 nm.

4.2.5 X-ray diffraction

The overall crystalline quality of the nanoimprint sample can be investigated on a macroscopic scale (in the millimeters range) using XRD measurements. With this technique it is also possible to determine the WZ GaP unit cell lattice parameters. In the scan in Fig. 4.11 the $(10\bar{1}\cdot l)$ peak series for the WZ wires and the $(\bar{2}\bar{2}4)$ ZB substrate peak are observed, while no extra peaks from polytype structures (ZB, 4H, 6C) are found. This, together with the narrow line width of the WZ peaks, which is limited by the resolution of the set-up, shows the high crystalline quality of the sample. The measured *a*- and *c*- lattice parameters for the WZ unit cell are respectively, 3.842 Å and 6.335 Å. Those values differ from the geometrical conversion of the ZB unit cell into the WZ one, showing an elongation of the WZ unit cell along the growth (*c*-) axis and a compression in the in-plane direction along the *a*-axes. This result is similar to what is found for the WZ phase of other III-V nanowires⁸⁷. More details on the WZ GaP crystal structure can be found in Ref.³².

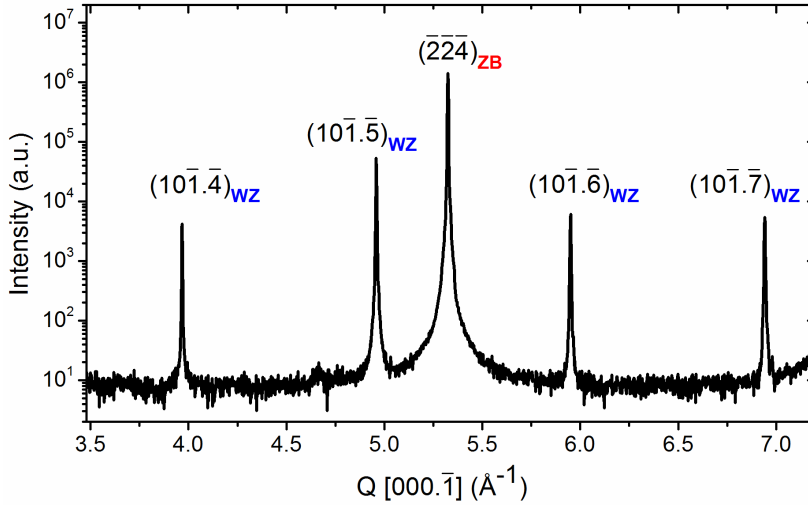


Figure 4.11: X-ray diffraction intensity along the crystal truncation rod through the $(\bar{2}\bar{2}4)$ substrate peak, which includes the $(10\bar{1}\cdot l)$ WZ peaks. The resolution-limited line widths of the WZ peaks and the absence of signal between the peaks show the high quality of the WZ material.

Chapter 5

Crystal phase control in GaP wires

For optical quantum information processing emission sources are needed, which can emit identical photons. This is a challenge, since quantum structures based on heterostructures always show variations in size and composition, leading to a spread in emission wavelength^{88,89}. With nanowires a new type of structure has become available, which is based on junctions between different crystal structures of identical chemical composition^{36,37,90}. Such advanced structures can behave as single photon sources³⁴. The development of nanowire homostructures formed by the combination of the ZB and WZ crystal phases has drawn a lot of attention in the last few years^{36,37,91}. In GaP material, electrons and holes can be efficiently confined in the WZ segment due to a predicted type I band alignment between WZ and ZB³¹. This would allow the growth of crystal phase quantum well (CPQW) and quantum dot (CPQD) structures in this material system³⁴. Large spontaneous polarization fields are, however, predicted for WZ GaP⁹², which can induce substantial surface charges across a thin ZB GaP segment embedded in WZ material⁹³. In this case the ZB segment will separate the electrons and holes and the thickness of this ZB segment determines the energy scales. It is therefore essential to control the thickness of the ZB segment at the monolayer level. In this chapter, we show the growth of defect-free and atomically sharp WZ/ZB interfaces in GaP nanowires. By controlling the flow and the supply time of the Ga precursor the length of the WZ and ZB segments can be tuned to achieve CPQWs along the nanowire axis. Furthermore, the growth of a WZ/ZB superlattice with constant WZ and ZB segment lengths is shown.

5.1 Growth of WZ/ZB interfaces

The ZB segments are grown in patterned arrays of 100 nm diameter WZ GaP nanowires defined by nanoimprint lithography⁷⁷. The SEM image of a typical sample in Fig. 5.1a shows the position-controlled growth of untapered GaP wires.

A schematic drawing of the WZ/ZB nanowire homostructures is illustrated in Fig. 5.1b. For the growth of these structures we use the following protocol. First, the growth of $\sim 2.6 \mu\text{m}$ WZ GaP stem is performed at 750°C under low V/III ratio (23), using $\chi_{\text{TMG}} = 7.42 \cdot 10^{-5}$, $\chi_{\text{PH}_3} = 1.71 \cdot 10^{-3}$, and $\chi_{\text{HCl}} = 1.22 \cdot 10^{-4}$, as discussed in chapter 4. A controllable crystal phase switching is induced by tuning the growth parameters as shown in Fig. 5.2a. The temperature values used in this thesis are the set point values at the thermocouple, which relate to the substrate *in-situ* temperature provided by the optical sensors inside the MOVPE reactor (aqua curve in Fig. 5.2a). Due to the partial decomposition of the phosphine below an effective temperature of 570°C (corresponding to a thermocouple temperature of $\sim 690^\circ\text{C}$)⁶⁴, the substrate *in-situ* temperature values are used in the calculation of the effective precursor flows. In order to have a clean switch to the ZB phase nucleation, the gallium flow is stopped, while the growth temperature is reduced to 600°C and the PH_3 pressure is increased to an effective molar fraction $\chi_{\text{PH}_3} = 2.04 \cdot 10^{-3}$ ^{76,79,80}. When the temperature is stabilized the gallium flow is opened again and the growth resumes using an effective V/III ratio of 67. No HCl gas is provided during ZB growth.

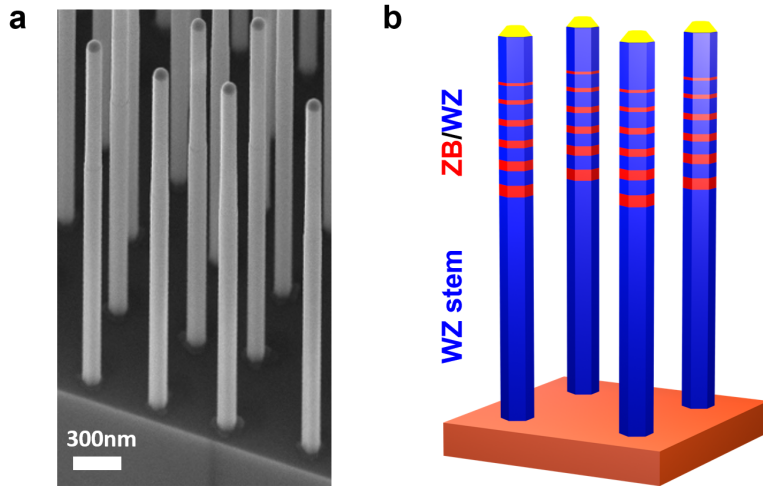


Figure 5.1: (a) SEM image of the GaP nanowires grown in the nanoimprint pattern (tilting angle 30°). (b) Schematics of the stacking of the crystal phases in the nanowires. After the growth of WZ stem multiple ZB segments are grown along the nanowire.

Once the ZB segment growth is finished, the gallium flow is stopped, and the temperature is increased to 750°C , where the WZ growth is resumed. We note that phosphine is supplied during the entire recipe to create a background pressure in order to prevent evaporation of the nanowires at these elevated temperatures. A resulting wire grown with the former procedure is shown in the HRTEM image in Fig. 5.2b. The pure ZB segment in the WZ nanowire is visible, with atomically sharp transitions between the WZ/ZB/WZ crystal structures and no stacking faults in both crystal phases. During the ZB growth the development of (non-vertical) $\{111\}$ side facets is generally observed⁹⁴.

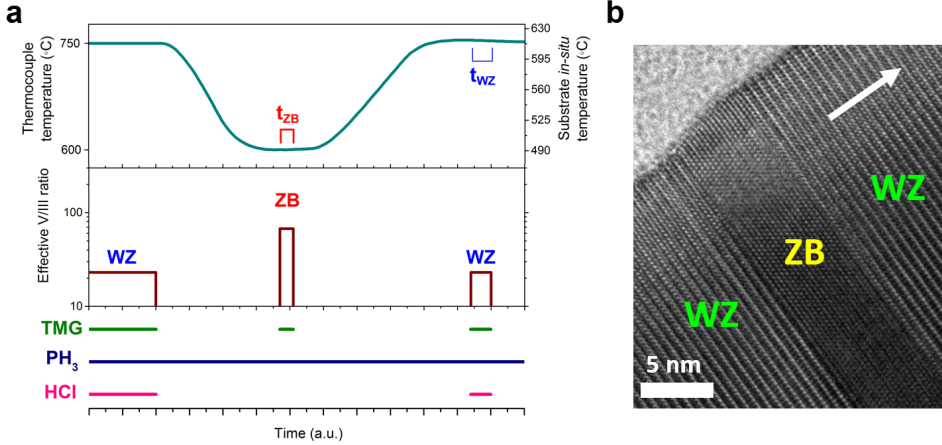


Figure 5.2: (a) Temperature profile (thermocouple and substrate *in-situ* values), effective V/III ratio, and sketch of the supply of the precursor gases during growth. (b) HRTEM picture of one WZ-ZB-WZ sequence showing defect-free crystal phases with atomically sharp interfaces. The arrow indicates the growth direction.

5.2 Control of the ZB length

In order to tune the emission wavelength of the quantum structures it is essential to have control of the dimensions. For obtaining a good level of control, a low growth rate is beneficial. We first study the growth dynamics of the ZB segment as a function of the precursor flows. We observe that a change of the PH_3 flow does not affect the growth rate, but that the Ga pressure has a large effect.

5.2.1 Effect of the Ga precursor

The nanowire presented in Fig. 5.3 is grown by repeating the process shown in Fig. 5.2a and by using a fixed growth time for the WZ segment ($t_{WZ} = 90$ s). During the ZB growth the gallium flow ($\chi_{TMG} = 3.04 \cdot 10^{-5}$) is supplied for an amount of time (t_{ZB}) varying from 3.1 s to 0 s. The lengths of the ZB segments are plotted in Fig. 5.4a as a function of the supply time of the gallium precursor for different TMG molar fractions. The dashed horizontal line indicates the shortest stacking sequence for the ZB phase (ABC stacking) in a WZ wire, which is equal to 0.945 nm. The error bars refer to a data set of 4 wires per sample.

When only the temperature is changed (corresponding to 0 seconds growth of ZB phase) no ZB growth is indeed observed, proving that a droplet refilling time t_{REF} is needed to start the ZB nucleation. Here, the refill time is defined as the linear extrapolation of the plots in Fig. 5.4a to zero ZB length. After droplet refilling, a growth rate $R_{ZB} = 7.5 \pm 0.6$ nm/s is measured at $\chi_{TMG} = 3.04 \cdot 10^{-5}$. Furthermore, reduction in the droplet diameter is observed after the growth of the first ZB segment ($t_{ZB} = 3.1$ s), indicating a depletion of Ga content in the gold droplet after the first cooldown/warm-up process. Instead, in the following ZB segments the change in diameter is minimum. Across the set of samples studied

grown using different ZB growth conditions, the shrinking of the droplet after the first ZB growth is observed in most of the wires.

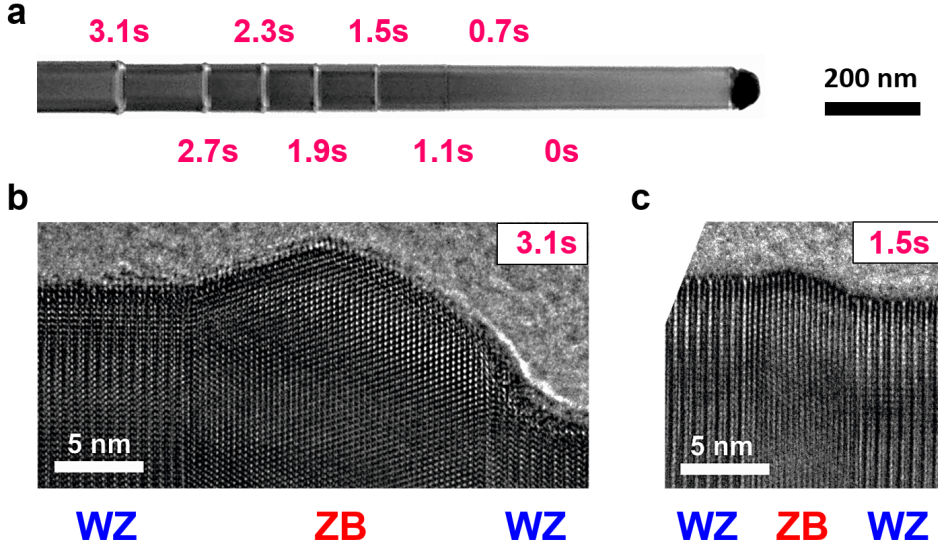


Figure 5.3: (a) TEM image of a nanowire with ZB grown for a variable time t_{ZB} ($\chi_{TMG} = 3.04 \cdot 10^{-5}$), separated by WZ segments grown for fixed $t_{WZ} = 90$ s. (b-c) HRTEM images of the nanowire in (a) for segments grown for $t_{ZB} = 3,1$ s (b) and $t_{ZB} = 1,5$ s (c), showing defect-free crystal phases with atomically sharp interfaces.

By lowering the Ga molar fraction down to $\chi_{TMG} = 1.35 \cdot 10^{-5}$ the growth rate R_{ZB} decreases to 2.6 ± 0.3 nm/s, while the refill time increases up to 3.9 ± 0.2 s (Fig. 5.4b-c). A critical transition is observed when the Ga molar fraction falls below $1.35 \cdot 10^{-5}$, where a step increase in the growth rate occurs while the refill time still follows a monotonic (increasing) trend. We speculate that at the lowest Ga molar flows the droplet is slowly filled with Ga and finally reaches a superfilled state, resulting in higher supersaturation, hence in higher growth rate during the ZB growth⁸⁰. This is unwanted, since it reduces the control over the ZB growth. The superfilled state of the droplet could also induce a change in the droplet contact angle. However, as it will be discussed in section 4, the ZB nucleation occurs at the center of the droplet rather than at the wire edge. Thus, a change in contact angle does not affect the growth kinetics. The growth rate and refill time appeared independent of the PH_3 flow (not shown), indicating that the ZB growth occurs in a Ga-limited regime.

Up to a length of 15 nm the ZB phase is generally defect-free. For longer segments, twin defects are present, as shown in Fig. 5.5a. After the nucleation of few twin defects, the growth evolves into a mixed ZB-WZ phase (Fig. 5.5b), with no control of the crystal phase in this regime. This behavior can be explained in terms of change in the supersaturation $\Delta\mu$ at the gold droplet, as discussed in section 4. Reduction in Ga content is often observed during ZB growth (see Fig. 5.3a). Thus, assuming that a progressive reduction of Ga content occur during ZB

nucleation, $\Delta\mu$ decreases, approaching the critical supersaturation $\Delta\mu_C$. Thereby, the probability for the nucleation of a WZ monolayer increases, hence twin defects can be observed. For a longer growth time, the supersaturation further decreases and mixed phase is observed.

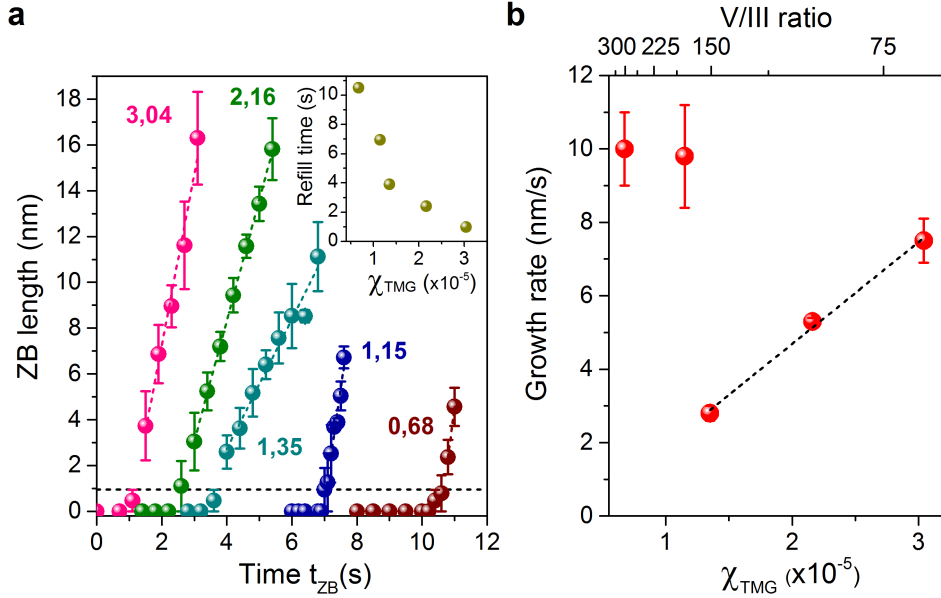


Figure 5.4: (a) ZB length as a function of the Ga supply time t_{ZB} for different TMG molar fractions χ_{TMG} , indicated in units of $1 \cdot 10^{-5}$. The dashed horizontal line indicates the shortest stacking sequence for the ZB phase (ABC stacking) in a WZ wire, which is equal to 0.945 nm. Inset: refill time t_{REF} as a function of the Ga molar fraction χ_{TMG} . (b) ZB growth rate as a function of the Ga molar fraction χ_{TMG} . Statistics are performed measuring 4 nanowires via HRTEM.

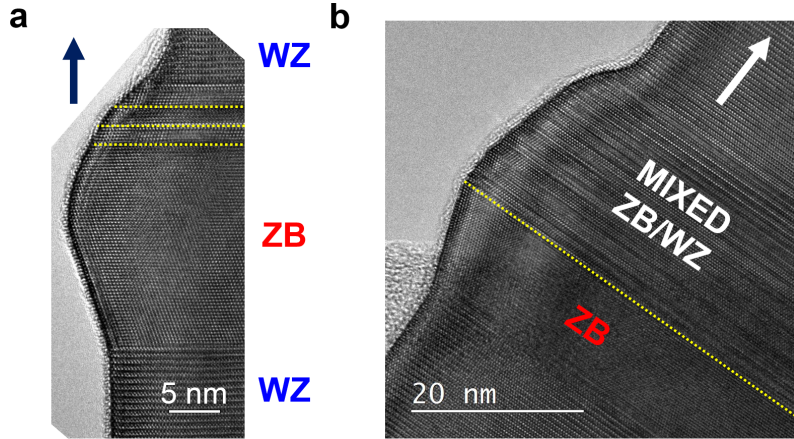


Figure 5.5: (a) HRTEM image of a nanowire showing the ZB phase followed by twin defects indicated by the dashed lines. (b) HRTEM image of a nanowire grown with the combination of ZB with the mixed ZB/WZ structure. The arrows indicate the growth direction.

5.2.2 Approaching the ML control

To investigate the possibility for monolayer-controlled ZB growth we use the lowest ZB growth rate of $\sim 7\text{-}9$ ML/s, which is obtained with a Ga molar fraction $\chi_{TMG} = 1.35 \cdot 10^{-5}$. The Ga precursor is switched on for decreasing time intervals between 4.6 s and 3.4 s with time steps of 0.1 s. In Fig. 5.6 the number of ZB monolayers as a function of the Ga supply time t_{ZB} for four different nanowires are shown. The following observations can be made. First, several monolayers rather than single monolayers nucleate on average during every 0.1 s time interval. Recently, in-situ TEM studies in a ultra-high vacuum TEM showed that GaP nanowire growth occurs by the addition of single monolayers, providing evidence that VLS growth proceeds in a single layer-by-single layer mode⁹⁵. This indicates that during the 0.1 s time interval, which is the resolution limit of our MOVPE machine, several monolayers are formed. Ideally, monolayer control might be achieved with shorter switching time (smaller than 0.1 s). On the other hand, this would be limited by the fact that small fluctuations, in the order of 0.1 s, in the refill time would have a large effect on the number of ZB monolayers grown for a given ZB growth time. Second, in most of the investigated wires the growth begins with 5-7 MLs, as shown for NW2-3. Occasionally the ZB growth starts with 3 MLs, which is the shortest possible ZB stacking segment, as illustrated for NW1-4. We believe that wire-to-wire variations in the supersaturation at the gold droplet induce variations in the refill time and in the initial ZB segment length. Third, close to the refill time t_{ZB} the ZB growth rate is $\sim 20\text{-}26$ ML/s, which is higher than the value of $\sim 7\text{-}9$ ML/s observed for longer growth times. Thus, even though the ZB growth rate has been reduced by lowering the Ga flow, the former results show that growth of homostructures with control at the monolayer level is still challenging.

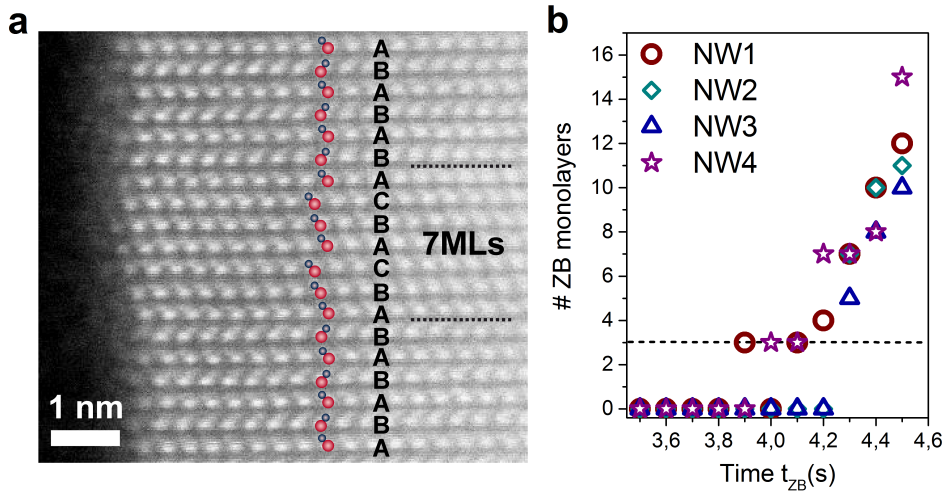


Figure 5.6: (a) HR-STEM image showing controlled ZB segment length of 7 ML. The red and blue circles indicate the Ga and P atoms, respectively. (b) Number of ZB monolayers as a function of the Ga supply time t_{ZB} for four different nanowires grown with $\chi_{TMG} = 1.35 \cdot 10^{-5}$. The dashed line corresponds to the shortest stacking sequence for the ZB phase in a WZ wire, which has a length of 3 MLs (ABC stacking).

5.3 Tuning the WZ growth

In a similar way the formation of the WZ phase has been investigated. The growth rate of the WZ phase is estimated by growing WZ segments for different time intervals separated by 10 nm ZB markers, as shown in Fig. 5.7. The lengths of the WZ segments are plotted in Fig. 5.7c as a function of the Ga supply time. The error bars refer to a data set of 4 wires per sample. When a Ga molar fraction of $\chi_{TMG} = 7.42 \cdot 10^{-5}$ is used, a constant WZ length of 7 ± 3 nm is observed below the offset time $t_{OFF} = 14 \pm 2$ s, while above this value an increase in the WZ segment length is observed (blue curve in Fig. 5.7c). Instead, when the Ga molar fraction is reduced to $\chi_{TMG} = 5.40 \cdot 10^{-5}$ the offset time t_{OFF} increases to around 100 s (dark red curve in Fig. 5.7c). The non-zero WZ length for growth times shorter than the offset time results from so-called *parasitic* WZ growth, i.e. growth during the change in temperature from 491°C to 614°C, or vice versa, in the absence of Ga supply. Thus, residual gallium in the gold droplet can induce the growth of the WZ crystal structure⁹¹. No intentional WZ growth is observed for times shorter than the offset time ($t_{WZ} < t_{OFF}$). Two mechanisms may be involved in this regime. First, due to the small amount of Ga supplied, the Ga supersaturation in the gold droplet required for the WZ growth remains below a critical value, and hence no intentional WZ growth occurs⁹⁶. Second, re-evaporation of Ga from the droplet due to the high growth temperature could further reduce the supersaturation in the droplet. In Fig. 5.8 four different wires grown with $\chi_{TMG} = 7.42 \cdot 10^{-5}$ are shown. Small fluctuations in both offset time ($t_{OFF} = 14 \pm 2$ s) and growth rate ($R_{WZ} = 2.4 \pm 0.2$ nm/s) are observed, while a spread in the parasitic WZ length can be seen, with values ranging from 4 nm to 11 nm. Since the relative spread in WZ segment length is larger in these WZ/ZB structures compared to the spread in length of pure WZ GaP stems (without ZB segments), which is about 10%, we can conclude that the large spread originates from the crystal phase switch process. The length of the ZB markers associated with the WZ segments in Fig. 5.8a are plotted in Fig. 5.8b. The wires (NW1-4) with the shortest ZB segment lengths shows the longest *parasitic* WZ segments, while the wires (NW2-3) with the longest ZB segments relates with the shortest *parasitic* WZ growth. Since the volume of the droplet is constant, the Ga content in the droplet remains constant during the growth cycle. Thus, when less Ga is used for the ZB growth, then there is more Ga available for the nucleation of the WZ phase, and vice versa. The spread in WZ length possibly relates to differences in diameter. Thicker wires have more Ga in the droplet which can precipitate, leading to longer WZ segments. The bigger diameter also results in a longer refill time, and, as a consequence, shorter ZB segments are observed for fixed growth time t_{ZB} .

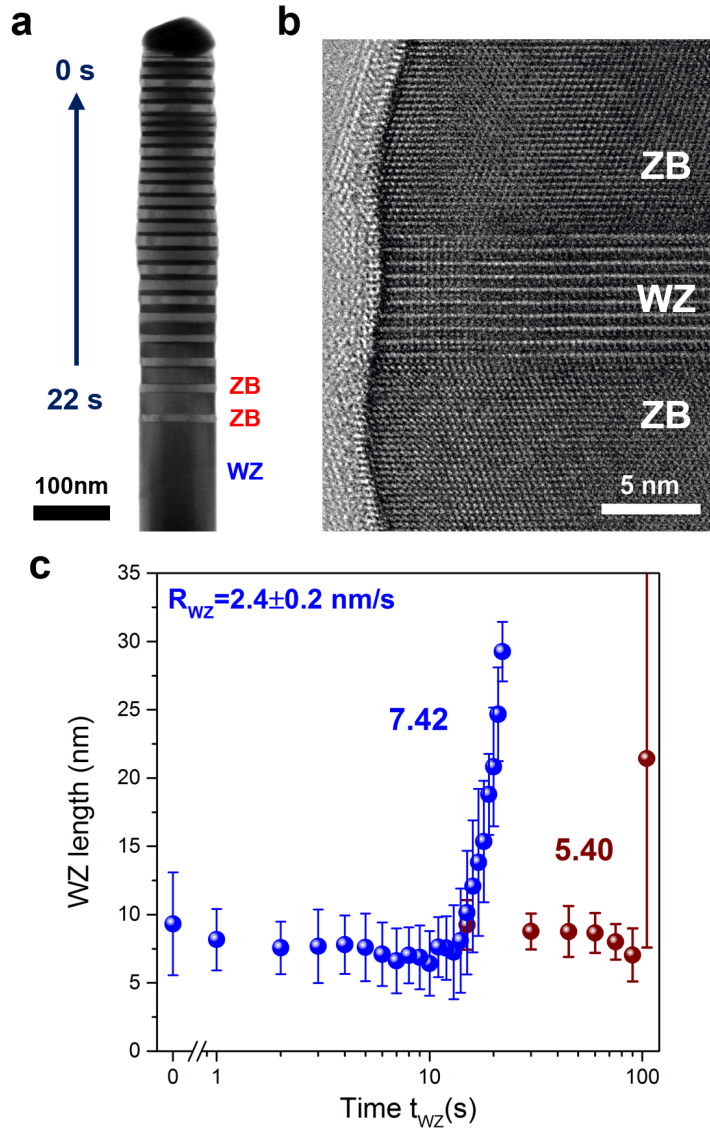


Figure 5.7: (a) TEM image of a nanowire with WZ segments grown for different Ga supply times t_{WZ} using a TMG molar fraction $\chi_{TMG} = 7.42 \cdot 10^{-5}$. The 10 nm long ZB segments are used as markers. (b) HRTEM image showing the *parasitic* WZ in between of the two ZB segments. (c) WZ length as a function of t_{WZ} for two different TMG molar fractions χ_{TMG} , indicated in units of $1 \cdot 10^{-5}$. Statistics are performed measuring 4 nanowires via HRTEM.

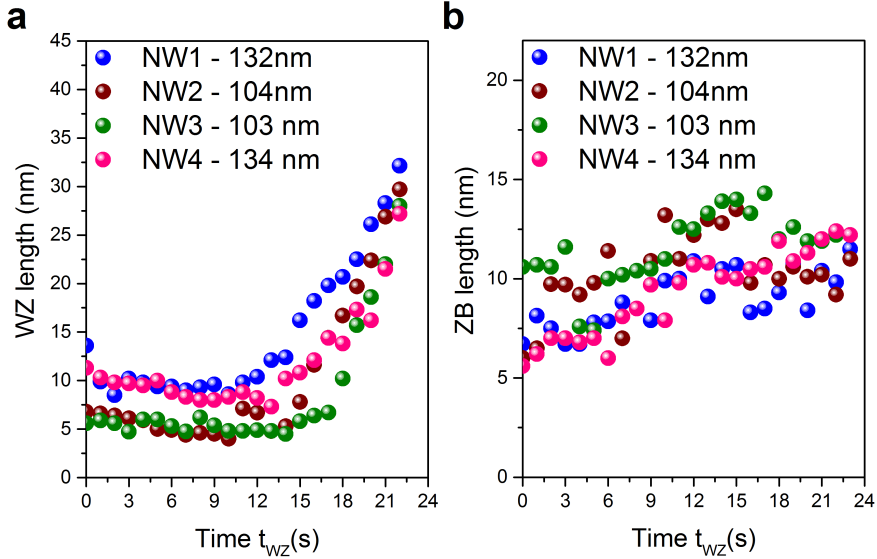


Figure 5.8: (a) WZ length as a function of t_{WZ} for four different nanowires grown with $\chi_{TMG} = 7.42 \cdot 10^{-5}$. (b) Length of the ZB markers associated with the WZ segments in (a).

5.4 Nucleation model for the WZ and ZB growths

The nucleation model discussed in this section is based on the work of dr. L.F. Feiner and dr. S. Breuer⁸².

In nanowires with small diameters nucleation generally occurs at the triple-phase line (TPL) at the wire edge⁹⁶. In this regime, the WZ phase will form if the supersaturation $\Delta\mu$ is higher than a critical value $\Delta\mu_{TPL}$, i.e. large enough to ensure that the free energy of formation of a WZ nucleus, ΔG_{WZ}^{TPL} , is smaller than the ZB nucleus, ΔG_{ZB}^{TPL} ⁹⁶. However, for sufficiently large diameter of the nanowire the larger number of potential nucleation sites in the interior (C) part of the droplet-nanowire interface, scaling as R^2 , (where R is the radius of nanowire) as compared to the number of sites at the TPL, scaling as R, may compensate for the unfavorable difference between ΔG_{WZ}^{TPL} and ΔG_{ZB}^C , and nucleation at the center of the droplet then becomes predominant. In this regime, the ZB phase will be grown for values of $\Delta\mu$ higher than a critical value $\Delta\mu_C(R)$, i.e. sufficiently large to ensure that the difference between ΔG_{WZ}^{TPL} and ΔG_{ZB}^C is small enough to make such compensation possible⁸². Intuitively, for larger diameter wires, approaching the bulk limit, the ZB phase should be formed.

As discussed in chapter 1, the interplay of many parameters affects the supersaturation at the gold droplet during growth. In particular, the growth temperature plays a key role in the purity of the WZ phase, as shown in chapter 4. Furthermore, in the crystal switch recipe discussed in the previous sections the transition between the pure WZ/ZB phases is mainly driven by the change in temperature.

The transition from WZ growth to ZB growth is induced by lowering the temperature from 750°C to 600°C, which corresponds to an increase in $\Delta\mu$ ⁸¹ and leads to a crossing of the critical value $\Delta\mu_C$ for the ZB nucleation. This is in clear contradiction to the behavior expected for nucleation at the TPL from the nucleation model mentioned above⁹⁶, according to which such a transition should be induced by lowering instead of raising $\Delta\mu$. We therefore propose that the transitions between WZ and ZB growth observed in our growth experiments are due to switching between TPL-nucleated WZ growth and C-nucleated ZB growth. Thus, WZ and ZB growth occur under the following conditions, respectively:

1. WZ growth: $T = 750^\circ\text{C}$, $\Delta\mu_{TPL} < \Delta\mu < \Delta\mu_C$;
2. ZB growth: $T = 600^\circ\text{C}$, $\Delta\mu_C < \Delta\mu$.

With this model we can qualitatively explain the formation of ZB at low temperature and WZ at high temperature. In addition, the refill time for ZB growth and the offset time for WZ growth are explained as the Ga supply time needed to bring the supersaturation $\Delta\mu$ above the critical values $\Delta\mu_C$ and $\Delta\mu_{TPL}$, respectively.

5.5 WZ/ZB superlattice

For the formation of a controlled WZ/ZB superlattice it is important to fine-tune the temperature and precursor flows to ensure that the droplet is always kept in a refilled (close to equilibrium) condition. In case that this situation is not fulfilled, a stable crystal switch process cannot be guaranteed. The growth of a WZ/ZB superlattice³⁷ is performed by stacking multiple segments with a fixed growth time for both the ZB and WZ crystal phases. The nanowire superlattices shown in Fig. 5.9 and in Fig. 5.10 are from two different samples grown using the same parameters. For the WZ phase $\chi_{TMG} = 5.40 \cdot 10^{-5}$ and $t_{WZ} = 6$ s are used, while for the ZB phase $\chi_{TMG} = 3.04 \cdot 10^{-5}$ and $t_{ZB} = 2$ s are chosen. By selecting this set of parameters, only a partial refill of the droplet occur during the high temperature growth. Both samples show high purity for the WZ and ZB crystal phases, with a high degree of reproducibility of the growth recipe. The patterned substrate is a key factor in order to control the growth parameters for the crystal phase switching, allowing reliable and reproducible results. However, differences in the WZ and ZB segment lengths are visible.

The wire in Fig. 5.9 is constant in diameter, and shows a constant WZ/ZB ratio for the segment lengths L of 3:1, with $L_{WZ} = 9.3 \pm 0.3$ nm and $L_{ZB} = 2.8 \pm 0.8$ nm. The crystal switch in the former wire follows the expected equilibrium growth dynamics. Instead, in the nanowire in Fig. 5.10 the difference in lengths between the ZB and WZ segments increases with the segment number. In Fig. 5.10d the sum of the WZ+ZB segment lengths is plotted. The reduction in the total segment length after the first three ZB cooldown/warm-up steps correspond to a reduction of the Ga content in the gold droplet, until the equilibrium value in the total length of 13 nm is reached. The latter value is identical to the one found in the equilibrium superlattice in Fig. 5.9.

In this regime, a progressive reduction in the ZB length down to a value of around 4 nm is present. Since the amount of Ga in the droplet is constant, the

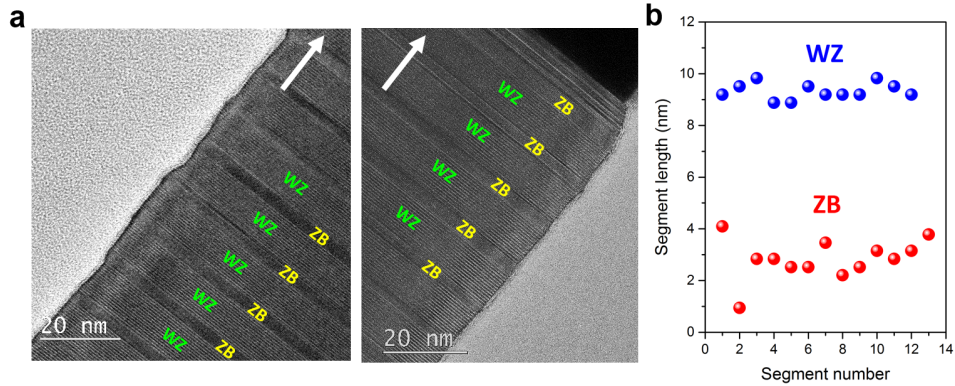


Figure 5.9: Superlattice growth at the equilibrium. (a) HRTEM images of one nanowire showing a superlattice (13 ZB/WZ segments) with a ratio of the WZ and ZB segment lengths of 3:1. The arrows indicate the growth direction. (b) Plot of the WZ and ZB segment lengths as a function of the segment number.

gradual decrease in the ZB length in Fig. 5.10c is probably related to an increase in the ZB refill time t_{REF} . Similarly to the wire shown in Fig. 5.8, when the amount of Ga consumed during the *parasitic* WZ growth increases, yielding to longer WZ segments, a lower amount of Ga is available for the ZB growth, which results in longer refill time and shorter ZB segments. This behavior demonstrates how, in a regime of partial refill of the droplet, large deviations from the equilibrium segment lengths can occur, possibly due to wire to wire differences in the supersaturation at the gold droplet. The bright/dark contrast in the ZB sections in Fig. 5.10a is associated with different crystal orientations of the two twin-related ZB crystal structures grown in the WZ phase (ABAB|ABCABC|ABAB and ABAB|CABCAB|ABAB). From the dark/bright contrast it is easy to observe the decrease of the ZB segment length.

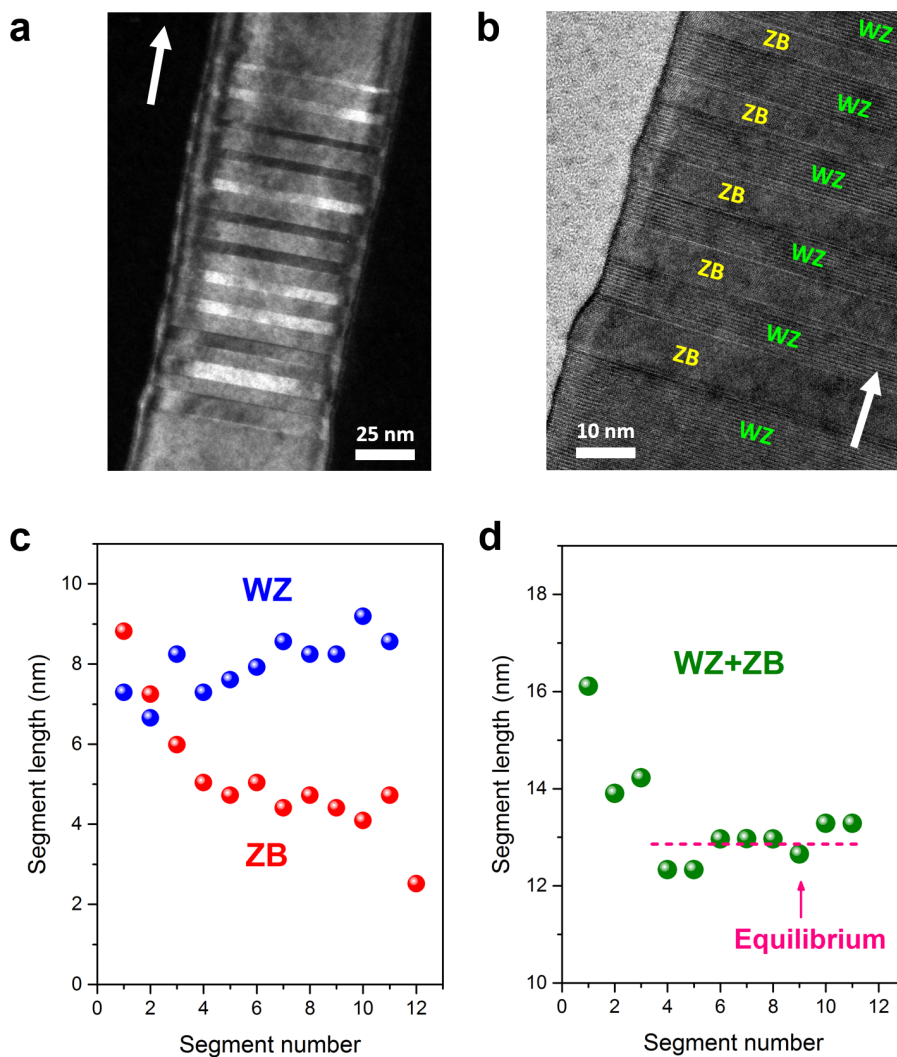


Figure 5.10: Superlattice toward the equilibrium growth. (a-b) Dark-field TEM image (a) and HRTEM image (b) of one nanowire showing a superlattice (12 ZB/WZ segments). The arrows indicate the growth direction. (c) Plot of the WZ and ZB segment lengths as a function of the segment number. (d) Plot of the sum WZ+ZB lengths as a function of the segment number.

5.6 Conclusion and applications

The crystal phase switch method developed in this thesis allows the growth of atomically sharp and single crystalline ZB/WZ interfaces along the nanowire length, with positions and sizes of the junctions controlled by the supply of the Ga precursor. Stable growth of ZB segments with lengths up to 15 nm and of WZ sections with lengths larger than 4 nm can be obtained in a reproducible way by maintaining the droplet in a refilled state. Instead, deviations from the equilibrium growth can occur for a partial refill of the droplet, leading to pure crystalline but uncontrolled crystal phase switch. The former limits in the maximum/minimum ZB/WZ segments length and the fluctuations in the segment lengths due the ZB/WZ refill/offset times reduce the flexibility of this growth method.

Various applications can benefit from the control of the crystal phase structure. In GaP wires grown with CPQWs sharp emission lines are observed (not shown), with energies defined by the addition of single ZB monolayers⁹⁷. The controlled growth of multiple identical quantum wells at defined positions within the same nanowire may provide a route to studying entangled photons in solid state quantum system⁹⁸. In nanowires Fabry-Pérot modes are often observed⁹⁹. The reflectivity of the end facets of the wire can be increased by using strain-free Bragg mirrors made of WZ/ZB superlattices¹⁰⁰. The latter structure can also be used as phonon-scattering medium to enhance the thermoelectric properties of those nanowires-based devices³⁵. Furthermore, core/shell heterostructures made of GaP core and group IV shell¹⁵ would result in crystal phase quantum rings in Silicon^{15,101,102} and Germanium, opening up new possibilities in the low-cost highly integrated optical interconnects⁷⁰.

Chapter 6

Optical characterization of WZ GaP wires

In this chapter, the optical measurements performed on the WZ GaP wires using photoluminescence (PL) and photoluminescence excitation (PLE) spectroscopy are presented. We show that, although the transition matrix elements for the band gap transition are predicted to be very weak at the Γ point, the WZ GaP nanowires still features a very rich photoluminescence spectrum. For the interpretation of the spectrum, the difficulty is that except for the band structure calculations^{31,45}, no material parameters, such as e.g. experimental data for the fundamental gap, the spin-orbit splitting, the crystal field splitting, or the binding energies of the donor, the acceptor, or the exciton, are known. To start our interpretation, we first need to attribute few features of the optical measurements with a high level of confidence, for which we have selected the donor-acceptor pair (DAP) recombination^{56,103}, the short lifetime⁷⁷, the observed band-filling^{47,56,104}, and the phonon replicas^{52,105,106}. Next, all the remaining spectral properties are fit into the former starting point, providing further confirmation of the interpretation proposed.

The chapter is organized with the following structure: first the experimental results are presented, followed by the discussion and interpretation of the optical data. The PL-PLE measurements are performed at 4K, unless stated differently in the figures caption.

6.1 Optical data: low excitation power (below 1 W/cm²)

In order to verify the direct nature of the band gap of WZ GaP, the wires are studied with low-temperature micro-PL using the CW-laser diode and the pulsed-laser diode for the excitation (spot with FWHM $\sim 1 \mu\text{m}$). The values for the excitation power density used in this thesis are averaged over 100 ms time. For the optical measurements, e-beam defined nanowire array samples are used with

a wire-to-wire spacing of $1.0 \mu\text{m}$ and patterned area of $25 \mu\text{m} \times 25 \mu\text{m}$, as shown in Fig. 6.1. Since the absorption cross-section of the nanowire is larger than the wire diameter¹⁰⁷, the optical emission from few nanowires is collected during the measurements. The emission intensity and radiative lifetime of the WZ nanowires are compared with a ZB (001) bulk GaP sample as a reference.

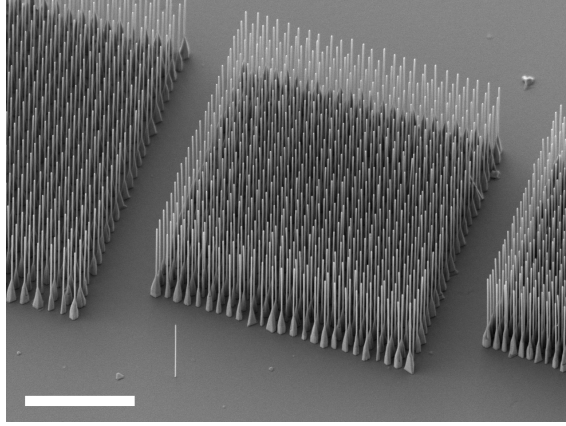


Figure 6.1: SEM image of GaP/Al_{0.4}Ga_{0.6}P core/shell nanowire arrays grown from Au droplets positioned by electron beam lithography with constant diameter of 100 nm (tilting angle 30°). The central array corresponds to 1 μm pitch. Scalebar: 10 μm .

6.1.1 PL spectra

The PL spectrum of the ZB GaP substrate in Fig. 6.2a exhibits two main peaks at 2.317 and 2.268 eV, corresponding to the A-line, which originates from excitonic emission from isoelectronic nitrogen impurities on P lattice sites, and its phonon-replica⁵⁴. The GaP/Al_{0.4}Ga_{0.6}P core/shell nanowires show the strongest emission at 2.088 eV (=594 nm) with a full width at half maximum (FWHM) of 29 meV, together with a wider and less intense peak at 2.040 eV (=607 nm) with a FWHM of 53 meV and two broad emissions at 1.910 and 1.650 eV. Bare WZ GaP nanowires show identical PL spectra, only with slightly lower intensity. To ensure that this emission originates from the wires and not from the substrate, nanowires are transferred from a substrate patterned by nano-imprint, into a PDMS¹⁰⁸ film coated with a titanium/gold back mirror, yielding similar results.

The spectra in Fig. 6.2a are obtained under identical experimental conditions so that we can quantitatively compare the PL intensity of the WZ wires and that of the ZB substrate. In Fig. 6.2b the integrated PL emission of the main ZB peak at 2.317 eV is compared to that of the main WZ wire peak at 2.088 eV for different wire diameters. The WZ PL intensity increases with wire diameter, due to increased volume, and levels off at the largest diameters. It is important to note that the integrated PL emission of WZ wires (80 nm diameter) is 65 times higher than that of the ZB GaP(001) substrate. This represents a lower limit of the enhancement factor of the WZ PL intensity, since this value is not corrected for

the probed materials volume. Note that the wires cover less than 1 % of the surface area, and moreover, the in and out coupling of light from the microscope objective is much better for a planar substrate compared to vertical nanowires¹⁰⁹. We have used a high quality ZB GaP(001) substrate as a reference, since the phonon assisted band-to-band emission of a GaP(111) substrate, observed at 2.280 eV at higher excitation power, is below the detection limit under these measurement conditions.

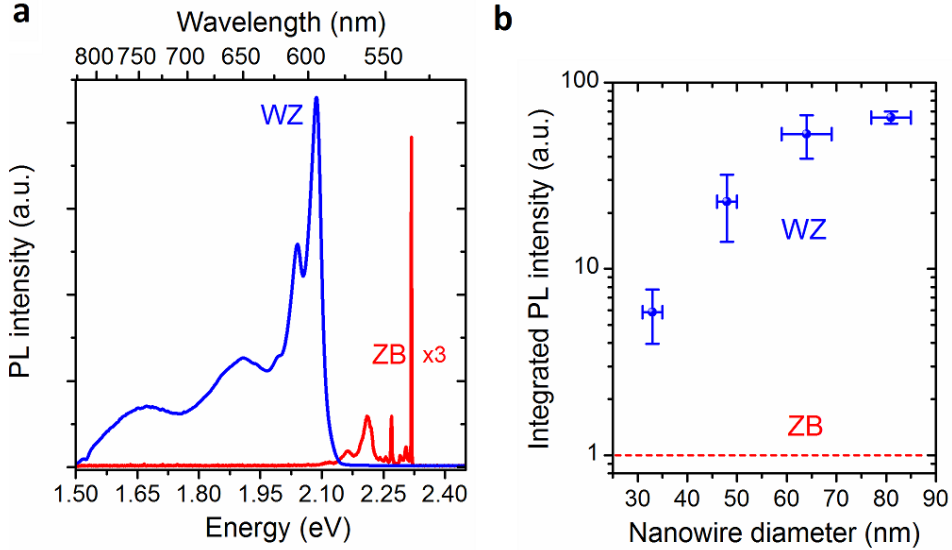


Figure 6.2: (a) Photoluminescence spectra of a ZB (001) GaP substrate (red spectrum) and of WZ GaP/Al_{0.4}Ga_{0.6}P nanowires (blue spectrum). For both spectra a CW-excitation (405 nm) with a power of 0.6 W/cm² is used. (b) Integrated PL emission of the main ZB substrate peak at 2.317 eV (red line) is compared to that of the main WZ wire peak at 2.088 eV for different nanowire core diameters (blue data points). All measurements are performed at 4K.

6.1.2 Time-resolved PL

Time-resolved PL measurements on WZ GaP/Al_{0.4}Ga_{0.6}P core/shell nanowires as well as on ZB bulk GaP are shown in Fig. 6.3. A long lifetime of 254 ± 3 ns is obtained for the A-line of the ZB bulk GaP, which is in the typical range for an indirect band gap transition. In strong contrast, a lifetime of 0.78 ± 0.01 ns is observed for the WZ core/shell nanowires, which compares favorably to lifetimes reported for direct band gap semiconductor like GaAs¹¹⁰.

In order to rule out any surface-related decay process, we have studied the PL intensity and lifetime of core/shell nanowires as a function of the Al_{0.4}Ga_{0.6}P shell thickness. Fig. 6.3b shows that a thin shell (7 nm) increases the PL intensity by a factor of 1.5, but increasing the shell thickness further (up to 60 nm) has no major effect on the intensity. The small increase of the intensity indicates

that surface states have only a minor effect on the optical properties of the wires. The intensity increase for the thickest shell of 72 nm is explained by enhanced absorption/emission of the wire, since the lifetime is unaffected. The temporal evolution of the PL intensity is independent of the shell thickness and the decay time is ~ 0.8 ns for all samples.

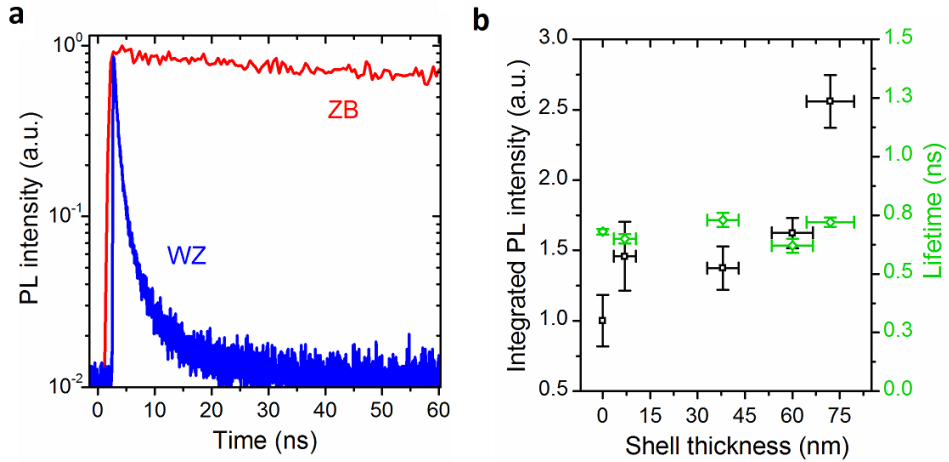


Figure 6.3: (a) Time resolved measurements showing a fitted lifetime of 254 ns for the ZB substrate and 0.78 ns for the WZ wires, demonstrating the direct nature of the WZ GaP semiconductor material. (b) Integrated PL intensity and lifetime of the WZ wire peak at 2.088 eV as a function of the $\text{Al}_{0.4}\text{Ga}_{0.6}\text{P}$ shell thickness. All measurements are performed at 4K.

6.2 Optical data: medium-high excitation power (above 1 W/cm²)

To investigate the optical behavior of the nanowires in the high power regime the frequency-doubled Ti-Sa laser (80 MHz repetition rate) is used for the excitation, where the energy per pulse can be estimated as $1 \text{ W/cm}^2 = 12.5 \text{ nJ/cm}^2/\text{pulse}$. Due to the combination of pulsed excitation with a bigger spot size ($\sim 9 \mu\text{m}$ diameter) reduced heating of the sample is expected. For this study, $2 \text{ mm} \times 2 \text{ mm}$ arrays of untapered wurtzite GaP nanowires with 200 nm diameter, $1.4 \mu\text{m}$ pitch, and lengths up to $13 \mu\text{m}$ are grown from EBL patterned substrate (Fig. 6.4).

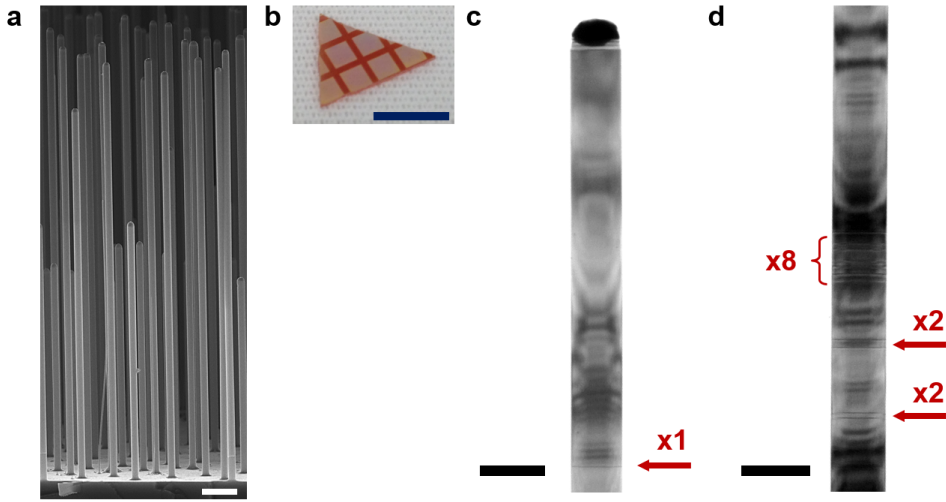


Figure 6.4: (a) SEM image of patterned GaP nanowires with 200 nm diameter (tilting-angle 80°). Scalebar: $1 \mu\text{m}$. (b) Optical image of the sample with $2 \text{ mm} \times 2 \text{ mm}$ patterned arrays of nanowires. Scalebar: 0.6 cm . (c-d) Bright-field TEM images acquired in two different positions along the nanowire showing the pure WZ phase, with few stacking faults indicated by arrows and numbers. Scalebars: 250 nm .

6.2.1 Power series

In Fig. 6.5a the PL spectrum collected at a low excitation power density of 0.03 W/cm^2 from as-grown WZ GaP wires is shown as the black curve. Significant reduction of the emission from deep impurity levels below 2.0 eV is achieved by using a larger size of the patterned area ($2 \text{ mm} \times 2 \text{ mm}$) respect to the small size e-beam arrays pattern. The difference between the two samples lies in the patterned area: the wires used in Fig. 6.2 are grown in arrays of $25 \mu\text{m} \times 25 \mu\text{m}$ in size, hence a small surface coverage compared to the bulk substrate (see Fig. 6.1). Instead, the wires used in Fig. 6.5a are grown in arrays of $2 \text{ mm} \times 2 \text{ mm}$, with a more homogenous coverage over the whole substrate which results in a reduction of incorporation of impurities from the substrate during growth. Similar optical results are obtained for 100 nm wires grown from the nanoimprint pattern.

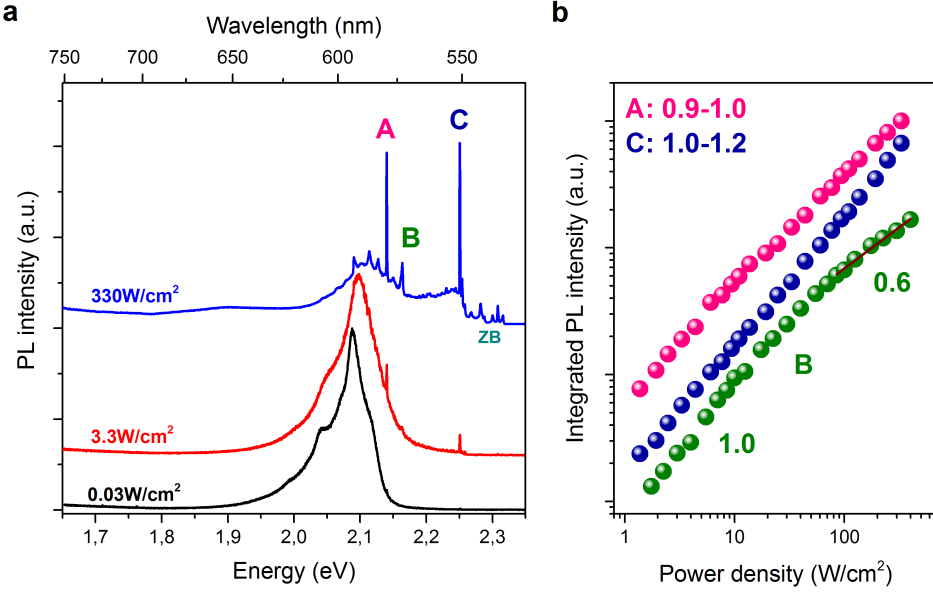


Figure 6.5: (a) Photoluminescence spectra of the WZ GaP wires acquired at different excitation powers. At the lowest excitation power the optical emission is centered at 2.088 eV, while the band filling up to 2.25 eV and the A-B-C exciton lines are observed at higher excitation powers. (b) Integrated PL intensity of the A-B-C lines as a function of the excitation power. All measurements are performed at 4K.

At the lowest excitation density, we observe a broad emission line located at 2.088 eV, which will be identified as a donor-acceptor pair (DAP) recombination^{56,103}. By increasing the excitation power up to 330 W/cm² (blue curve in Fig. 6.5a) we observe a relative saturation of the DAP recombination peak (see Fig. 6.8) and the rise of a continuum-like emission in the range 2.15-2.25 eV. The continuum emission strongly increases with both increasing excitation density and photon energy. However, a clear drop in the continuum emission is observed at 2.25 eV, which is also visible in the PL spectrum of a single nanowire (see Fig. 6.6b). At higher excitation density, we observe the appearance of three sharp emission lines at 2.140-2.164-2.252 eV, labelled as A-B-C. Across the tens of samples studied, the A-C lines are generally observed with similar intensities, while the B-line is only occasionally present. In the following interpretation, it will be shown that the A-, B-, and C-peaks are most probably related to the excitons of the A ($\Gamma_{9v} \rightarrow \Gamma_{8c}$), B ($\Gamma_{7v+} \rightarrow \Gamma_{8c}$), and C ($\Gamma_{7v-} \rightarrow \Gamma_{8c}$) band edges calculated with the DFT method^{31,45}.

The emission lines above 2.262 eV are related to the ZB substrate underneath the as-grown nanowires (see Fig. 6.6a)¹¹¹. The A-line at 2.140 eV shows a FWHM $\sim 220 \mu\text{eV}$. However, multiple peaks with a FWHM lower than 150 μeV (limited by the setup resolution limit) are visible when measured on a single wire over SiOx/Si substrate, as shown in Fig. 6.6b. Similarly, the B-line at 2.164 eV also shows multiple sharp peaks (see Appendix A.2) which are unresolved in our setup.

Instead, the C-line at 2.252 eV is observed as a single peak (FWHM ~ 260 μeV).

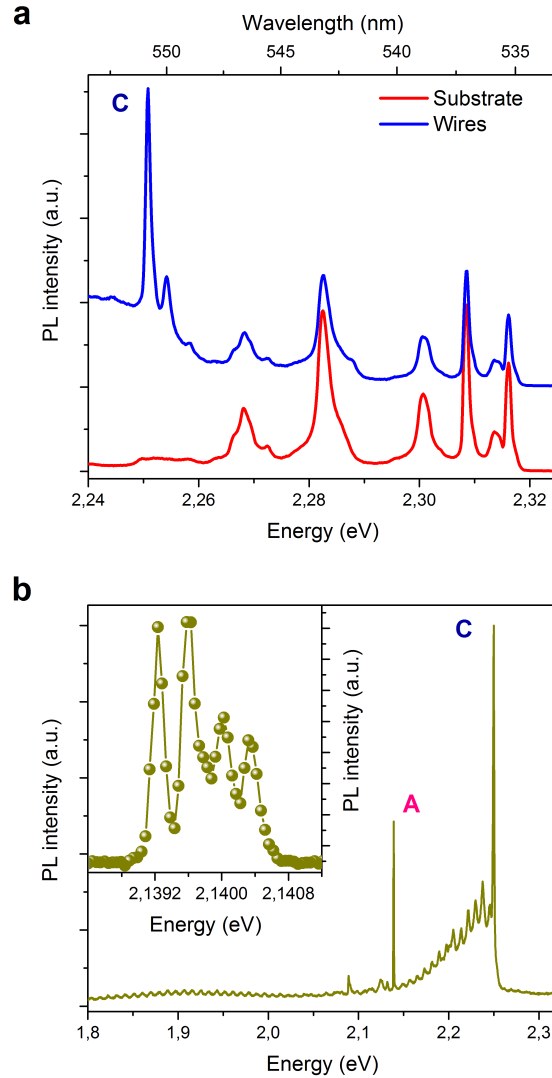


Figure 6.6: (a) Comparison of the PL spectra when measured on the as-grown nanowires and on the ZB substrate. (b) PL spectrum of a single wire transferred to SiO_x/Si substrate. Fabry-Pérot modes¹⁶ are visible across the entire emission spectra, and will be discussed in detail in chapter 7. Inset: enlarged view of the A-line in the range 2.1384-2.1412 eV. All measurements are performed at 4K.

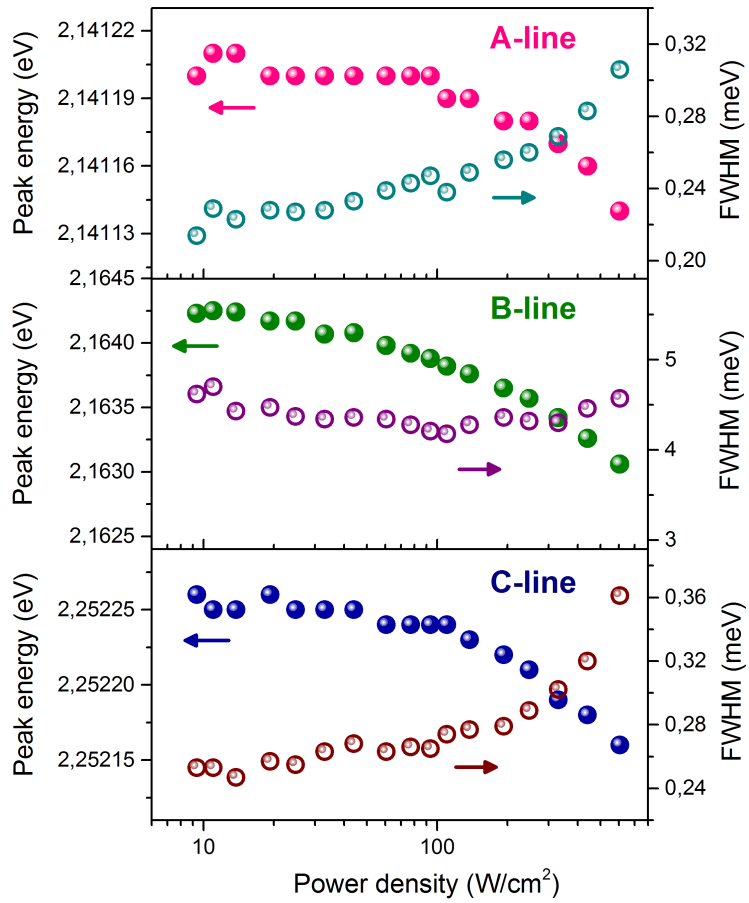


Figure 6.7: Peak energy and FWHM as a function of the excitation power for the A-, B-, and C-lines.

The integrated PL intensity (I_{PL}) as function of the excitation power density (P_{EXC}) is shown in Fig. 6.5b. The slope $K \sim 1$ extracted from fitting the data with the power law $I_{PL} \propto P_{EXC}^K$, together with the independence of the peak energy on the excitation power (see Fig. 6.7) suggest excitonic recombination for the A, B, and C peaks¹¹².

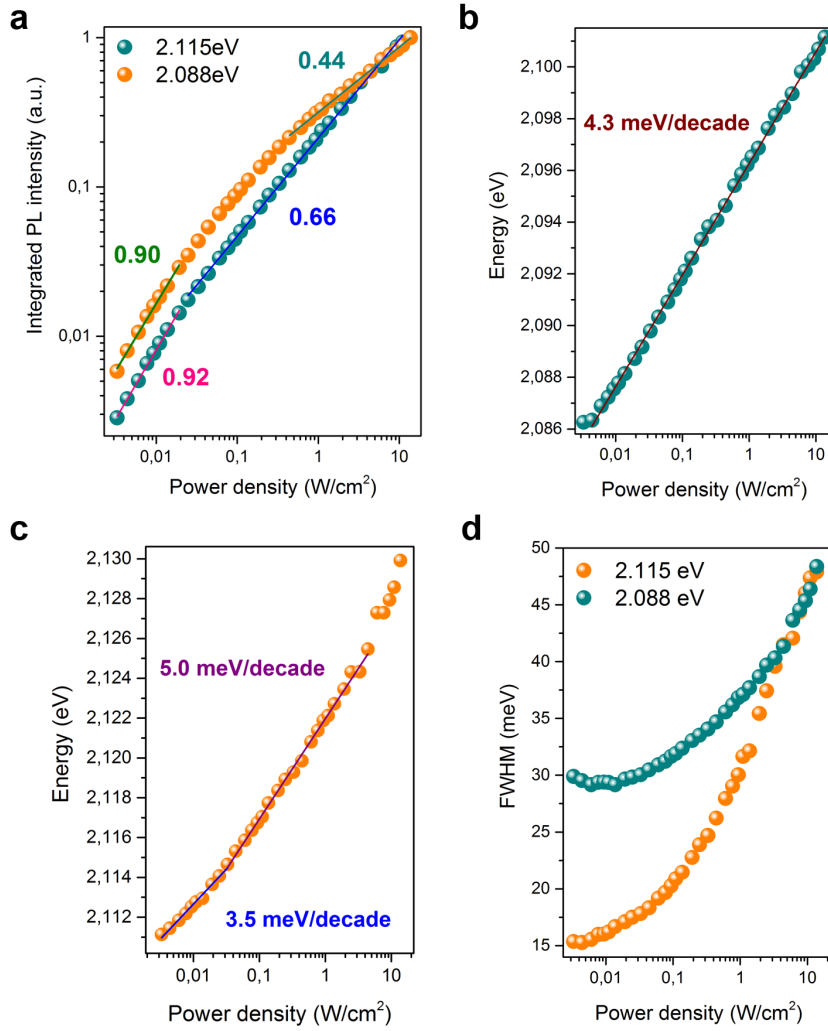


Figure 6.8: (a) Integrated PL intensity as a function of the excitation power for the 2.088 eV and 2.115 eV peaks. (b-c) Shift of the energy for the 2.088 eV (b) and 2.115 eV peaks (c) as a function of power. (d) Increase of the FWHM with excitation power.

6.2.2 Internal quantum efficiency and non-radiative efficiency

By fitting the power-dependent PL data using a rate equation model^{113,114}, we can estimate the internal quantum efficiency (IQE) and the non-radiative efficiency (NRE), defined as $NRE=1-IQE$. The Shockley-Read-Hall (SRH) non-radiative recombination^{115,116} and the Auger non-radiative recombination¹¹⁷ contribute to the NRE. The IQE and NRE as a function of excitation power density are shown in Fig. 6.9. More details on the fitting procedure are discussed in Appendix A.1. For excitation powers lower than 40 W/cm^2 , the total efficiency (IQE+NRE) is higher than 100% due to an overestimation of the NRE in presence of multiple recombination channels. Radiative recombination is the predominant mechanism in the A-line emission, with a small decrease of the IQE for increasing power. Instead, non-radiative recombination dominates for the B-line. The IQE of the forbidden C-transition, surprisingly increases up to 90% showing a predominantly radiative recombination mechanism. Across the samples studied, the maximum value of the IQE is in the range 40-90% for the A-line, 15-50% for the B-line and 70-90% for the C-line. Furthermore, Auger recombination¹¹⁷ can be excluded as a non-radiative source of recombination for the C-line (see Appendix A.1), in agreement with the time-resolved measurements that will be discussed in Fig. 6.11d. Using the same model to fit the DAP peak at 2.088 eV in the low excitation power regime, we obtain a radiative recombination efficiency close to zero, which indicates that the 2.088 eV emission peak is related to impurities incorporated in the nanowires (see Appendix A.1).

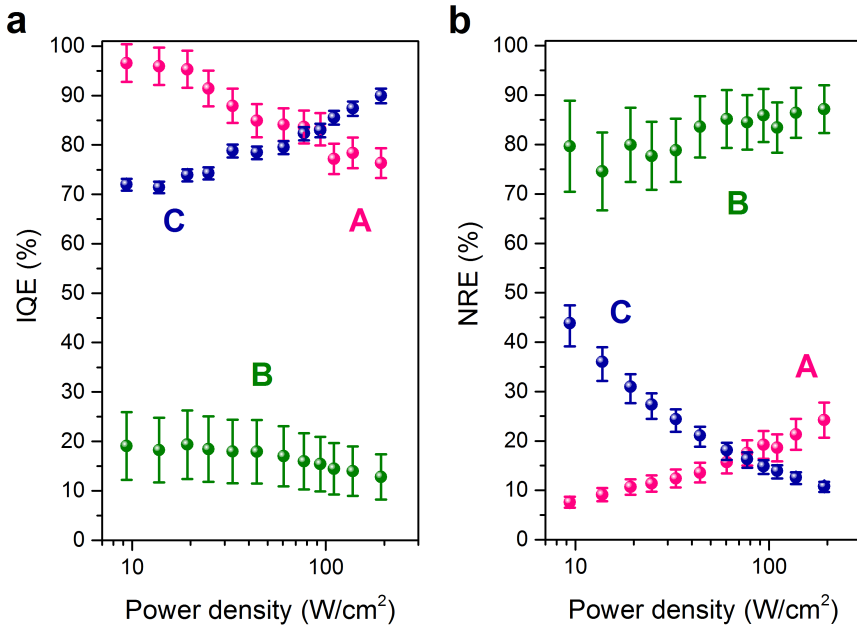


Figure 6.9: (a-b) Plot of the IQE (a) and NRE (b) as a function of the excitation power density for the A-B-C lines.

6.2.3 Phonon replicas

Additional narrow peaks are visible in the lower energy range of the A-line in Fig. 6.10a. Group theory predicts eight phonon normal modes at the Γ point: $2A_1$, $2E_1$, $2B_1$, $2E_2$ for the WZ structure (see Table 8 in chapter 2)^{52,105,106}, with one A_1 and one E_1 acoustic modes, while the remaining six modes are optical. Thus, the sharp peaks in Fig. 6.10a are assigned as acoustical and optical phonon replicas^{52,105,106} of 13 ± 1 meV (TA) and 48 ± 2 meV (TO/LO), respectively. Phonon replicas are often associated with the presence of localized states, such as bound excitons¹¹⁸. It is important to mention that we observe identical phonon replicas with the A- and B-lines (see Appendix A.2), but not with the C-line, indicating that the origin of the C-line is distinctly different to the nature of the A- and B-lines. Furthermore, the peaks at 1.996-2.041 eV in the black curve in Fig. 6.5a can be assigned as LO/TO (A_1 - E_1 - E_2) phonon replicas (46 ± 3 meV)⁵² of the main 2.088 eV peak.

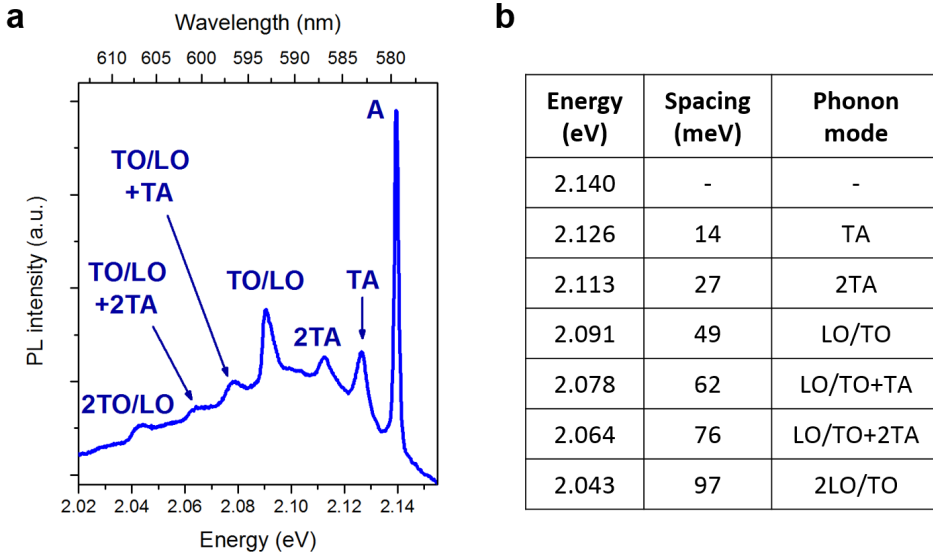


Figure 6.10: (a) Acoustical (TA) and optical (TO/LO) phonon replicas of the A-line. (b) List of the phonon modes observed in (a).

6.2.4 Lifetime of the exciton lines

Time-resolved PL measurements on the WZ GaP wires are presented in Fig. 6.11. A long lifetime of 75 ns for the A-line and a fast decay of ~ 0.7 ns for the band signal in the proximity of the A-line are shown in Fig. 6.11a. The highest resolution grating was used to select either the signal of the sharp peak or the band emission (2 meV off the peak). However, when selecting the A-line low intensity PL signal from the band underneath is still present, which results in a fast decay ~ 0.7 ns at the beginning of the red curve in Fig. 6.11a. Similar behaviour is observed for the B-line, with a long lifetime of 43 ns (see Fig. 6.11b). For the C-line, the

situation is completely different. We observe a short lifetime of 0.7 ns, which is measured at the edge of the continuum-like background signal with 0.5 ns decay, as shown in Fig. 6.11c. Furthermore, the lifetime of the C-line is almost independent on the excitation power (Fig. 6.11d) confirming that no Auger recombination is present¹¹⁷, as previously discussed in the IQE fit.

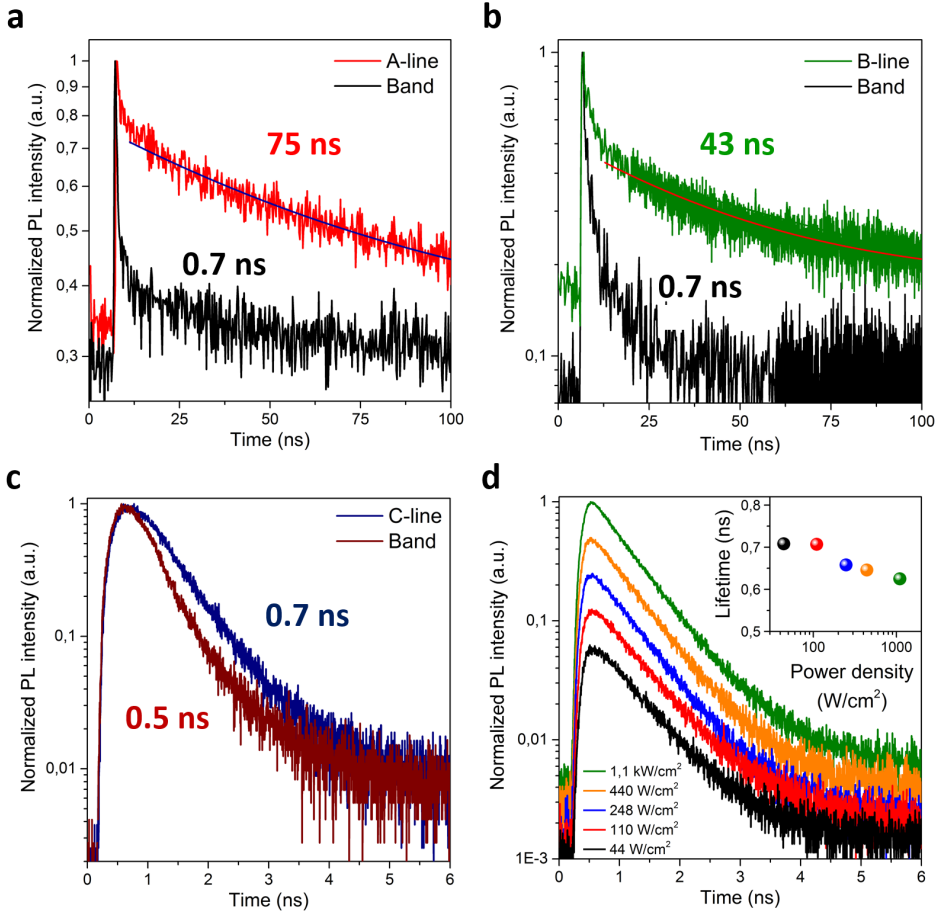


Figure 6.11: (a-c) Time-resolved PL measurements of the A-B-C lines compared with the short lifetime of the band signal. (d) Time-resolved PL spectra for the C-line collected at different excitation powers. Inset: lifetime values extracted from (d). All measurements are performed at 4K.

6.2.5 PL in polarization

Polarization-dependence PL measurements for the 2.088 eV peak and the C-line acquired on a single nanowire on SiOx substrate are shown in Fig. 6.12. Since the A-line consist of several peaks when measured on a single wire, with a FWHM at the setup resolution limit, the determination of the intensity is less accurate.

However, the A-line shows similar behaviour as the C-line for both excitation and detection polarization scans. Instead, the B-line was never observed in horizontal wires, hence no polarization measurements are available for this emission line. In the emission scan, preferred perpendicular polarization is observed for the 2.088 eV peak and for the C- line. In the excitation scan, the 405 nm laser is used as excitation source. The 2.088 eV peak does not have any preferred polarization, while the C- line shows preferred polarization parallel to the nanowire axis (c-axis).

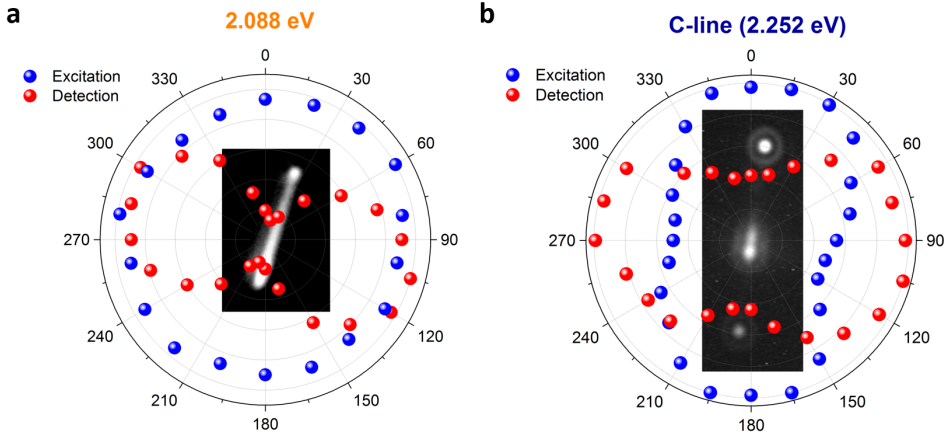


Figure 6.12: (a-b) Polarization dependence of the PL curves for the 2.088 eV (a) and 2.252 eV (b) peaks. The blue curve refers to the polarization excitation scan performed using the 405 nm laser, while the red curve is the scan of the polarization of the emission from the wires. All measurements are performed at 4K.

6.2.6 PL 3-100 K

In Fig. 6.13a-b the PL spectra and the integrated PL intensity of as-grown wires for temperatures ranging between 4 K and 100 K are shown. The ZB substrate emission disappear above 50 K due to the dissociation of the exciton bound to the nitrogen impurities^{29,106}. Reduced band filling and quenching of the C-line is observed in the WZ wires when the temperature of 100 K is reached, together with red-shift of the peak energy according to Varshni's law (inset in Fig. 6.13a)¹¹⁹. The data points in Fig. 6.13b are fitted according to Ref.¹²⁰ and an activation energy of ~ 30 meV is found for the A- and C-lines. The plot of the FWHM versus temperature is shown in the inset in Fig. 6.13b.

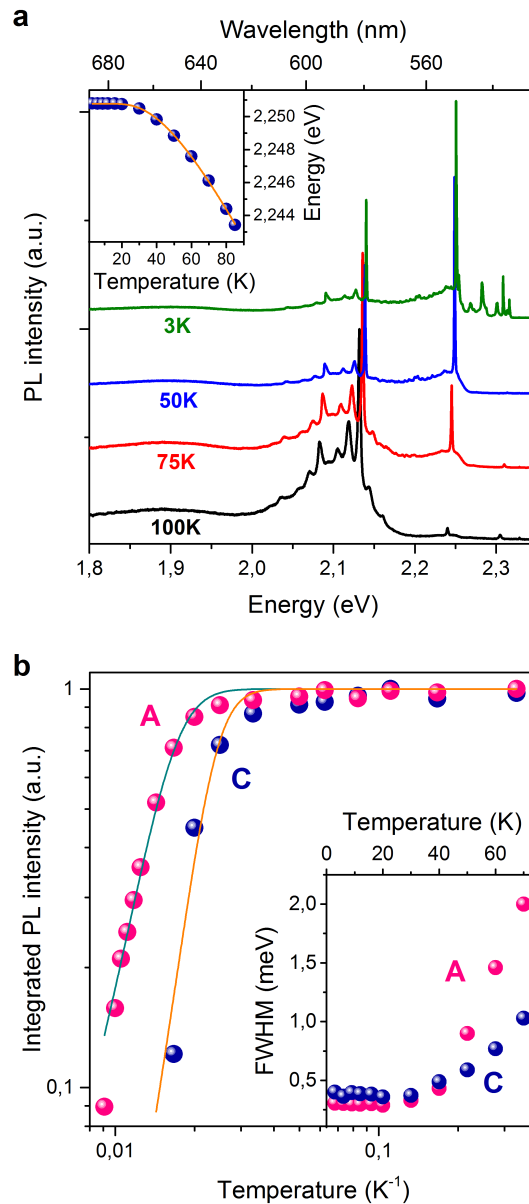


Figure 6.13: (a) PL spectra acquired in the range 3-100 K. Inset: plot of the energy of the C-line as a function of temperature. (b) Integrated PL intensity for the A-line and C-line versus $1/T$. Inset: plot of the FWHM as a function of the temperature for the A-line and C-line.

6.2.7 PLE measurements on vertical and horizontal wires

In order to get further insight into the band structure of WZ GaP low-temperature micro-photoluminescence excitation (PLE) spectroscopy is performed¹²¹. In all the PLE measurements the detection energy is set to 2.09 eV (dashed vertical pink line). The PL and PLE spectra for vertical and horizontal wires are shown in Fig. 6.14a (see Appendix A.3 for more details). Two sample configurations are studied: vertical nanowires (as-grown on the ZB GaP substrate) and horizontal ensemble of wires (transferred to a SiOx/Si substrate).

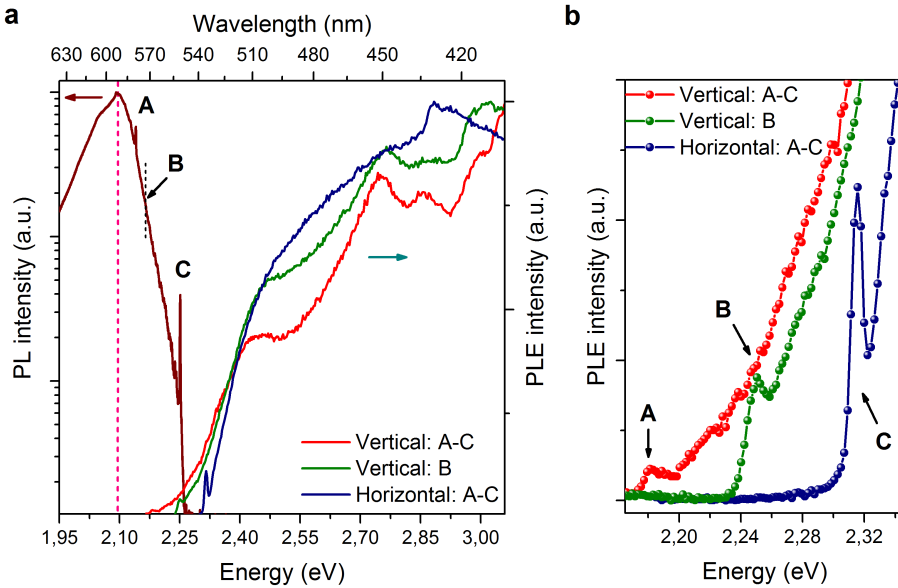


Figure 6.14: (a) PL spectrum acquired with the PLE excitation source at 405 nm - 5 W/cm² (dark red curve). The black dashed line indicates the peak energy of the B-line. The PLE curves are measured on vertical and horizontal nanowires. (b) Enlarged view of the PLE curves in (a). The first edge in the PLE spectrum (indicated by arrows) is strongly dependent on the corresponding PL intensity of the A-B-C lines. All measurements are performed at 4K.

In the vertical configuration, two different vertical arrays of wires are measured, one of them showing high intensities A-C lines, and the other one showing mainly the B-line in the high power PL spectrum (see Appendix A.2). Instead, the B-line was never observed in the PL spectra on horizontal wires, resulting in optical emission from the A-C peaks only in this configuration. The enlarged view of the PLE curves for vertical and horizontal wires in the energy range 2.16-2.34 eV is plotted in Fig. 6.14b, showing three well resolved band edges for the A-, B- and C-peaks. In the as-grown wires with high intensity A- and C-lines in PL, the first PLE peak is seen at 2.181 eV. However, in the case of predominant B-line in PL, the onset of the PLE shifts up to 2.250 eV. For vertically oriented wires, we observe a band-like continuum above the A-peak at 2.181 eV and above the B-peak at 2.250 eV. For horizontally oriented wires, we however observe a very low but clearly

non-negligible intensity signal between 2.05 eV and 2.311 eV (see Appendix A.3), followed by a sharp C-peak at 2.315 eV and a steep increase of the PLE intensity above the C-peak. The latter peak is observed in PLE for both horizontally and vertically oriented wires. When the temperature increases from 4 K to 50 K, the portion of the PLE signal below 2.31 eV reduces in intensity, while the C-peak becomes visible, as shown in Fig. 6.15.

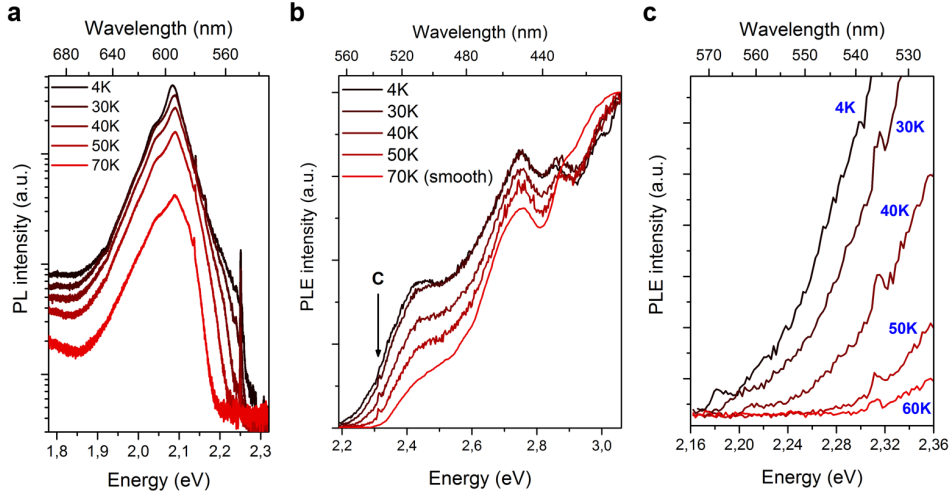


Figure 6.15: (a-b) PL spectra (a) and PLE spectra (b) measured in the temperature range 4-70 K for as-grown wires with high intensity A-C lines. (c) Enlarged view of the curves in (b).

Polarization dependence of the nanowire photoluminescence could be responsible for the differences the PLE spectra between vertically oriented and horizontally oriented wires¹²². However, polarization dependent PLE measurements on a horizontally oriented bundle of aligned nanowires (see Fig. 6.16) show no polarization-induced shift of the absorption edge below the C-peak. Thus, polarization anisotropy does not explain the observed difference between vertically and horizontally oriented wires in Fig 6.14b.

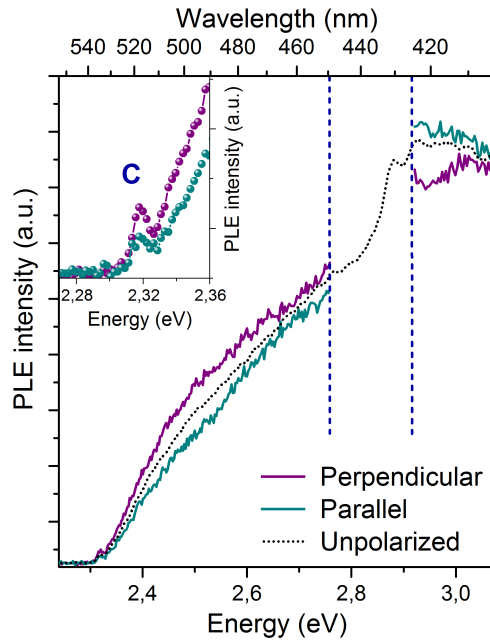


Figure 6.16: PLE curves acquired for polarization perpendicular (violet) and parallel (aqua) to the axis of a horizontally oriented bundle of aligned nanowires. In the range 2.755-2.910 eV the polarization of the excitation source is not suitable for measurements. The dashed curve is acquired using a de-polarizer in the excitation path. Inset: enlarged view of the PLE spectra showing the C-edge. All measurements are performed at 4K.

6.3 Interpretation of the experimental results

6.3.1 Donor acceptor pair recombination

The broad emission line located at 2.088 eV shows many features which are characteristic of a DAP recombination^{56,103}. First, the emission line is asymmetrically broadened with a FWHM of ~ 30 meV, with the presence of LO/TO phonon replicas¹²³. In addition, the power-dependence for the 2.088 eV peak in Fig. 6.8 shows a strong blue shift with increasing excitation power due to Coulomb interactions between charged donors and acceptors^{56,103}. Furthermore, the saturation of the PL intensity at high excitation power and the values of the parameters extracted from the IQE fit (see Appendix A.1) indicate recombination from impurity states¹¹². These arguments provide compelling evidence that the peak at 2.088 eV can be assigned as DAP recombination. The high energy shoulder peak at 2.115 eV, is most probably related to an electron to acceptor ($e-A^0$) recombination line. The binding energy of the shallow acceptors in ZB GaP is in the range 20-60 meV³³. In the assumption that similar binding energies also hold for WZ GaP, from the position of the ($e-A^0$) line we can estimate the fundamental band gap of WZ GaP being in between 2.135 eV and 2.165 eV. Additionally, the separation between the ($e-A^0$) and the DAP emission peaks indicates a donor binding energy of less than 27 meV. It is known that nitrogen can induce direct transitions in GaP^{124,125}. Since we can exclude any possible source of atomic nitrogen in our reactor we can rule out nitrogen related direct emission from the nanowires. Furthermore, the emission bands at energies lower than 1.9 eV, which are especially visible in Fig. 6.2, are related to deep levels associated with incorporated impurities⁵⁴.

6.3.2 Burstein-Moss bandfilling

The plot of the predicted matrix element in chapter 2 (Fig. 4) shows a very small value for the matrix elements for the $\Gamma_{9v} \rightarrow \Gamma_{8c}$ transition and zero matrix element for the $\Gamma_{7v+} \rightarrow \Gamma_{8c}$ transition⁴⁵. Due to the very low radiative recombination probability of the photo-excited carriers in the Γ_{9v-} and Γ_{7v+} -bands, an enhancement in the band-filling is expected. As a result of this, the continuum-like emission between 2.15-2.25 eV strongly increases with increasing excitation power, as seen in Fig. 6.5a. The observed excitation power dependence strongly points towards a band-filling continuum due to the Burstein-Moss effect^{47,56,104}. The increasing magnitude of the continuum emission at higher photon energy is in accordance with the increasing value of the matrix elements with increasing k-values shown in chapter 2 (Fig. 4). The steep cut-off of the continuum-like emission near the C-line suggests a fast recombination channel, which is strongly limiting the band-filling above it. This is indeed shown by the fast radiative lifetime (0.7 ns) of the C-line. Since band-filling can only be observed above the fundamental band gap, this fact, combined with the acceptor nature of the 2.115 eV peak, indicates that the fundamental band gap of WZ GaP is located above the A-line, around 2.15 eV.

6.3.3 Bound exciton character of the A- and B-lines

Bound excitons rather than free excitons are usually predominant in large band gap semiconductors^{126–128}. By their nature, bound excitons are localized particles in real space. This enhances the delocalization of the electron wave function in the k-space, allowing an overlap with the larger transition matrix elements at larger k-values, outside the Γ -point. This results in a non-zero transition strength for bound excitons, thus providing a radiative recombination channel for the Γ_{9v} - and Γ_{7v+} -bands, which would otherwise not emit any photoluminescence with the Γ_{8c} -band. As it will be discussed later, the A- and B-lines are the bound exciton emissions of the A ($\Gamma_{9v}\rightarrow\Gamma_{8c}$) and B ($\Gamma_{7v+}\rightarrow\Gamma_{8c}$) transitions, respectively. The measured 75 ns and 43 ns recombination lifetimes for the A- and B-lines confirm this hypothesis. Furthermore, the localization of bound excitons in real space also enhances the phonon replicas¹¹⁸, as shown in Fig. 6.10a. By reversing these arguments, the observation of the phonon replicas of the A- and B-line provides additional evidence for the bound exciton character. In addition, the temperature dependence for the FWHM of the PL shows linear scaling with temperature, which is typical for a bound exciton emission (see Fig. 6.13)^{123,129}. Using the Haynes's rule, which relates the bound exciton binding energy to the donor/acceptor binding energy¹³⁰, the position of the A- and B-bound excitons are expected to be located 5-10 meV below the band edge for the $\Gamma_{9v}\rightarrow\Gamma_{8c}$ and $\Gamma_{7v+}\rightarrow\Gamma_{8c}$ transitions. Hence, from the energy values of the bound excitons we estimate the fundamental band gap of WZ GaP above 2.15 eV, in agreement with the assignment based on the DAP emission. We also note that the 24 meV splitting between the A and B-line is too large to attribute both peaks to the same band edge. As a next confirmation that the A- and B-lines are bound excitons, we note that the A-line at 2.140 eV consists of multiple bound exciton peaks with a FWHM lower than 150 μeV , as shown in Fig. 6.6c. Since an exciton can bind to both neutral and charged donors and acceptors, multiple emission lines are expected¹²⁹. The detailed identification of the bound exciton lines is however beyond the scope of the present thesis. Similar arguments holds for the multiple bound exciton nature of the B-line. Instead, the C-line at 2.252 eV is always observed as a single peak with a FWHM of $\sim 260 \mu\text{eV}$, suggesting a free exciton recombination mechanism, as it will be discussed later in the chapter.

6.3.4 Direct band gap excitonic character of the A-, B-, and C-lines

The integrated PL intensity (I_{PL}) as function of the excitation power density (P_{EXC}) in Fig. 6.5b shows the linear behaviour typical of the direct band gap excitonic recombination¹¹² for the A-, B-, and C-peaks. The slope $K\sim 1$ extracted from fitting the data with the power law, $I_{PL}\propto P_{EXC}^K$, together with the independence of the peak energy position on excitation power (see Fig. 6.7) indicate direct band gap excitonic recombination for the A- and C-lines^{56,112}. A similar behaviour is observed for the B-line, although its slope is reduced above 85 W/cm^2 , which might be attributed to interaction with the continuum or by filling of impurity states^{56,128}. We occasionally also observe sharp PL emission from confined states

associated with stacking faults within the nanowires, showing narrow quantum dot (QD) related peaks³⁴ in between the A-line and the C-line. However, the sharp A- and C-lines are always observed at exactly the same photon energy, for all samples studied. In addition, QD-related emission peaks show a clear saturation with excitation power, while the A- and C-peaks show a linear excitation power dependence at similar excitation densities, which allows to clearly distinguish between QD-related emission near stacking faults and the excitonic A- and C-peaks¹³¹.

6.3.5 High internal quantum efficiency of the A- and C-lines

The plot of the IQE as a function of the excitation power in Fig. 6.9 shows that radiative recombination is the predominant mechanism for both the A-line and the C-line. Instead, the B-line seems to be dominated by non-radiative recombination or an interaction with the band filling continuum. From the fit of the power dependent PL data, Auger recombination¹¹⁷ can be excluded as a non-radiative recombination mechanism for the C-line (see Appendix A.1). Another argument against Auger recombination is that the radiative lifetime of the C-line is independent on the excitation power (see Fig. 6.11d). The high IQE values measured for both the A- and C-lines provide evidence that the A- and C-excitons are related to direct band gap transitions with a large oscillator strength, although the A-transition was theoretically predicted to be very weak and the C-transitions was predicted to be completely forbidden⁴⁵. For the A-line, the high IQE is possibly related to the large k-space delocalization of the bound exciton. We can only speculate on the relatively small IQE of the B-line. This transition is predicted to be completely forbidden, however we speculate that the B-line is only visible when the bound exciton is localized close to a local symmetry-breaking feature, such as a nearby surface or stacking fault, or due to a nearby second impurity. This explanation also explains the fact the B-line is only occasionally visible. The origin for the high IQE value for the C-line is discussed in the next section.

6.3.6 Free exciton nature of the C-line

We now turn our attention to the C-line at 2.252 eV. This emission line is experimentally observed as a single peak (FWHM ~ 260 μeV) with no phonon replicas. The combination of the short radiative lifetime of 0.7 ns with the very high IQE value strongly suggests an allowed direct band gap transition. The linear scaling of the C-line with the excitation power, together with the independence of the peak energy on the excitation power indicate a direct band gap free exciton recombination¹¹². This assignment is further confirmed by the fact that a zero diamagnetic shift is observed in the presence of a magnetic field (not shown). By looking at the spectral position of the C-line we address this emission to the C band edge ($\Gamma_{7v} \rightarrow \Gamma_{8c}$), which is however predicted to be dipole forbidden by the selection rules. As opposed to the A- and B-lines, the C-line shows a clear absorption edge in PLE with an excitonic-like enhancement at 2.315 eV, which indicates an exciton binding energy $E_b = 13 \pm 2$ meV (see Fig. 6.17). We speculate that the C-line is either due to an allowed 2p-exciton, or due to the mixing of the C-band with the A- and B-bands, resulting in a larger oscillator strength at the band edge of the C-

band. Theoretically, since the C transition is dipole forbidden, the 1s exciton state is not allowed⁴⁸. However, a 2p free exciton could reverse the parity, resulting in an allowed transition with a large oscillator strength^{38,48}. The second option is that the oscillator strength of the 1s exciton is enhanced by band mixing with the A- and B- bands. As shown in chapter 2 (Fig. 4), at large k-values (i.e. higher energy values in the band-filling continuum) large matrix elements are predicted for the A- and B-bands and the overlap with the C-band becomes possible. The measured 0.5 ns lifetime for the band-filling continuum near the C-line in Fig. 6.11c supports this idea. At present stage, we are not yet able to provide final conclusion on the nature and the large oscillator strength of the C-line. However, we like to comment that in case that the C-line is a p-type free exciton, similar p-type free excitons would be expected for the A- and B-band edges as well, which are not observed. On the other hand, only the C-line is overlapping with a band-filling continuum with a 0.5 ns radiative lifetime, which favors the band mixing argument. Finally, the PL spectra in Fig. 6.6a shows the C-line together with a peak located 3.6 meV higher in energy. The former energy spacing could result from the separation between different excited states for the C-exciton¹³², as calculated in chapter 2.

6.3.7 Assignment of the A-, B-, and C-peaks

Combining the initial estimate for the position of the fundamental band gap of WZ GaP based on the position of the (e-A⁰) line, the A- and B-bound excitons, and the position of the band-filling continuum, with the theoretically calculated band gap positions, we can assign the A-, B-, and C-peaks. We assign the A- and B-peaks at 2.140 eV and 2.164 eV as bound exciton recombination¹¹² of the A ($\Gamma_{9v} \rightarrow \Gamma_{8c}$) and B ($\Gamma_{7v+} \rightarrow \Gamma_{8c}$) transitions^{31,45}, respectively. Furthermore, by looking at the spectral position of the C-peak at 2.252 eV we speculate that this emission, which has no phonon replicas and a short lifetime of 0.7 ns, is the free exciton¹¹² related to the C ($\Gamma_{7v-} \rightarrow \Gamma_{8c}$) transition^{31,45}. Our assignment is supported by the PLE measurements presented in Fig. 6.14. No phonon modes are observed for the WZ GaP wires, unlike in the PLE spectra of the indirect band gap semiconductor like ZB GaP¹⁰⁶. This suggests that the WZ GaP emission originates from the (dipole forbidden) direct band gap transition predicted by the DFT theory^{31,45}. For vertically oriented nanowires, the PLE signal is observed above 2.17 eV, further indicating that the fundamental direct band gap is slightly above the A-line, in agreement with the assignment provided from the PL measurements. Furthermore, the PLE spectra in Fig. 6.14b show the presence of three distinct and well-resolved absorption edges, each featuring an excitonic-like enhancement close to its respective direct band gap^{121,133}.

6.3.8 Discussion of the PLE spectra

The PLE spectra can be fitted using the parabolic band approximation $I_{PLE} \propto (E - E_0)^P * I_{EXC}$ ^{47,69,134}, as shown in Fig. 6.17. The exponent $P_{VER}=1.8$ for the vertically oriented wires (in the range 2.195-2.325 eV) could result either from a forbidden direct transition or from an indirect transition¹³⁴. The indication of a

forbidden direct transition agrees with the wave-vector dependence of the transition matrix elements of the A-transition in chapter 2 (Fig. 4), where a strong oscillator strength is observed only at large k-vector values. For the horizontally oriented wires, the exponent is found to be $P_{HOR}=0.70\pm 0.02$ (in the range 2.32-2.48 eV), which is close to the value of 0.5 predicted for a direct allowed transition¹³⁴. This confirms the high oscillator strength derived from the lifetime measurements of the C-line in Fig. 6.11c.

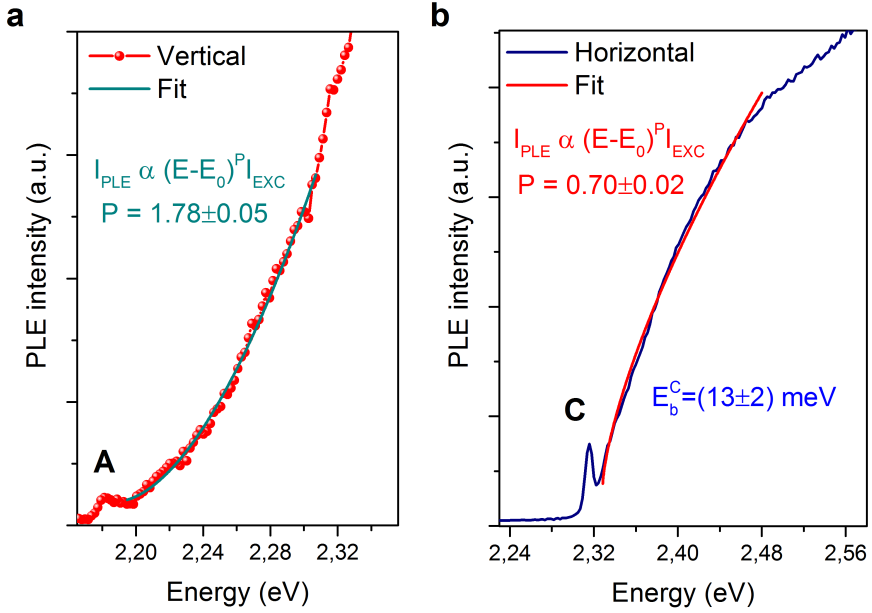


Figure 6.17: (a-b) Fit of the PLE curves for vertical (a) and horizontal (b) wires using the parabolic band approximation^{47,69,134}.

The exciton binding energy (E_b) can be extracted from the PLE curve according to $E_b = E_{PEAK} - E_0$, where E_{PEAK} is the energy of the exciton peak and E_0 the band edge energy value extracted from the previous fit. An estimation of the E_b for the A-B peaks is not possible due to the parabolic behaviour of the PLE signal, while an exciton binding energy of 13 ± 2 meV is found for the C-peak.

6.3.9 Stokes shift

The values for the peaks observed in PL and PLE are listed in Tab. 6.1, together with the predicted band structure values from the DFT calculations^{31,45}. In addition, the observed Stokes shifts between PL and PLE¹³⁵ are listed in Tab. 6.1. In the conventional model, the Stokes shift is related to inhomogeneities, e.g. due to interface fluctuations in a quantum well¹³⁵ or due to a landscape of charged impurities in a bulk semiconductor¹³⁶. In such a model, the Stokes shift is directly related to the inhomogeneous linewidth of an excitonic transition. Due to the combination of narrow PL-linewidths and high crystalline purity of the wires,

disorder can be excluded as a source of the observed Stokes shifts¹³⁵. Thus, the exceptionally large Stokes shift in WZ GaP cannot be explained by the narrow FWHM of the PL-PLE peaks.

We speculate that the predominant factor to explain the experimental PLE data is the wave-vector dependence of the transition matrix elements of the A-, B-, C-bands as given in chapter 2 (Fig. 4). Very weak PLE signal is expected close to the band edges, where the transition matrix elements are very small, while the PLE intensity increases above the fundamental band edge, which translates into an apparent Stokes shift. We first comment that the apparent Stokes shift increases from the 41 meV of the weakly allowed (by selection rules) A-band up to 86 meV of the completely forbidden B-band. Next, the apparent Stokes shift reduces to 63 meV for the forbidden C-band. Although the detailed interpretation of the PLE-spectrum, and in particular interpretation of the observed Stokes shifts between the PL- and PLE-spectra is very challenging, the general shape of the PLE data supports the former assignment of the A-, B- and C-lines.

Γ_{8c}	A (eV)	B (eV)	C (eV)	Δ_{AB} (meV)	Δ_{BC} (meV)
PL	2.140	2.164	2.252	24	88
PLE _{VERT}	2.181	2.250	2.315	69	65
PLE _{HOR}	-	-	2.315	-	-
ΔE_{PL-PLE}	0.041	0.086	0.063	-	-
DFT	2.123	2.165	2.340	42.5	132.5

Table 6.1: Table of the measured values for the A, B, and C transitions in PL and in PLE compared with the DFT calculations in Ref.^{31,45}.

6.3.10 Transitions with the Γ_{7c} conduction bands

We finally note that the energy bands seen in PLE above 2.4 eV are possibly related to transitions with the M-band, while the peaks between 2.7 and 3.0 eV are related to the Γ_{7c} to valence band transitions. In the PLE spectra of vertical wires, the bump at 2.420 eV could indicate an optical transition between the Γ_{9v} band and the M-minimum in the conduction band. This peak is also measured when the wires are transferred into PDMS¹⁰⁸. However, since no phonon modes are observed, no clear interpretation can be given for this peak. The PLE curve of the horizontal wires for energies above 2.420 eV increases in intensity until a second edge at 2.865 eV is observed. Optical transitions with the Γ_{7c} band are expected above 2.88 eV³¹ in agreement with the PLE data. Higher energy bands are also seen in the vertical wires at 2.74 eV, 2.85 eV and 2.97 eV, possibly related to the Γ_{9v} , Γ_{7v+} , and Γ_{7v-} band transitions with the Γ_{7c} band.

6.3.11 Polarization dependence in PL-PLE

In the polarization-resolved PLE measurements in Fig. 6.16 preferred perpendicular polarization is seen for the C-peak at 2.315 eV. This behaviour seems to

contradict the observed parallel polarization in the 405 nm (3.06 eV) excitation-polarization scan of the C-line in Fig. 6.12b. As mentioned in the PLE measurements, transitions with the Γ_{7c} conduction band are observed above 2.7 eV. Thus, the discrepancy between the 405 nm excitation in Fig. 6.12b and the polarization of the PLE spectrum for the C-line results from the different selection rules of the Γ_{8c} and Γ_{7c} conduction bands. In fact, when we measure the polarization dependence at 405 nm we are exciting Γ_{7c} states, which are expected to have parallel polarization, which is in agreement with the measurements.

6.4 Conclusion

We performed a detailed study on the optical properties of WZ GaP by performing PL, time-resolved PL, and PLE measurements. The high emission intensity, the striking difference in the WZ-ZB lifetimes, and the very good agreement between the experimental and predicted WZ GaP band gap values, strongly suggest the presence of direct band gap transitions in the WZ GaP nanowires. We could clearly assign a donor-acceptor pair (DAP) recombination peak at 2.088 eV, and a Burstein-Moss band-filling continuum between 2.15 and 2.25 eV. Moreover, the sharp A- and B-lines could be clearly identified as bound excitons, with both TA and LO/TO phonon sidebands. The sharp A, and C-lines exhibit a linear power dependence and a very high internal quantum efficiency, pointing towards direct band gap excitonic transitions. The occasionally visible B-line has a lower IQE transition and shows a deviation from the linear power dependence. The C-line shows a fast recombination lifetime of 0.7 ns, and has the character of a free exciton. We provide experimental indication of the A-, B-peaks as bound excitons of the A- ($\Gamma_{9v} \rightarrow \Gamma_{8c}$) and B- ($\Gamma_{7v+} \rightarrow \Gamma_{8c}$) band edges, while the C-peak is speculated to be the C- ($\Gamma_{7v-} \rightarrow \Gamma_{8c}$) free exciton, which might be either the 2p-exciton or it acquires its oscillator strength by band mixing. The high IQE value of excitonic C-transition finally provides applications for the solid state lighting in the green range of the visible wavelengths⁷¹.

Chapter 7

Determination of the dielectric constant

In this chapter, we show the excellent waveguiding properties of the WZ GaP wires capped with a $\text{Al}_{0.4}\text{Ga}_{0.6}\text{P}$ shell. The Fabry-Pérot resonances observed in the PL spectrum of single wires are used to estimate the value for the dielectric constant of WZ GaP at 550 nm of $\epsilon = 15 \pm 1$.

7.1 Fabry-Pérot modes

The SEM image in Fig. 7.1a shows one GaP/ $\text{Al}_{0.4}\text{Ga}_{0.6}\text{P}$ core/shell nanowire of ~ 220 nm diameter and $18.5 \mu\text{m}$ length transferred on SiOx. When the wire is excited with the 405 nm laser with a rectangular spot of around $1 \mu\text{m} \times 10 \mu\text{m}$, the PL image in Fig. 7.1b is obtained. Two bright emission spots are visible at the ends of the nanowire, indicating that the GaP wire act as an efficient waveguide^{16,137}.

High modulations due to the Fabry-Pérot (FP) interferences as a result of the multiple reflections between the wires end facets⁹⁹ are seen in the PL spectra of the three nanowires shown in Fig. 7.2a. The modes spacing $\Delta\lambda$ reduces for increasing wire length and increases with the emission wavelength, as shown in Fig. 7.2b. In the former figure, the data points from a set of 11 nanowires with different lengths are shown.

The mode spacing in a Fabry-Pérot cavity is given by¹³⁸:

$$\Delta\lambda = \frac{1}{L} \left(\frac{\lambda^2}{2n_g} \right), \quad (7.1)$$

where L is the nanowire length and n_g is the group index defined as:

$$n_g = n_e - \lambda \frac{dn_e}{d\lambda}, \quad (7.2)$$

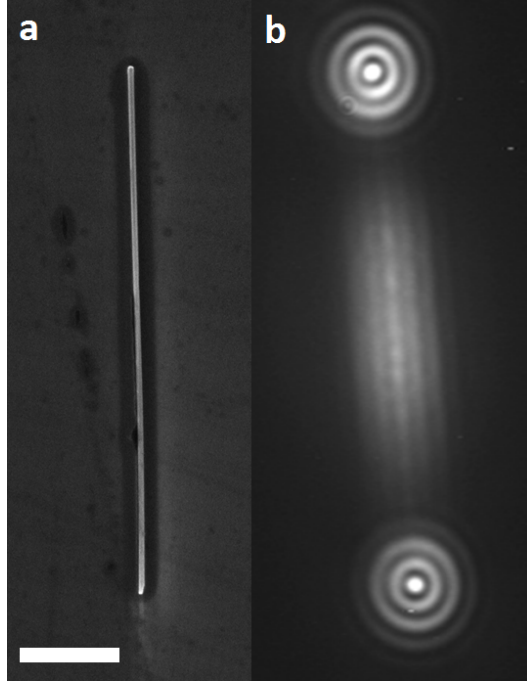


Figure 7.1: (a) SEM image of a GaP/Al_{0.4}Ga_{0.6}P core/shell nanowire of ~ 220 nm diameter and $18.5 \mu\text{m}$ length transferred on SiOx. The gold droplet is visible in the top end facet of the wire. Scalebar: $2 \mu\text{m}$. (b) PL image at 4 K of the wire when excited with the 405 nm laser with a rectangular spot of around $1 \mu\text{m} \times 10 \mu\text{m}$.

and n_e is the refractive index. Thus, for a fixed wavelength the mode spacing $\Delta\lambda$ is expected to scale proportional to $1/L$, as confirmed in Fig. 7.3.

7.2 Finesse and end facets reflectivity

The performance of a Fabry-Pérot resonator is characterized by the finesse F , defined as¹³⁹:

$$F = \frac{\Delta\lambda}{w}, \quad (7.3)$$

where w is the FWHM of the FP modes. The finesse can be viewed as the number of beams interfering within the FP cavity to form a standing wave. Higher finesse means higher number of interfering beams within the cavity, hence a more complete interference process. In Fig. 7.4 the measured values of the finesse for three different nanowires are shown. Constant values of the finesse above 600 nm are found in all the wires studied, while an enhancement in the finesse around 580 nm is occasionally observed. Variation in the refractive index is commonly observed close to the direct band gap of the III-V semiconductors¹⁴⁰. Thus, the

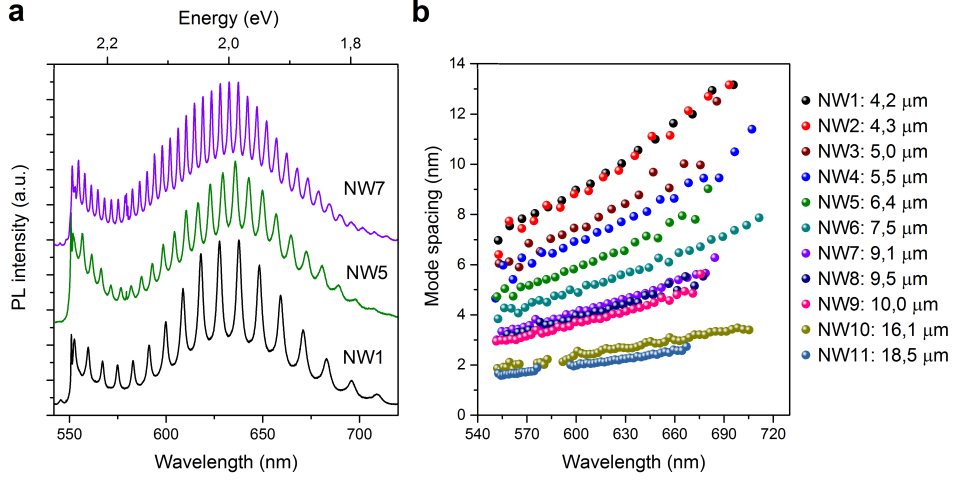


Figure 7.2: (a) PL spectra acquired at 4K of three nanowires with different lengths showing a change in the FP modes spacing. (b) Plot of the modes spacing as a function of the emission wavelength for 11 nanowires with different lengths.

resonance observed in the finesse at 580 nm is a further indication that the band gap of WZ GaP is at around 2.15 eV, as discussed in chapter 6.

One of the major factors which affects the finesse is the reflectivity R of the wire end facets, which can be estimated from the following formula¹⁴⁰:

$$F = \frac{4R}{(1 - R)^2}. \quad (7.4)$$

In the set of wires studied, the reflectivity at 580 nm is in the range 0.15-0.40, while at 650 nm the maximum in the reflectivity decreases to 0.28. Two main factors contribute to this behavior: imperfections in the wire end facet and losses. During the transferring of the nanowires over the SiO_x substrate one side of the wires breaks, resulting in one end facet with the gold droplet, while the other facet can either have a perfect flat edge surface or a more rough one. This can lead to additional losses, which affects the reflectivity, hence the finesse of the FP cavity. Thus, the spread in the finesse for different wires is related to the behavior of the end facet. In addition, due to the different morphology of the two end facets of the wire, the reflectivity R estimated from Eq. 7.4 can be slightly different from the reflectivity of the single end facets R_1 and R_2 .

7. Determination of the dielectric constant

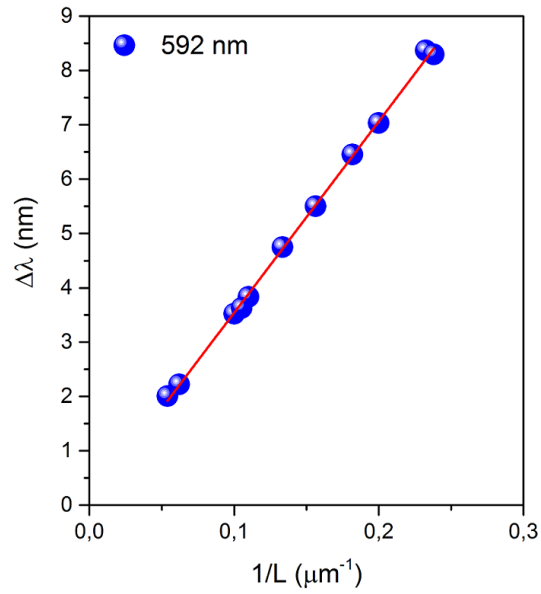


Figure 7.3: Plot of the FP modes spacing as a function of $1/L$.

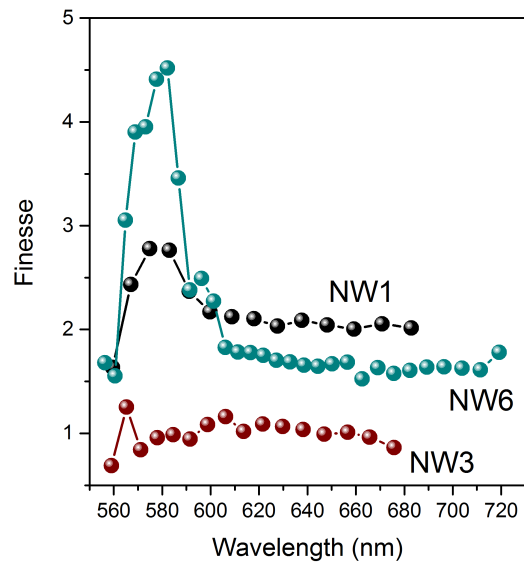


Figure 7.4: Plot of the finesse for three different nanowires.

7.3 Refractive index

The mode spacing in the Fabry-Pérot cavity of the wire can provide information on the refractive index n_e of the WZ GaP (Eq. 7.1-7.2), if the dispersion relation for n_e is known. The Sellmeier equation^{16,141} can be used to give an approximate dispersion relation for n_e :

$$n_e^2 = A + B \frac{\lambda^2}{\lambda^2 - C}, \quad (7.5)$$

where A, B and C are the Sellmeier coefficients. By fitting the mode spacing $\Delta\lambda$ as a function of the wavelength λ using the Eq. 7.1-7.5 we can estimate the refractive index n_e for the WZ GaP wires. In Fig. 7.5 the values for n_e of the WZ GaP wires as a function of the wavelength are shown, together with the refractive index for the ZB GaP bulk (red dashed line). The error bars are derived from the fit on the set of wires studied. Higher value of the refractive index n_e for the WZ wires respect to the ZB bulk is found.

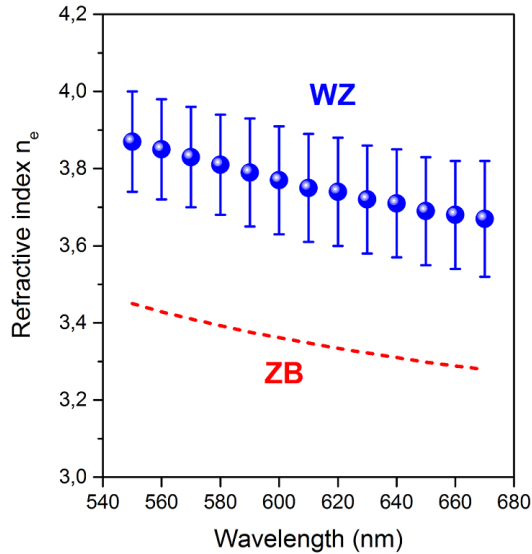


Figure 7.5: Plot of the refractive index n_e for the WZ GaP wires as a function of wavelength. The red dashed line indicates the refractive index of ZB GaP.

The measured value for the refractive index of the WZ wires is only a lower limit compared to the WZ bulk value, due to two reasons:

1. $\text{Al}_{0.4}\text{Ga}_{0.6}\text{P}$ shell: the higher band gap shell has a lower refractive index ($n_e=3.24$ for ZB $\text{Al}_{0.4}\text{Ga}_{0.6}\text{P}$ ¹⁴²), which can reduce the measured value for the refractive index of the wires.
2. Dielectric mismatch with air¹⁴³: the guided modes in the wires are not fully confined inside the nanowire, but also extend to the surrounding air.

Depending on the guided modes (TE, TM, HE, ...) present in the wire the mode index (measured refractive index) changes. However, the mode index is always lower than the refractive index of the bulk material¹⁴⁴. Hence, the measured difference in the refractive index between the WZ phase and the ZB phase can only increase by considering higher order guided modes. The calculation of the FP mode profile in the wire should take into account the dielectric mismatch, which has the effect of lowering the measured value of the refractive index. However, this method is outside the scope of this thesis.

Due to the dielectric mismatch, the n_e measured for the WZ wires is an effective refractive index. In case that similar optical measurements would be performed on ZB wires, the measured value for n_e would be lower than the ZB bulk value, resulting in a even bigger difference between the refractive indexes of the WZ and ZB crystal phases. The effect of the dielectric mismatch could be estimated by measuring the FP modes as function of the WZ GaP wire diameter. Since the confinement of the optical modes increases with increasing wire diameter, for very large diameters (such as >500 nm) we'd expect an asymptote behavior, approaching the WZ GaP bulk refractive index.

7.4 Dielectric constant

At the optical frequencies, the dielectric constant ϵ can be related to the refractive index n_e using the following relation¹⁴⁰:

$$n_e = \sqrt{\epsilon}, \quad (7.6)$$

The measured value (averaged over the set of 11 wires) of the dielectric constant ϵ for the WZ GaP wires at 550 nm is 15 ± 1 . The dielectric constant for the ZB phase at 550 nm is 11.9. As discussed in the previous section, the measured value of ϵ is only a lower limit compared to the bulk WZ GaP. In literature there are only two studies that determine the dielectric constant for both the WZ and ZB phases. In bulk GaN a higher dielectric constant is found in the ZB structure respect to the WZ¹⁴⁵, while InAs nanowire arrays show the opposite trend in the visible range¹⁴⁶. Thus, additional studies on other III-V semiconductors like GaAs and InP are needed to draw general conclusions about the relative magnitude of the dielectric constant in the WZ and ZB phases.

Chapter 8

Applications and outlook

In this chapter, we discuss possible applications of WZ GaP nanowires. The direct band gap of WZ GaP wires is promising for visible LEDs and for photoelectrochemical (PEC) cells for hydrogen production. Tunability of the optical emission across the visible range is achieved by using ternary AlGaP and GaAsP nanowires, providing an important feature for new generation LEDs and PEC devices. Solar water splitting for hydrogen production is demonstrated using p-type WZ GaP wires, achieving a new record efficiency for this material with respect to bulk samples. Furthermore, the lattice match between GaP and Silicon allows epitaxial growth and crystal structure transfer when grown in a core/shell nanowire structure. The growth of core/shell WZ GaP/Si nanowires is shown, reducing the distance between the integration of Silicon with photonics.

8.1 On the road to green LEDs

White light-emitting diodes (LEDs) are currently limited in the efficiency, due to a lack of semiconductor materials which can efficiently emit green light⁷¹. There are only few semiconductors with a band gap energy corresponding to green light, and each of these has a specific fundamental problem^{71,147–149}. AlP and GaP have an indirect band gap resulting in very low emission efficiency. The external quantum efficiency (EQE) of green emitting LEDs is around 10%, and the current best solution is to use phosphors to convert blue/UV light into green¹⁴⁹.

8.1.1 Tunability of the optical emission

WZ GaP has a direct band gap and the band gap energy can be modified by ternary compound semiconductor materials to achieve a wider range for the optical emission⁷. To address the emission tunability across a significant portion of the visible range, WZ $\text{Al}_x\text{Ga}_{1-x}\text{P}$ and $\text{GaAs}_y\text{P}_{1-y}$ ternary compound nanowires are grown. In Fig. 8.1 the emission spectra of ternary compounds with different

compositions are shown. Partial substitution of Ga by Al induces a blue-shift of the emission up to 2.234 eV with an Al concentration of 46%, while substitution of P by As induces a red-shift of the emission down to 1.797 eV with an As concentration of 70%, demonstrating that the emission color can be adjusted for a range of visible wavelengths, which is important for solid state lighting.

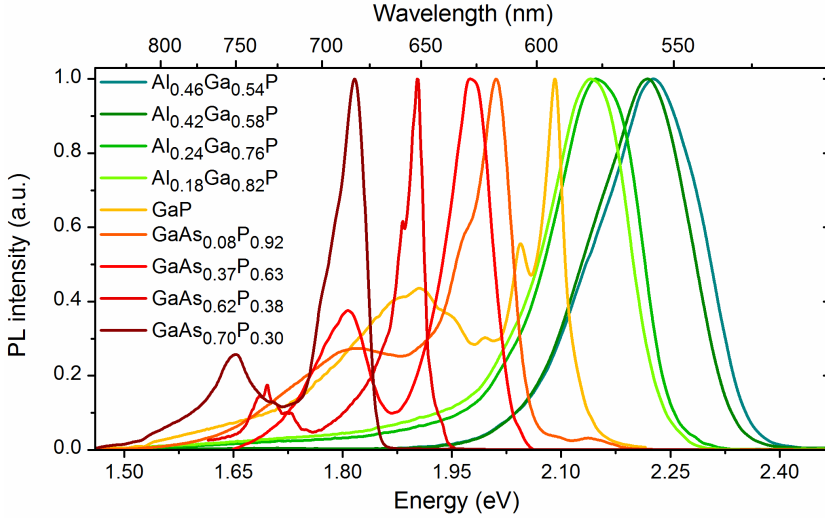


Figure 8.1: Photoluminescence spectra of WZ $\text{Al}_x\text{Ga}_{1-x}\text{P}$ and $\text{GaAs}_y\text{P}_{1-y}$ ternary compound wires, showing the tunability of the emission wavelength. Substitution of Ga by Al induces a blueshift, and substitution of P by As a redshift of the emission. All measurements are performed at 4K.

The PL lifetime has been determined for the different compositions, and Fig. 8.2 shows that the lifetime is between 0.5 and 1 ns for all samples. It is important to mention that the emission intensity and lifetime of $\text{GaAs}_y\text{P}_{1-y}$ ternary nanowires are independent on the As composition, unlike in the case of bulk ZB $\text{GaAs}_y\text{P}_{1-y}$, which has a direct/indirect energy gap crossover point at a composition of $y=0.57$ ¹⁵⁰. This confirms that these wurtzite ternary nanowires preserve the direct nature of the band structure over the whole compositional range.

8.1.2 p-n junctions for LEDs

Radial p-n heterostructures are commonly used in nanowire based LEDs¹³. In order to obtain p-n junctions in GaP nanowires zinc and sulfur precursors are introduced during growth. However, the addition of dopants during growth could affect the crystallinity of the wires. Sulfur is expected to have a small influence on the purity of the WZ phase¹⁰. Instead, the addition of zinc could increase the WZ stacking fault density due to the tendency to promote the formation of the ZB phase^{10,80}. As it will be shown in the next section, the purity of the WZ phase is barely affected by the presence of zinc during growth, with a stacking fault density that remains lower than 1 SF/ μm . Thus, the p-n core/shell nanowire growth can

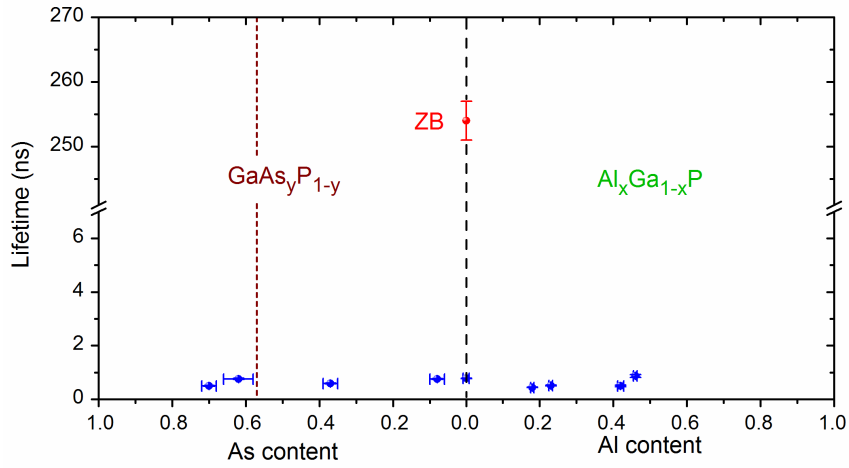


Figure 8.2: Radiative lifetimes as a function of the different wurtzite $\text{Al}_x\text{Ga}_{1-x}\text{P}$ and $\text{GaAs}_y\text{P}_{1-y}$ compositions (blue data points). The ZB GaP substrate lifetime is at 254 ns (red point). The dotted line at 57% As indicates the direct/indirect transition for zinc blende GaAsP material.

be developed on a p-type GaP substrate. Next, the LED device can be realized by following a similar approach to the one developed for solar cells application^{9,10}. An example of a possible layout for a WZ GaP LED device is shown in Fig. 8.3, where the nanowires are embedded in a benzocyclobutene (BCB) layer and then the top transparent indium-tin-oxide (ITO) contact is deposited by sputtering.

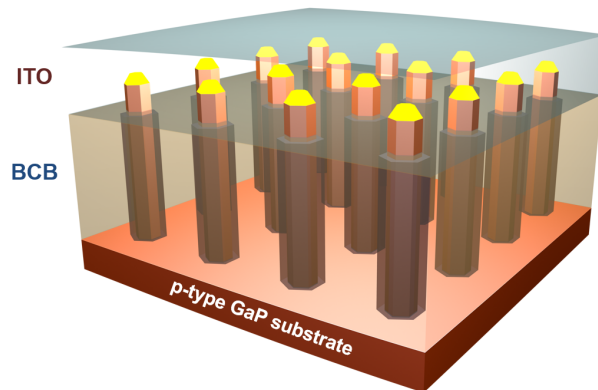


Figure 8.3: Possible layout of WZ GaP nanowire LED device. Courtesy of L. Gagliano.

8.2 Solar water splitting

Semiconductor photoelectrochemical (PEC) cells are a promising option for direct conversion of solar energy to fuels. A p-type semiconductor, acting as a photocathode, in contact with water allows for clean hydrogen production. In order to reach a high efficiency in the PEC cell it is important that the semiconductor has a band gap in the range of 1.7-2.2 eV, and band-edge position with respect to the redox system¹⁵¹. In addition, the semiconductor should have a good chemical stability to ensure long-term operation. Most semiconductors can only perform either the oxidation or the reduction of water, or require an external bias to achieve water splitting. Instead, zinc blende GaP can satisfy most of those requirements. It has reasonable stability in aqueous solution, can be grown with high stoichiometric control, and ZB p-GaP photocathodes and n-GaP photoanodes have been demonstrated in the past¹⁵². However, the low currents reported are a direct consequence of the indirect band gap of ZB GaP, leading to poor light absorption. The latter issue can be solved by moving to pure WZ GaP nanowires, where the direct band gap enhances the light absorption, hence the performance of the PEC cell.

In collaboration with Anthony Standing, we developed PEC devices consisting of p-type WZ GaP wires. By optimizing length and diameter of the nanowires, reflection of the incident light and bulk recombination losses are reduced. This, combined with the deposition of a Platinum catalyst, allow us to achieve a high efficiency of 2.9%, which compares to the 0.3% obtained with bulk GaP electrodes¹⁵¹. We note here that an additional advantage of a nanowire device is that it will use only a fraction of the semiconductor material that a thin film device would use. Furthermore, the nanowire arrays can be transferred from the growth substrate into a flexible polymer film (PDMS)¹⁵¹, which allows reduction in the cost of the substrates, and a flexible device with minimal material usage (1 gram of GaP/m²) can be produced. Nanoimprint and PDMS sample transfer are scalable technologies, which will allow for the production of large-area devices in the future.

8.2.1 Behavior of a PEC cell

When the semiconductor electrode is placed in an electrolyte solution, a thermal equilibrium between the two phases must be reached. This is satisfied when the Fermi level of the semiconductor and the redox potential of the electrolyte solution are the same¹⁵³. However, in case of a p-type semiconductor a movement of charges must occur to compensate for the different positions of the Fermi levels, resulting in a depletion layer at the interface between the semiconductor and the solution, as shown in Fig. 8.4a.

When an external, positive, potential is applied to the semiconductor, the Fermi level shifts to a lower energy, together with the band edges, reducing the depletion region. The energy levels at the interface, however, are not affected by the applied bias. Therefore, the magnitude and the direction of the band bending will depend on the applied potential. When no light source is supplied (dark), three regimes are observed in case of a p-type semiconductor:

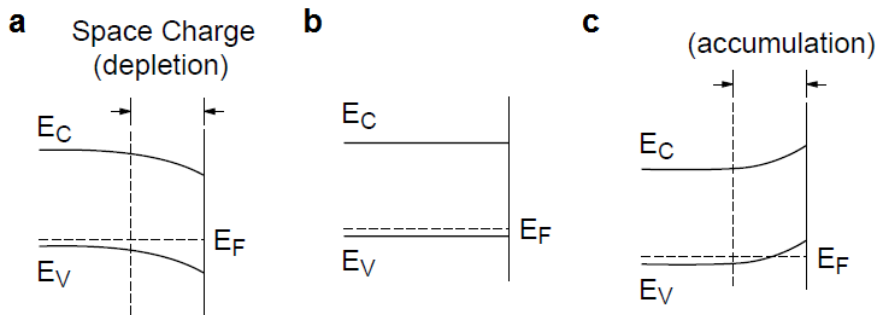


Figure 8.4: (a-c) Effect of the applied potential on the band edges in a p-type semiconductor in dark. Adapted from Ref. ¹⁵³.

1. Flatband: when the applied potential is such that the Fermi energy is at the same energy of the solution redox potential, and no band bending is observed (Fig. 8.4b). The potential associated with this situation is called the flatband potential E_{fb} ;
2. Accumulation: potentials more positive than the E_{fb} . The carriers can react at the surface of the semiconductor either with the material itself or with redox species in the electrolyte, oxidizing either water into O_2 (anode behavior), or in most cases oxidizing the electrode itself (Fig. 8.4c);
3. Depletion: at negative potentials lower than the E_{fb} . Very few (minority) charge carriers are available for charge transfer, the reaction is almost inhibited, and no current is generated (Fig. 8.4a).

Those regimes are visible in the typical behavior of the PEC cell for a p-type semiconductor shown in Fig. 8.5. Under solar illumination, electron-hole pairs which are generated by photon absorption in the proximity of the space-charge region are separated by the built-in electric field ¹⁵⁴. The photogenerated carriers are either extracted during the water splitting process, recombine radiatively, or lose energy as heat. When the applied bias is more negative than E_{fb} accumulation of electrons at the interface with the solution occurs, capturing holes from the solution and reducing the water into H_2 (cathode behavior).

In analogy with solar cells, the flatband potential E_{fb} is the theoretical limit of the open circuit potential V_{OC} , which is defined as the potential where the current is 0 A. The maximum current achieved under illumination with no applied bias is called short circuit current I_{SC} . The fill factor (FF) is defined as the ratio of the maximum power from the PEC ($i_{max}V_{max}$) to the product of the I_{SC} and V_{OC} . The efficiency η is estimated from:

$$\eta(\%) = FF \frac{i_{max}V_{max}}{P_{in}A} 100, \quad (8.1)$$

where P_{in} is the intensity of the light incident on the sample (mW/cm^2), and A is the sample area (cm^2). The reference potentials reported here are converted

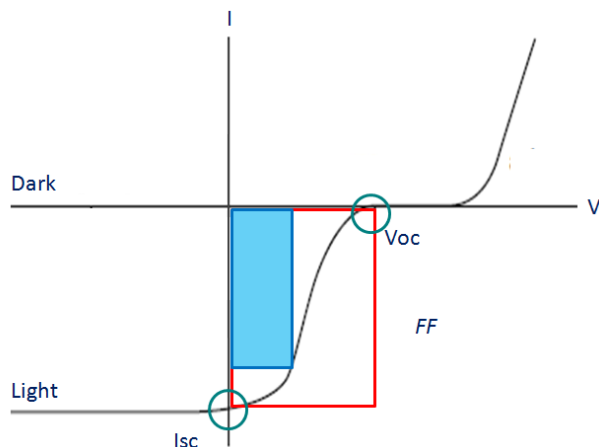


Figure 8.5: (a) Typical behavior of a p-type semiconductor in the dark and under illumination.

to the Reversible Hydrogen Electrode (RHE) potential for convenience. The efficiency calculated for the photocathode is referenced to a hypothetical cathode with no overpotential losses at 0 V vs RHE.

The setup used in the measurements is shown in Fig. 8.6. The PEC measurements are performed in a three-electrode electrochemical cell with a saturated calomel reference electrode (SCE) and a Pt foil counter electrode in 1M HClO_4 electrolyte. 100 mW/cm^2 AM 1.5G illumination is provided by a 300 W Xenon Lamp.

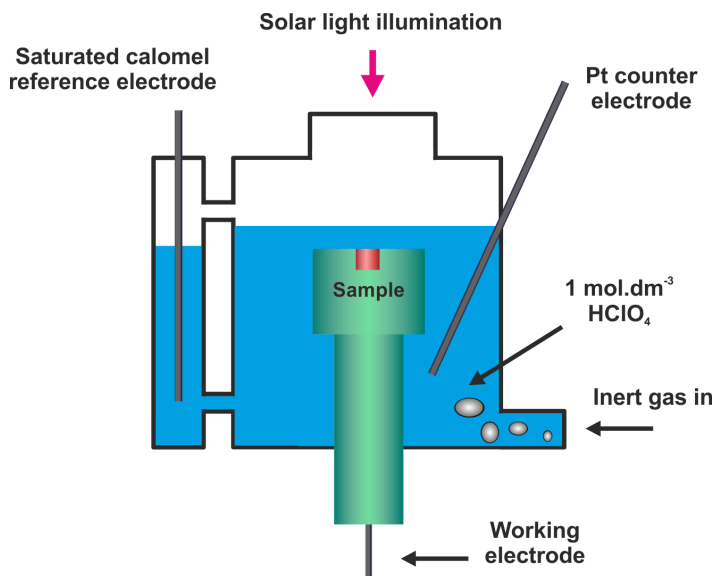


Figure 8.6: Sketch of the experimental setup.

8.2.2 Nanowires versus substrate

The pure WZ p-GaP nanowires are grown in nanoimprint arrays on a Zn-doped GaP substrate (Fig. 8.7a) for use as photocathodes for the production of hydrogen from water. In order to induce a p-type doping a Di-Ethyl Zinc (DEZn) flow (molar fraction 3.4×10^{-4}) is used. The wires used have an almost perfect WZ crystal structure, with a very low stacking fault density of $< 1 \mu\text{m}^{-1}$. The nanowires used in this experiment are of optimized geometry, with lengths and diameters of $\sim 2.0 \mu\text{m}$ and $\sim 150 \text{ nm}$, respectively. The nanowire length is controlled by adjusting the growth time of the core, while the diameter is adjusted by the growth of the p-GaP shell on the nanowire surface. An amorphous Platinum catalyst is deposited on both the planar and the nanowire samples to reduce recombination and enhance charge transfer.

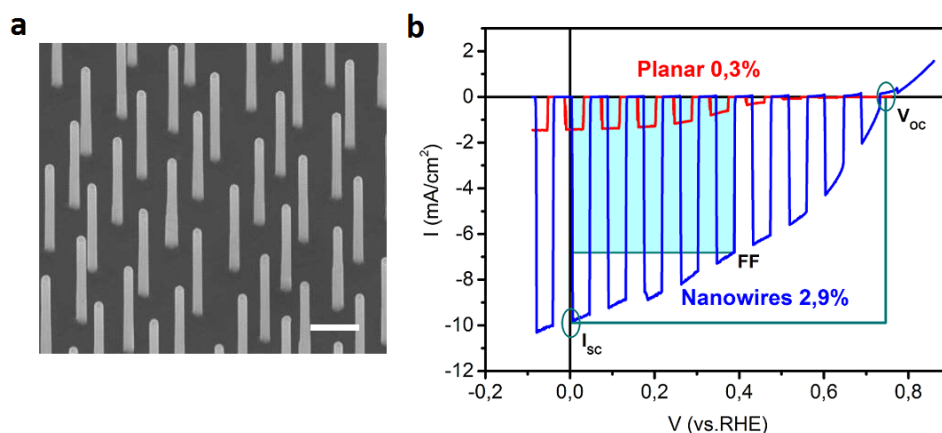


Figure 8.7: (a) SEM image of a typical array of p-GaP nanowires defined by nanoimprint lithography (tilting angle 30°). Scale bar: 400 nm. (b) I-V curves for direct comparison of nanowire (red) and planar (black) samples with Pt catalyst, performed under chopped $100 \text{ W}/\text{cm}^2$ AM1.5 illumination, in aqueous solution pH_0 with HClO_4 as supporting electrolyte. Also showing V_{OC} , I_{SC} and FF (empty square/filled square)¹⁵¹.

Figure 8.7b compares the current density-voltage (I-V) behavior of ZB planar (100)-oriented p-GaP single crystalline substrate and WZ nanowire p-GaP electrodes. The dips in the I-V curve are due to the use of chopped illumination to avoid noise caused by H_2 bubble formation during the reaction. The WZ GaP nanowire sample has a higher V_{OC} , I_{SC} and FF than the planar sample, resulting in a much higher efficiency up to 2.9% compared to the 0.3% of the bulk. Important to mention is that the planar ZB GaP sample already shows similar V_{OC} and I_{SC} values compared to recently reported best values for planar ZB GaP¹⁵².

8.3 Hexagonal Silicon

The integration of Silicon with photonics could bring low-cost highly integrated optical interconnects⁷⁰. Currently, the performance of Si-based optical devices are severely limited by the indirect nature of the band gap of bulk Silicon, which does not allow efficient optical emission from this material. In cubic Silicon the indirect band gap of 1.13 eV lies in the way from the Γ - to the X-point, while the direct band gap at the Γ point is of 3.35 eV^{33,155,156}. However, in case this material is grown with a different crystal symmetry such as hexagonal Silicon a dramatic change in the band structure is predicted. The indirect band gap of 0.79-0.85 eV is now predicted at the M-point, while a direct band gap of 1.48-1.6 eV is expected at the Γ point^{156,157}. In addition, by applying uniaxial strain a crossing between the indirect/direct band gap is expected^{158,159}, resulting in possible efficient optical emission from hexagonal Silicon.

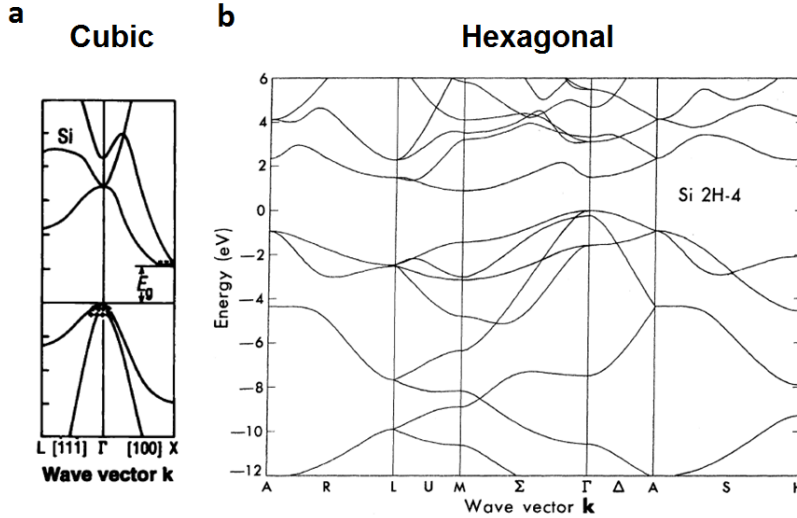


Figure 8.8: (a) Band structure calculation for cubic Silicon showing the indirect band gap toward the X-point. Adapted from Ref.¹⁵⁵. (b) Band structure calculation for hexagonal Silicon showing the indirect band gap at the M-point. Adapted from Ref.¹⁵⁷.

In collaboration with Ikaros H. Hauge, we achieved Silicon in the hexagonal phase by using core/shell nanowire heterostructure transferring the hexagonal structure from the core to the shell¹⁵. The ability of the nanowires to release the strain together with a small lattice mismatch (0.4% in zincblende/cubic structure) between GaP and Si promote the formation of a single crystalline interface. Once the growth of the WZ GaP core at 750°C is completed, the temperature is raised to 800°C and the growth of the Si shell is performed under disilane (Si_2H_6) flow¹⁰¹. Figure 8.9a corresponds to a HAADF image acquired in STEM, where the bright area represents the GaP core and the dark area corresponds to the Si shell. The EDX elemental mapping in Fig. 8.9b further demonstrates that the nanowires has a GaP/Si core/shell structure. Fig. 8.9c display a typical HRTEM image of the

nanowire viewed along the $\langle 11-20 \rangle$ zone axis, while the FFT analysis (Fig. 8.9e inset) reveals that the nanowire is single crystalline with the hexagonal structure. However, occasional defects lying in the radial direction can be observed in the nanowires. Two different mechanism are responsible of the defect formation in the Si shell. Propagation of a occasional stacking fault from the GaP core into the outer Si shell (Fig. 8.9d) or a missing plane of Si atoms in the shell, known as crack defect (Fig. 8.9e)¹⁰¹. By optimizing the Si shell growth parameters, defect-free hexagonal silicon shells with thicknesses ranging from 5 nm to 170 nm are achieved¹⁰². The approach developed here can also be used for the growth of hexagonal Germanium and SiGe compounds. Germanium has an indirect band gap at 0.66 eV in the cubic phase³³, while a direct band gap at 0.31-0.55 eV is predicted for hexagonal Ge^{156,157}. Thus, an indirect to direct band gap transition is expected in $\text{Si}_x\text{Ge}_{1-x}$ alloys for varying x content.

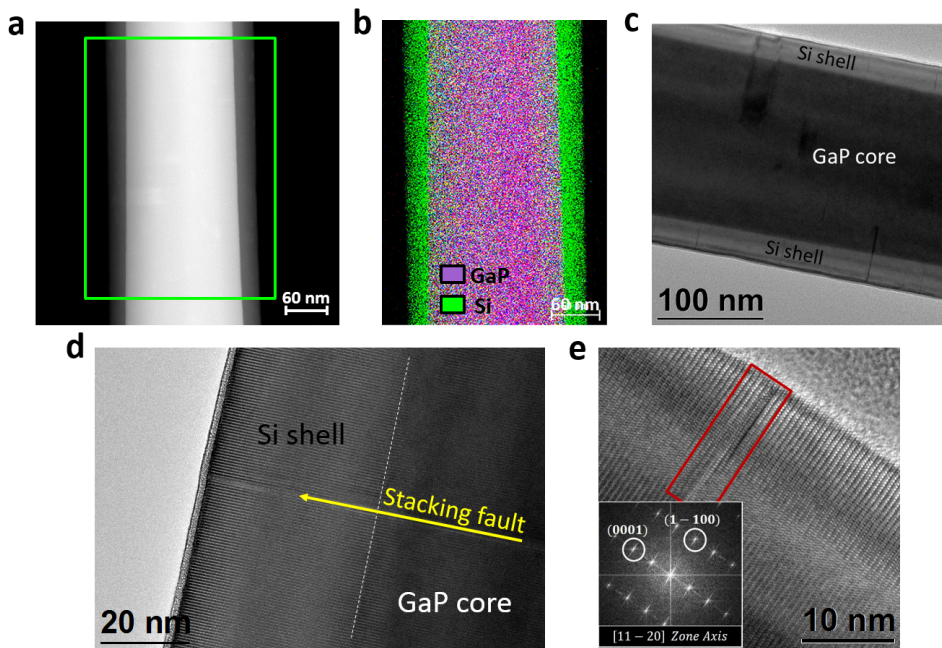


Figure 8.9: (a) HAADF image of a GaP/Si core-shell nanowire. (b) Compositional map corresponding to the green rectangle in (a), with Si shown in green and GaP in purple. (c) HRTEM images of another representative GaP-Si core-shell nanowire along the $\langle 11-20 \rangle$ zone axis. (d) HRTEM image along the $\langle 11-20 \rangle$ zone axis of a GaP/Si core-shell exhibiting the stacking fault defect transferred from the GaP core to the Si shell. (e) HRTEM image along the $\langle 11-20 \rangle$ zone axis of a GaP/Si core-shell showing a crack defect. Inset: FFT image of the nanowire. Adapted from Ref.¹⁰¹.

Chapter A

Appendix

A.1 Estimation of IQE and NRE

The IQE and NRE of the nanowires are estimated according to the model developed by Yoo et al.¹¹³. This model is based on the rate equation, which correlate the total generation rate (G) with the individual recombination rate, according to the formula:

$$G = An + Bn^2 + Cn^3, \quad (\text{A.1})$$

where A , B , and C are the coefficients for the Shockley-Read-Hall (SRH) non-radiative recombination, radiative recombination and Auger non-radiative recombination, respectively, and n is the carrier concentration.

The integrated PL intensity as a function of the excitation power density can be fitted according to the formula:

$$P_{\text{Laser}} = P_1 I_{\text{PL}}^{0.5} + P_2 I_{\text{PL}} + P_3 I_{\text{PL}}^{1.5}, \quad (\text{A.2})$$

where P_{Laser} is the excitation power density, I_{PL} the integrated PL intensity, P_1 , P_2 , and P_3 are the fitting parameters. The former parameters can be related to the rate equation according to¹¹³:

$$\begin{aligned} P_1 &= h \frac{A}{\sqrt{B}}, \\ P_2 &= k, \\ P_3 &= l \frac{C}{B^{1.5}}, \end{aligned} \quad (\text{A.3})$$

An example of the fit for the C-line and for the 2.088-2.115 eV peaks is shown in Fig. A.1.

The IQE can be extracted from the expression:

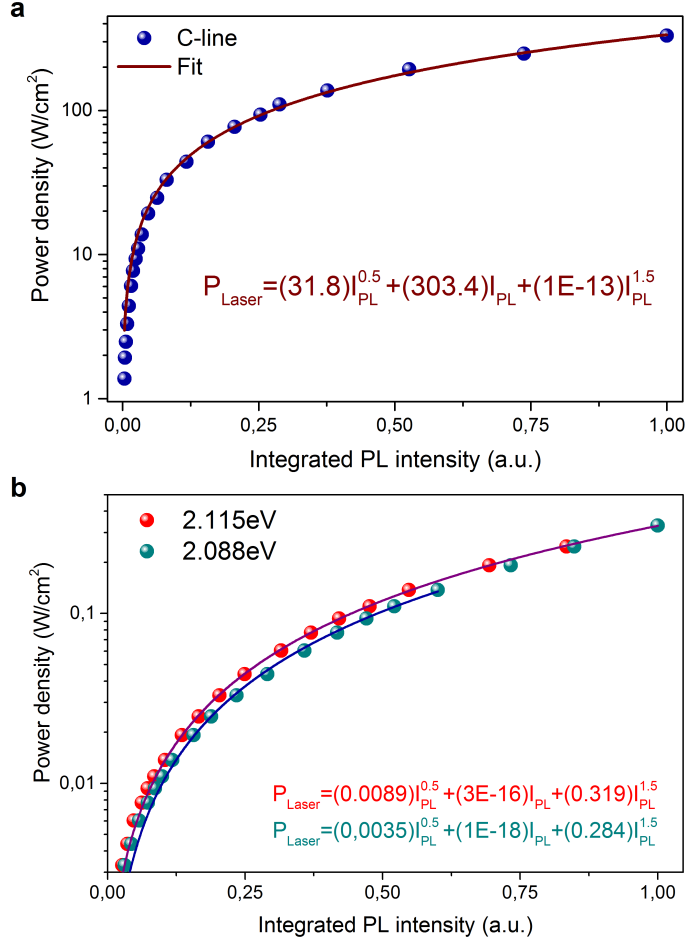


Figure A.1: (a-b) Fit of the power-dependent PL data for the C-line (a) and for the 2.088-2.115 eV peaks (b).

$$IQE = \frac{Bn^2}{G} = \frac{I_{\text{PL}}}{P_{\text{Laser}}} P_2, \quad (\text{A.4})$$

while the NRE is calculated as:

$$NRE = \frac{An + Cn^3}{G} = \frac{I_{\text{PL}}^{0.5}}{P_{\text{Laser}}} P_1 + \frac{I_{\text{PL}}^{1.5}}{P_{\text{Laser}}} P_3. \quad (\text{A.5})$$

The contributions for the SRH (An), radiative (Bn^2), and Auger (Cn^3) recombination to the IQE and NRE are shown in Fig. A.2. No Auger recombination is observed for the C-line, while the radiative recombination is close to zero for the 2.088 eV peak.

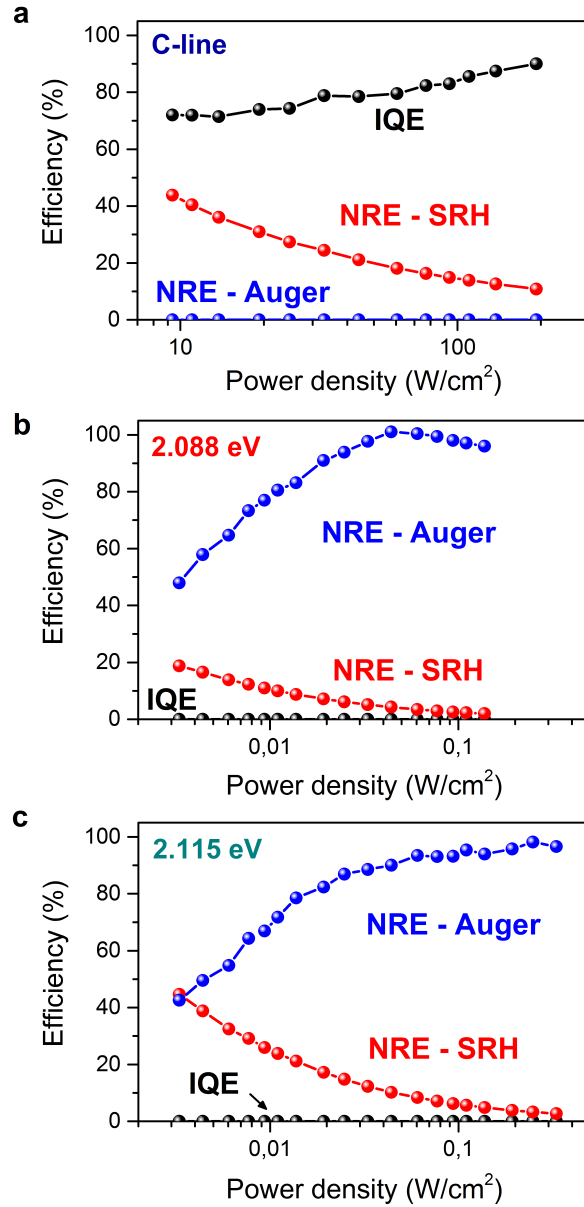


Figure A.2: (a-c) Contributions of the SRH, radiative, and Auger recombination to IQE and NRE for the C-line (a), 2.088 eV peak (b), and 2.115 eV peak (c).

A.2 PL spectra showing the B-line

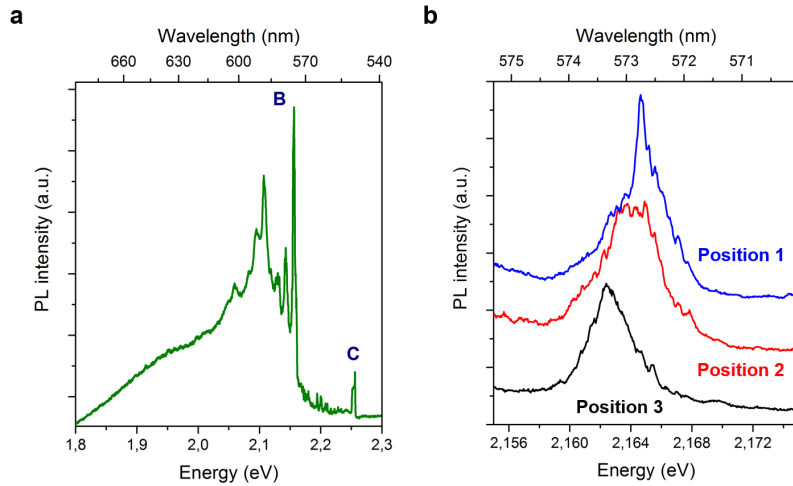


Figure A.3: (a) PL spectrum for vertical nanowires showing mainly B-line emission. Excitation power density: 130 W/cm^2 . (b) Enlarged view of the curve in (a) measured in three different positions across the sample.

A.3 Additional PLE measurements

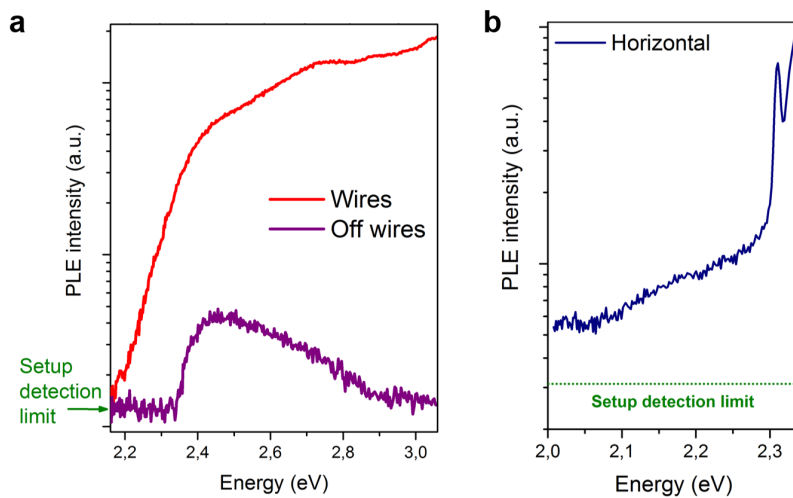


Figure A.4: (a) PLE curves measured on the vertical nanowires and over the ZB substrate. (b) PLE curve for horizontal wires showing weak signal above the setup detection limit.

References

- [1] G. E. Moore, "Cramming more components onto integrated circuits," *Electronics*, pp. 114–117, 1965.
- [2] "<http://www.intel.com.au/content/www/au/en/silicon-innovations/intel-14nm-technology.html>."
- [3] R. S. Wagner and W. C. Ellis, "Vapor-liquid-solid mechanism of single crystal growth," *Applied Physics Letters*, vol. 4, no. 1964, pp. 89–90, 1964.
- [4] K. Hiruma, M. Yazawa, T. Katsuyama, K. Ogawa, K. Haraguchi, M. Koguchi, and H. Kakibayashi, "Growth and optical properties of nanometer-scale GaAs and InAs whiskers," *Journal of Applied Physics*, vol. 77, no. 1995, pp. 447–462, 1995.
- [5] M. S. Gudiksen, L. J. Lauhon, J. Wang, D. C. Smith, and C. M. Lieber, "Growth of nanowire superlattice structures for nanoscale photonics and electronics.," *Nature*, vol. 415, no. 2, pp. 617–620, 2002.
- [6] M. T. Björk, C. Thelander, A. E. Hansen, L. E. Jensen, M. W. Larsson, L. R. Wellenberg, and L. Samuelson, "Few-electron quantum dots in nanowires," *Nano Letters*, vol. 4, pp. 1621–1625, 2004.
- [7] T. Kuykendall, P. Ulrich, S. Aloni, and P. Yang, "Complete composition tunability of InGaN nanowires using a combinatorial approach.," *Nature materials*, vol. 6, pp. 951–956, Dec. 2007.
- [8] E. Minot, F. Kelkensberg, M. van Kouwen, J. van Dam, L. P. Kouwenhoven, V. Zwiller, M. T. Borgström, O. Wunnicke, M. Verheijen, and E. P. A. M. Bakkers, "Single quantum dot nanowire LEDs," *Nano letters*, vol. 7, no. 2, pp. 367–371, 2007.
- [9] J. Wallentin, N. Anttu, D. Asoli, M. Huffman, I. Åberg, B. Witzigmann, H. Q. Xu, L. Samuelson, K. Deppert, and M. T. Borgström, "InP Nanowire Array Solar Cells Achieving 13.8% Efficiency by Exceeding the Ray Optics Limit," *Science*, vol. 339, pp. 1057–1060, 2013.
- [10] Y. Cui, J. Wang, S. R. Plissard, A. Cavalli, T. T. T. Vu, R. P. J. V. Veldhoven, L. Gao, M. Trainor, M. A. Verheijen, J. E. M. Haverkort, and E. P. A. M. Bakkers, "Efficiency Enhancement of InP Nanowire Solar Cells by Surface Cleaning," *Nano letters*, vol. 13, no. 9, pp. 4113–4117, 2013.

- [11] F. Qian, S. Gradečak, Y. Li, C. Y. Wen, and C. M. Lieber, “Core/multishell nanowire heterostructures as multicolor, high-efficiency light-emitting diodes,” *Nano Letters*, vol. 5, no. 11, pp. 2287–2291, 2005.
- [12] M. Tchernycheva, P. Lavenus, H. Zhang, a. V. Babichev, G. Jacopin, M. Shahmohammadi, F. H. Julien, R. Ciecchonski, G. Vescovi, and O. Kryliouk, “InGaN/GaN core-shell single nanowire light emitting diodes with graphene-based P-contact,” *Nano Letters*, vol. 14, no. 5, pp. 2456–2465, 2014.
- [13] Y. Ra, R. Navamathavan, J. Park, and C. Lee, “Coaxial In_xGa_{1-x}N/GaN Multiple Quantum Well Nanowire Arrays on Si (111) Substrate for High-Performance Light-Emitting Diodes,” *Nano letters*, vol. 13, no. 8, pp. 3506–3516, 2013.
- [14] M. Hocevar, G. Immink, M. Verheijen, N. Akopian, V. Zwiller, L. Kouwenhoven, and E. Bakkers, “Growth and optical properties of axial hybrid III-V/silicon nanowires.,” *Nature communications*, vol. 3, p. 1266, Jan. 2012.
- [15] R. E. Algra, M. Hocevar, M. A. Verheijen, I. Zardo, G. G. W. Immink, W. J. P. V. Enkevort, G. Abstreiter, L. P. Kouwenhoven, E. Vlieg, and E. P. A. M. Bakkers, “Crystal Structure Transfer in Core/Shell Nanowires,” *Nano letters*, vol. 11, no. 4, pp. 1690–1694, 2011.
- [16] R.-M. Ma, X.-L. Wei, L. Dai, S.-F. Liu, T. Chen, S. Yue, Z. Li, Q. Chen, and G. G. Qin, “Light Coupling and Modulation in Coupled Nanowire Ring - Fabry-Perot Cavity,” *Nano letters*, vol. 9, no. 7, pp. 2697–2703, 2009.
- [17] S. Rühle, L. K. V. Vugt, H. Li, N. A. Keizer, L. Kuipers, and D. Vanmaekelbergh, “Nature of Sub-Band Gap Luminescent Eigenmodes in a ZnO Nanowire,” *Nano letters*, vol. 8, no. 1, pp. 119–123, 2008.
- [18] M. a. Zimmler, J. Bao, F. Capasso, S. Müller, and C. Ronning, “Laser action in nanowires: Observation of the transition from amplified spontaneous emission to laser oscillation,” *Applied Physics Letters*, vol. 93, no. 5, pp. 3–5, 2008.
- [19] S. Chu, G. Wang, W. Zhou, Y. Lin, L. Chernyak, J. Zhao, J. Kong, L. Li, J. Ren, and J. Liu, “Electrically pumped waveguide lasing from ZnO nanowires.,” *Nature nanotechnology*, vol. 6, pp. 506–10, Aug. 2011.
- [20] P. Xie, Q. Xiong, Y. Fang, Q. Qing, and C. M. Lieber, “Local electrical potential detection of DNA by nanowire-nanopore sensors,” *Nature Nanotechnology*, vol. 7, no. February, pp. 119–125, 2011.
- [21] C. K. Chan, H. Peng, G. Liu, K. McIlwrath, X. F. Zhang, R. A. Huggins, and Y. Cui, “High-performance lithium battery anodes using silicon nanowires,” *Nature nanotechnology*, vol. 3, pp. 31–35, 2007.
- [22] A. I. Hochbaum, R. Chen, R. D. Delgado, W. Liang, E. C. Garnett, M. Najarian, A. Majumdar, and P. Yang, “Enhanced thermoelectric performance of rough silicon nanowires.,” *Nature*, vol. 451, no. January, pp. 163–167, 2008.
- [23] M. H. M. Van Weert, N. Akopian, U. Perinetti, M. P. Van Kouwen, R. E. Algra, M. a. Verheijen, P. a. M. B. Erik, L. P. Kouwenhoven, and V. Zwiller, “Selective excitation and detection of spin states in a single nanowire quantum dot,” *Nano Letters*, vol. 9, pp. 1989–1993, 2009.

-
- [24] V. Mourik, K. Zuo, S. M. Frolov, S. R. Plissard, E. P. a. M. Bakkers, and L. P. Kouwenhoven, “Signatures of Majorana fermions in hybrid superconductor-semiconductor nanowire devices,” *Science*, vol. 336, pp. 1003–1007, 2012.
- [25] M. T. Borgström, G. Immink, B. Ketelaars, R. Algra, and E. P. A. M. Bakkers, “Synergetic nanowire growth,” *Nature nanotechnology*, vol. 2, pp. 541–544, Sept. 2007.
- [26] I. Markov, *Crystal growth for beginners*. second ed., 2004.
- [27] C. Foxon and B. Joyce, “Interaction kinetics of As₂ and Ga on (100) GaAs surfaces,” *Surface Science*, vol. 64, pp. 293–304, 1977.
- [28] M. T. Borgström, J. Wallentin, J. Trägårdh, P. Ramvall, M. Ek, L. R. Wallenberg, L. Samuelson, and K. Deppert, “In situ etching for total control over axial and radial nanowire growth,” *Nano Research*, vol. 3, pp. 264–270, Mar. 2010.
- [29] C.-Y. Yeh, S.-H. Wei, and A. Zunger, “Relationships between the band gaps of the zinc-blende and wurtzite modifications of semiconductors,” *Physical Review B*, vol. 50, no. 4, pp. 2715–2718, 1994.
- [30] A. De and C. E. Pryor, “Predicted band structures of III-V semiconductors in the wurtzite phase,” *Physical Review B*, vol. 81, p. 155210, Apr. 2010.
- [31] F. Bechstedt and A. Belabbes, “Structure, energetics, and electronic states of III-V compound polytypes.,” *Journal of physics. Condensed matter : an Institute of Physics journal*, vol. 25, p. 273201, July 2013.
- [32] D. Kriegner, S. Assali, A. Belabbes, T. Etzelstorfer, V. Holý, T. Schüllli, F. Bechstedt, E. P. A. M. Bakkers, G. Bauer, and J. Stangl, “Unit cell structure of the wurtzite phase of GaP nanowires: X-ray diffraction studies and density functional theory calculations,” *Physical Review B*, vol. 88, p. 115315, Sept. 2013.
- [33] “<http://www.ioffe.rssi.ru/SVA/NSM/Semicond/>.”
- [34] N. Akopian, G. Patriarche, L. Liu, and V. Zwiller, “Crystal Phase Quantum Dots,” *Nano letters*, vol. 10, no. 4, pp. 1198–1201, 2010.
- [35] C. Dames and G. Chen, “Theoretical phonon thermal conductivity of Si/Ge superlattice nanowires,” *Journal of Applied Physics*, vol. 95, no. 2, pp. 682–693, 2004.
- [36] N. Vainorius, S. Lehmann, D. Jacobsson, L. Samuelson, K. a. Dick, and M.-E. Pistol, “Confinement in Thickness-Controlled GaAs Polytype Nanodots,” *Nano Letters*, vol. 15, no. 4, pp. 2652–2656, 2015.
- [37] K. A. Dick, C. Thelander, L. Samuelson, and P. Caroff, “Crystal phase engineering in single InAs nanowires.,” *Nano letters*, vol. 10, pp. 3494–3499, Sept. 2010.
- [38] P. Yu and M. Cardona, *Fundamental of Semiconductors*. third ed., 2005.
- [39] W. Kohn and L. Sham, “Self-consistent equations including exchange and correlation effects,” *Physical Review*, vol. 140, no. 4, pp. A1133–A1138, 1965.
- [40] N. Argaman and G. Makov, “Density functional theory - an introduction,” *arXiv:physics/9806013*, 1999.

References

- [41] P. Hohenberg and W. Kohn, “Inhomogeneous electron gas,” *Physical Review*, vol. 136, no. 3, pp. B864–871, 1964.
- [42] A. Belabbes, C. Panse, J. Furthmüller, and F. Bechstedt, “Electronic bands of III-V semiconductor polytypes and their alignment,” *Physical Review B*, vol. 86, pp. 075208–1–12, Aug. 2012.
- [43] T. N. Morgan, “Symmetry of electron states in GaP,” *Physical Review Letters*, vol. 21, no. 12, pp. 819–823, 1968.
- [44] M. R. Salehpour and S. Satpathy, “Comparison of electron bands of hexagonal and cubic diamond,” *Physical Review B*, vol. 41, no. 5, pp. 3048–3052, 1990.
- [45] F. Bechstedt and A. Belabbes, “In preparation,”
- [46] P. Tronc, Y. Kitaev, G. Wang, and M. Limonov, “Selection Rules for Optical Transitions Involving Impurities and Defects in Hexagonal GaN,” *Physica Status Solidi (B)*, vol. 210, pp. 471–474, Dec. 1998.
- [47] M. Grundmann, *The physics of semiconductors*. Springer, 2006.
- [48] T. Kazimierczuk, D. Fröhlich, S. Scheel, H. Stolz, and M. Bayer, “Giant Rydberg excitons in the copper oxide Cu₂O,” *Nature*, vol. 514, pp. 343–347, 2014.
- [49] P. H. Borchers, K. Kunct, G. F. Alfreyg, and R. L. Hall, “The lattice dynamics of gallium phosphide,” *Journal of Physics C: Solid State Physics*, vol. 12, pp. 4699–4706, 1979.
- [50] I. Zardo, S. Conesa-Boj, F. Peiro, J. R. Morante, J. Arbiol, E. Uccelli, G. Abstreiter, and a. Fontcuberta i Morral, “Raman spectroscopy of wurtzite and zincblende GaAs nanowires: Polarization dependence, selection rules, and strain effects,” *Physical Review B*, vol. 80, p. 245324, Dec. 2009.
- [51] H. Harima, “Properties of GaN and related compounds studied by means of Raman scattering,” *J. Phys.: Condens. Matter*, vol. 14, pp. R967–R993, 2002.
- [52] B. Pödör, “Zone edge phonons in gallium phosphide,” *Physica status solidi (b)*, vol. 120, pp. 207–213, 1983.
- [53] F. Gervais and B. Piriou, “Temperature dependence of transverse- and longitudinal-optic modes in TiO₂ (rutile),” *Physical Review B*, vol. 10, no. 4, pp. 1642–1654, 1974.
- [54] H. Alawadhi, R. Vogelgesang, A. K. Ramdas, T. P. Chin, and J. M. Woodall, “Indirect transitions, free and impurity-bound excitons in gallium phosphide: A revisit with modulation and photoluminescence spectroscopy,” *Journal of Applied Physics*, vol. 82, no. 9, pp. 4331–4337, 1997.
- [55] J. K. Hsu, C. Juang, B. J. Lee, and G. C. Chi, “Photoluminescence studies of interstitial Zn in InP due to rapid thermal annealing,” *Journal Vacuum Science and Technology B*, vol. 12, p. 1416, 1994.
- [56] U. Kaufmann, M. Kunzer, M. Maier, H. Obloh, A. Ramakrishnan, and B. Santic, “Nature of the 2.8 eV photoluminescence band in Mg doped GaN,” *Applied Physics Letters*, vol. 72, no. 11, pp. 1326–1328, 1998.

-
- [57] R. M. Sieg, B. Chatterjee, and S. A. Ringel, "Evidence for enhanced zinc interstitial concentration in strain-relaxed heteroepitaxial indium phosphide," *Applied Physics Letters*, vol. 66, no. 23, pp. 3108–3110, 1995.
- [58] J. Wang, S. R. Plissard, M. a. Verheijen, L.-F. Feiner, A. Cavalli, and E. P. A. M. Bakkers, "Reversible switching of InP nanowire growth direction by catalyst engineering.," *Nano letters*, vol. 13, pp. 3802–6, Aug. 2013.
- [59] M. A. Verschuuren and S. F. Wuister, "Imprint lithography," 2008.
- [60] T. W. Odom, J. C. Love, D. B. Wolfe, K. E. Paul, and G. M. Whitesides, "Composite Stamps," *Langmuir*, vol. 18, no. 9, pp. 5314–5320, 2002.
- [61] T. Martensson, P. Carlberg, M. Borgström, L. Montelius, W. Seifert, and L. Samuelson, "Nanowire arrays defined by nanoimprint lithography," *Nano Letters*, vol. 4, no. 4, pp. 699–702, 2004.
- [62] M. A. Verschuuren and H. V. Sprang, "3D Photonic Structures by Sol-Gel Imprint Lithography," in *MRS Spring meeting*, 2007.
- [63] M. McCord and M. Rooks, *Handbook of microlithography, micromachining and microfabrication. Volume 1: microlithography*. 1997.
- [64] G. Stringfellow, *Organometallic Vapor-Phase epitaxy: theory and practice*. second ed., 1999.
- [65] "www.zeiss.com."
- [66] "<http://cbe.ivic.vt.edu/mic250/pdf/thesebook-chap3.pdf>."
- [67] M. Heiss, Y. Fontana, A. Gustafsson, G. Wüst, C. Magen, D. D. O'Regan, J. W. Luo, B. Ketterer, S. Conesa-Boj, A. V. Kuhlmann, J. Houel, E. Russo-Averchi, J. R. Morante, M. Cantoni, N. Marzari, J. Arbiol, A. Zunger, R. J. Warburton, and A. Fontcuberta i Morral, "Self-assembled quantum dots in a nanowire system for quantum photonics.," *Nature materials*, vol. 12, pp. 439–44, May 2013.
- [68] G. H. Glover, "Study of electron energy relaxation times in GaAs and InP," *Journal of Applied Physics*, vol. 44, no. 1973, pp. 1295–1301, 1973.
- [69] P. Landsberg, *Recombination in semiconductors*. 1991.
- [70] M. Paniccia, "Integrating silicon photonics," *Nature Photonics*, vol. 4, pp. 498–499, Aug. 2010.
- [71] S. Nakamura, "Current Status of GaN-based solid-state lighting," *MRS Bulletin*, vol. 34, pp. 101–107, 2009.
- [72] C.-Y. Yeh, Z. W. Lu, S. Froyen, and A. Zunger, "Zinc-blende-wurtzite polytypism in semiconductors," *Physical Review B*, vol. 46, no. 16, pp. 10086–10097, 1992.
- [73] R. E. Algra, M. A. Verheijen, M. T. Borgström, L.-F. Feiner, G. Immink, W. J. P. van Enckevort, E. Vlieg, and E. P. a. M. Bakkers, "Twinning superlattices in indium phosphide nanowires.," *Nature*, vol. 456, pp. 369–372, Nov. 2008.
- [74] P. Caroff, K. A. Dick, J. Johansson, M. E. Messing, K. Deppert, and L. Samuelson, "Controlled polytypic and twin-plane superlattices in iii-v nanowires.," *Nature nanotechnology*, vol. 4, pp. 50–55, Jan. 2009.

References

- [75] H. Shtrikman, R. Popovitz-Biro, A. Kretinin, L. Houben, M. Heiblum, M. Bukala, M. Galicka, R. Buczko, and P. Kacman, "Method for suppression of stacking faults in Wurtzite III-V nanowires.," *Nano letters*, vol. 9, pp. 1506–10, Apr. 2009.
- [76] H. J. Joyce, J. Wong-Leung, Q. Gao, H. H. Tan, and C. Jagadish, "Phase perfection in zinc Blende and Wurtzite III-V nanowires using basic growth parameters," *Nano letters*, vol. 10, pp. 908–915, Mar. 2010.
- [77] S. Assali, I. Zardo, S. Plissard, D. Kriegner, M. A. Verheijen, G. Bauer, A. Meijerink, A. Belabbes, F. Bechstedt, J. E. M. Haverkort, and E. P. A. M. Bakkers, "Direct band gap wurtzite gallium phosphide nanowires.," *Nano letters*, vol. 13, pp. 1559–1563, Apr. 2013.
- [78] M. Murayama and T. Nakayama, "Chemical trend of band offsets at wurtzite/zincblende heterocrystalline semiconductor interfaces," *Physical Review B*, vol. 49, no. 7, pp. 4710–4724, 1994.
- [79] M. Verheijen, R. E. Algra, M. T. Borgström, G. Immink, E. Sourty, W. J. P. van Enkevort, E. Vlieg, and E. P. A. M. Bakkers, "Three-dimensional morphology of GaP-GaAs nanowires revealed by transmission electron microscopy tomography," *Nano letters*, vol. 7, no. 10, pp. 3051–3055, 2007.
- [80] R. E. Algra, M. A. Verheijen, L.-F. Feiner, G. G. W. Immink, W. J. P. V. Enkevort, E. Vlieg, and E. P. a. M. Bakkers, "The role of surface energies and chemical potential during nanowire growth.," *Nano letters*, vol. 11, pp. 1259–1264, Mar. 2011.
- [81] F. Glas, "Chemical potentials for Au-assisted vapor-liquid-solid growth of III-V nanowires," *Journal of Applied Physics*, vol. 108, pp. 1–6, 2010.
- [82] L.-F. Feiner and S. Breuer, "Phase diagram for GaP nanowire growth from the nucleation model including positional entropy," p. In preparation.
- [83] A. Berg, S. Lehmann, N. Vainorius, A. Gustafsson, M.-E. Pistol, L. R. Wallenberg, L. Samuelson, and M. T. Borgström, "Growth and characterization of wurtzite GaP nanowires with control over axial and radial growth by use of HCl in-situ etching," *Journal of Crystal Growth*, vol. 386, pp. 47–51, Jan. 2014.
- [84] F. Oehler, P. Gentile, T. Baron, and P. Ferret, "The effects of HCl on silicon nanowire growth: surface chlorination and existence of a 'diffusion-limited minimum diameter'," *Nanotechnology*, vol. 20, p. 475307, 2009.
- [85] N. Skold, L. S. Karlsson, M. W. Larsson, M.-E. Pistol, W. Seifert, J. Tragardh, and L. Samuelson, "Growth and Optical Properties of Strained GaAs-GaxIn1-xP Core-Shell Nanowires," *Nano Letters*, vol. 5, no. 10, pp. 1943–47, 2005.
- [86] N. Sköld, J. B. Wagner, G. Karlsson, T. Hernán, W. Seifert, M.-E. Pistol, and L. Samuelson, "Phase segregation in AlInP shells on GaAs nanowires.," *Nano letters*, vol. 6, no. 12, pp. 2743–2747, 2006.
- [87] D. Kriegner, C. Panse, B. Mandl, and K. Dick, "Unit cell structure of crystal polytypes in InAs and InSb nanowires," *Nano letters*, vol. 11, no. 4, pp. 1483–1489, 2011.

-
- [88] M. E. Reimer, G. Bulgarini, N. Akopian, M. Hocevar, M. B. Bavinck, M. a. Verheijen, E. P. A. M. Bakkers, L. P. Kouwenhoven, and V. Zwiller, “Bright single-photon sources in bottom-up tailored nanowires,” *Nature Communications*, vol. 3, no. 737, pp. 1–6, 2012.
- [89] G. Juska, V. Dimastrodonato, L. O. Mereni, A. Gocalinska, and E. Pelucchi, “Towards quantum-dot arrays of entangled photon emitters,” *Nature Photonics*, vol. 7, pp. 527–531, 2013.
- [90] V. Fiorentini, F. Bernardini, F. Della Sala, A. Di Carlo, and P. Lugli, “Effects of macroscopic polarization in III-V nitride multi-quantum-wells,” *Physical Review B*, vol. 60, no. 12, pp. 8849–8858, 1999.
- [91] J. Bolinsson, P. Caroff, B. Mandl, and K. A. Dick, “Wurtzite-zincblende superlattices in InAs nanowires using a supply interruption method,” *Nanotechnology*, vol. 22, p. 265606, July 2011.
- [92] A. Belabbes, J. Furthmüller, and F. Bechstedt, “Relation between spontaneous polarization and crystal field from first principles,” *Physical Review B*, vol. 87, p. 035305, Jan. 2013.
- [93] J. Lähnemann, O. Brandt, U. Jahn, C. Pfüller, C. Roder, P. Dogan, F. Grosse, A. Belabbes, F. Bechstedt, A. Trampert, and L. Geelhaar, “Direct experimental determination of the spontaneous polarization of GaN,” *Physical Review B*, vol. 86, pp. 081302(R)–1–5, Aug. 2012.
- [94] R. E. Algra, M. a. Verheijen, L. F. Feiner, G. G. W. Immink, R. Theissmann, W. J. P. Van Enckevort, E. Vlieg, and E. P. a. M. Bakkers, “Paired twins and {11-2} morphology in GaP nanowires,” *Nano Letters*, vol. 10, pp. 2349–2356, 2010.
- [95] Y.-C. Chou, K. Hillerich, J. Tersoff, M. C. Reuter, K. A. Dick, and F. M. Ross, “Atomic-Scale Variability and Control of III-V Nanowire Growth Kinetics,” *Science*, vol. 343, pp. 281–284, 2014.
- [96] F. Glas, J.-C. Harmand, and G. Patriarche, “Why Does Wurtzite Form in Nanowires of III-V Zinc Blende Semiconductors?,” *Physical Review Letters*, vol. 99, p. 146101, Oct. 2007.
- [97] J. Lähnemann, U. Jahn, O. Brandt, T. Flissikowski, P. Dogan, and H. T. Grahn, “Luminescence associated with stacking faults in GaN,” *Journal of Physics D: Applied Physics*, vol. 423001, pp. 1–14, 2014.
- [98] M. A. M. Versteegh, M. E. Reimer, K. D. Jöns, D. Dalacu, P. J. Poole, A. Gulinatti, A. Giudice, and V. Zwiller, “Polarization-entangled photon pairs from a nanowire quantum dot,” *Nature communications*, vol. 5, pp. 1–9, 2014.
- [99] L. K. V. Vugt, S. Rühle, and D. Vanmaekelbergh, “Phase-Correlated Nondirectional Laser Emission from the End Facets of a ZnO Nanowire,” *Nano letters*, vol. 6, no. 12, pp. 2707–2711, 2006.
- [100] O. Blum, I. J. Fritz, L. R. Dawson, a. J. Howard, T. J. Headley, J. F. Klem, and T. J. Drummond, “Highly reflective, long wavelength AlAsSb/GaAsSb distributed Bragg reflector grown by molecular beam epitaxy on InP substrates,” *Applied Physics Letters*, vol. 66, no. 3, pp. 329–331, 1995.

- [101] S. Conesa-Boj, H. Hauge, M. Verheijen, S. Assali, A. Li, E. P. A. M. Bakkers, and A. Fontcuberta i Morral, “Cracking the Si Shell Growth in Hexagonal GaP-Si Core-Shell Nanowires,” *Nano Letters*, vol. 15, no. 5, pp. 2974–2979, 2015.
- [102] H. Hauge, M. A. Verheijen, S. Conesa-Boj, T. Etzelstorfer, M. Watzinger, D. Kriegner, I. Zardo, C. Fasolato, F. Capitani, P. Postorino, S. Kolling, A. Li, S. Assali, J. Stangl, and E. P. A. M. Bakkers, “Hexagonal Silicon Realized, under review,”
- [103] A. B. Slimane, A. Najar, R. Elafandy, D. P. San-Román-Alerigi, D. Anjum, T. K. Ng, and B. S. Ooi, “On the phenomenon of large photoluminescence red shift in GaN nanoparticles.,” *Nanoscale research letters*, vol. 8, p. 342, Jan. 2013.
- [104] E. Burstein, “Anomalous optical absorption limit in InSb,” *Physical Review*, vol. 93, pp. 632–633, 1954.
- [105] J. K. Panda, A. Roy, M. Gemmi, E. Husanu, A. Li, D. Ercolani, and L. Sorba, “Electronic band structure of wurtzite GaP nanowires via temperature dependent resonance Raman spectroscopy,” *Applied Physics Letters*, vol. 103, no. 2, p. 023108, 2013.
- [106] P. Dean and D. Thomas, “Intrinsic Absorption-Edge Spectrum of Gallium Phosphide,” *Physical Review*, vol. 150, pp. 690–703, Oct. 1966.
- [107] P. Krogstrup, H. I. Jørgensen, M. Heiss, O. Demichel, J. V. Holm, M. Aagesen, J. Nygard, and A. Fontcuberta i Morral, “Single-nanowire solar cells beyond the Shockley-Queisser limit,” *Nature Photonics*, vol. 7, no. March, pp. 1–5, 2013.
- [108] A. J. Standing, S. Assali, J. E. M. Haverkort, and E. P. A. M. Bakkers, “High yield transfer of ordered nanowire arrays into transparent flexible polymer films.,” *Nanotechnology*, vol. 23, pp. 495305–1–5, Dec. 2012.
- [109] G. Grzela, R. Paniagua-Domínguez, T. Barten, Y. Fontana, J. A. Sánchez-Gil, and J. G. Rivas, “Nanowire Antenna Emission,” *Nano letters*, vol. 12, no. 11, pp. 5481–5486, 2012.
- [110] C. J. Hwang, “Lifetimes of Free and Bound Excitons in High-Purity GaAs,” *Physical Review B*, vol. 8, no. 2, pp. 646–652, 1973.
- [111] P. Dean, “Absorption and luminescence of excitons at neutral donors in Gallium Phosphide,” *Physical Review*, vol. 157, no. 3, pp. 655–667, 1967.
- [112] T. Schmidt, K. Lischka, and W. Zulehner, “Excitation-power dependence of the near-band-edge photoluminescence of semiconductors,” *Physical Review B*, vol. 45, no. 16, pp. 8989–8994, 1992.
- [113] Y.-S. Yoo, T.-M. Roh, J.-H. Na, S. J. Son, and Y.-H. Cho, “Simple analysis method for determining internal quantum efficiency and relative recombination ratios in light emitting diodes,” *Applied Physics Letters*, vol. 102, no. 21, p. 211107, 2013.
- [114] Q. Gao, D. Saxena, F. Wang, L. Fu, S. Mokkaapati, Y. Guo, L. Li, J. Wong-Leung, P. Caroff, H. H. Tan, and C. Jagadish, “Selective-Area Epitaxy of Pure Wurtzite InP Nanowires: High Quantum Efficiency and Room-Temperature Lasing.,” *Nano letters*, vol. 14, pp. 5206–11, Sept. 2014.

-
- [115] W. Shockley and W. T. Read, "Statistics of the Recombination of Holes and Electrons," *Physical Review*, vol. 87, no. 5, pp. 835–842, 1952.
- [116] R. Hall, "Electron-hole recombination in germanium," *Physical Review*, vol. 87, no. 5, p. 387, 1952.
- [117] W. Guo, M. Zhang, P. Bhattacharya, and J. Heo, "Auger recombination in III-nitride nanowires and its effect on nanowire light-emitting diode characteristics.," *Nano letters*, vol. 11, pp. 1434–8, Apr. 2011.
- [118] M. Smith, J. Lin, X. Jiang, A. Khan, Q. Chen, A. Salvador, A. Botchkarev, W. Kim, and H. Morkoc, "Exciton-phonon interaction in InGaN/GaN and GaN/AlGaIn multiple quantum wells," *Applied Physics Letters*, vol. 70, no. 21, pp. 2882–2884, 1997.
- [119] P. Varshni, "Temperature dependence of the energy gap in semiconductors," *Physica*, vol. 34, pp. 149–154, 1967.
- [120] M. Leroux, N. Grandjean, B. Beaumont, G. Nataf, F. Semond, J. Massies, and P. Gibart, "Temperature quenching of photoluminescence intensities in undoped and doped GaN," *Journal of Applied Physics*, vol. 86, no. 7, pp. 3721–3728, 1999.
- [121] M. De Luca, G. Lavenuta, A. Polimeni, S. Rubini, V. Grillo, F. Mura, A. Miriametro, M. Capizzi, and F. Martelli, "Excitonic recombination and absorption in In_xGa_{1-x}As/GaAs heterostructure nanowires," *Physical Review B*, vol. 87, p. 235304, June 2013.
- [122] C. Klingshirn, "65 years of ZnO research - old and very recent results," *Physica Status Solidi (B)*, vol. 247, pp. 1424–1447, Apr. 2010.
- [123] C. J. Chou and G. F. Neumark, "Effect of electron-hole correlation on acoustic phonon broadening of bound exciton spectra," *Applied Physics Letters*, vol. 65, no. 6, pp. 761–763, 1994.
- [124] Y. Zhang, B. Fluegel, A. Mascarenhas, H. Xin, and C. Tu, "Optical transitions in the isoelectronically doped semiconductor GaP:N: An evolution from isolated centers, pairs, and clusters to an impurity band," *Physical Review B*, vol. 62, no. 7, pp. 4493–4500, 2000.
- [125] H. W. Seo, S. Y. Bae, J. Park, M. I. Kang, and S. Kim, "Nitrogen-doped gallium phosphide nanowires," *Chemical Physics Letters*, vol. 378, pp. 420–424, 2003.
- [126] B. K. Meyer, H. Alves, D. M. Hofmann, W. Kriegseis, D. Forster, F. Bertram, J. Christen, A. Hoffmann, M. Straßburg, M. Dworzak, U. Haboeck, and A. V. Rodina, "Bound exciton and donor-acceptor pair recombinations in ZnO," *Physica Status Solidi (B)*, vol. 241, pp. 231–260, Feb. 2004.
- [127] B. Monemar, P. P. Paskov, J. P. Bergman, G. Pozina, A. A. Toropov, T. V. Shubina, T. Malinauskas, and A. Usui, "Transient photoluminescence of shallow donor bound excitons in GaN," *Physical Review B*, vol. 82, p. 235202, Dec. 2010.
- [128] L. Wang and N. C. Giles, "Temperature dependence of the free-exciton transition energy in zinc oxide by photoluminescence excitation spectroscopy," *Journal of Applied Physics*, vol. 94, no. 2, pp. 973–978, 2003.

References

- [129] R. Benzaquen, R. Leonelli, and a. P. Roth, "Temperature dependence of the shallow-donor bound-exciton-emission linewidth in high-purity InP," *Physical Review B*, vol. 52, no. 3, pp. 1485–1488, 1995.
- [130] P. Dean, R. Faulkner, S. Kimura, and M. Ilegems, "Optical Properties of Excitons Bound to Neutral Acceptors in GaP," *Physical Review B*, vol. 4, no. 6, pp. 1926–1944, 1971.
- [131] G. Bulgarini, M. E. Reimer, T. Zehender, M. Hocevar, E. P. A. M. Bakkers, L. P. Kouwenhoven, and V. Zwiller, "Spontaneous emission control of single quantum dots in bottom-up nanowire waveguides," *Applied Physics Letters*, vol. 100, no. 12, p. 121106, 2012.
- [132] P. Dawson, K. Moore, G. Duggan, H. Ralph, and C. Foxon, "Unambiguous observation of the 2s state of the light- and heavy-hole excitons in GaAs-(AlGa)As multiple-quantum-well structures," *Physical Review B*, vol. 34, no. 8, 1986.
- [133] M. De Luca, A. Polimeni, M. Felici, A. Miriametro, M. Capizzi, F. Mura, S. Rubini, and F. Martelli, "Resonant depletion of photogenerated carriers in InGaAs/GaAs nanowire mats," *Applied Physics Letters*, vol. 102, no. 17, pp. 1–5, 2013.
- [134] R. Elliott, "Intensity of optical absorption by excitons," *Physical Review*, vol. 108, no. 4, pp. 1384–1389, 1957.
- [135] F. Yang, M. Wilkinson, E. Austin, and K. O'Donnell, "Origin of the Stokes shift: a geometrical model of exciton spectra in 2D semiconductors," *Physical Review Letters*, vol. 70, no. 3, pp. 323–326, 1993.
- [136] M. Gurioli, A. Vinattieri, J. Martinez-Pastor, and M. Colocci, "Exciton thermalization in quantum well structures," *Physical Review B*, vol. 50, no. 16, 1994.
- [137] B. Piccione, C.-H. Cho, L. K. van Vugt, and R. Agarwal, "All-optical active switching in individual semiconductor nanowires.," *Nature nanotechnology*, vol. 7, pp. 640–5, Oct. 2012.
- [138] M. A. Zimmler, F. Capasso, S. Müller, and C. Ronning, "Optically pumped nanowire lasers: invited review," *Semiconductor Science and Technology*, vol. 25, pp. 1–12, Feb. 2010.
- [139] K. Madingoane, *A Bragg grating Fabry-Perot filter for next-generation broadband wireless local area networks*. PhD thesis, 2003.
- [140] C. Klingshirn, *Semiconductor optics*. third ed., 2006.
- [141] G. Ghosh, "Sellmeier coefficients and dispersion of thermo-optic coefficients for some optical glasses," *Applied Optics*, vol. 36, p. 1540, Mar. 1997.
- [142] T. S. Moss, "Relations between the Refractive Index and Energy Gap of Semiconductors," *Physica Status Solidi (B)*, vol. 131, pp. 415–427, Oct. 1985.
- [143] G. Chen, J. Wu, Q. Lu, H. R. Gutierrez, Q. Xiong, U. V. Park, and V. Pennsylv, "Optical Antenna Effect in semiconducting nanowires," *Nano letters*, vol. 8, no. 5, pp. 1341–1346, 2008.
- [144] K. Iizuka, *Engineering Optics*. Springer, third ed., 2008.

-
- [145] M. Lin, B. Sverdlov, S. Strite, H. Morkoc, and A. Drakin, "Refractive indices of wurtzite and zinblende GaN," *Electronics Letters*, vol. 29, no. 20, pp. 1759–1761, 1993.
- [146] N. Anttu, S. Lehmann, K. Storm, K. A. Dick, L. Samuelson, P. M. Wu, and M.-E. Pistol, "Crystal phase-dependent nanophotonic resonances in InAs nanowire arrays," *Nano letters*, vol. 14, pp. 5650–5, Oct. 2014.
- [147] Y. Li, S. You, M. Zhu, L. Zhao, W. Hou, T. Detchprohm, Y. Taniguchi, N. Tamura, S. Tanaka, and C. Wetzel, "Defect-reduced green GaInN/GaN light-emitting diode on nanopatterned sapphire," *Applied Physics Letters*, vol. 98, no. 15, pp. 151102–1–3, 2011.
- [148] U. V. Desnica, "Doping limits in II-VI compounds - challenges, problems and solutions," *Progress in Crystal Growth and Characterization*, vol. 36, no. 4, pp. 291–357, 1998.
- [149] J. H. Oh, J. R. Oh, H. K. Park, Y.-G. Sung, and Y. R. Do, "Highly-efficient, tunable green, phosphor-converted LEDs using a long-pass dichroic filter and a series of orthosilicate phosphors for tri-color white LEDs," *Optics express*, vol. 20, no. 1, pp. 1–12, 2012.
- [150] S.-G. Shen and X.-Q. Fan, "Lattice and electronic structure properties of semiconducting alloy Lattice and electronic structure properties of GaAs_{1-x}P_x semiconducting alloy," *Journal of physics: Condensed matter*, vol. 8, no. 24, pp. 4369–4379, 1996.
- [151] A. Standing, S. Assali, L. Gao, M. A. Verheijen, D. van Dam, Y. Cui, P. H. L. Notten, J. E. M. Haverkort, and E. P. A. M. Bakkers, "Efficient Water Reduction with Gallium Phosphide Nanowires," *Nature communications*, vol. Accepted, 2015.
- [152] M. Malizia, B. Seger, I. Chorkendorff, and P. C. K. Vesborg, "Formation of a p-n heterojunction on GaP photocathodes for H₂ production providing an open-circuit voltage of 710 mV," *Journal of Materials Chemistry A*, vol. 2, no. 19, p. 6847, 2014.
- [153] A. Bott, "Electrochemistry of Semiconductors," *Current separation*, vol. 17, no. 3, pp. 87–91, 1998.
- [154] R. van de Krol and M. Gratzel, *Photoelectro-chemical hydrogen production*. 2012.
- [155] S. S. Iyer and Y.-H. Xie, "Light Emission from Silicon," *Science*, vol. 260, pp. 40–46, 2012.
- [156] A. De and C. E. Pryor, "Electronic structure and optical properties of Si, Ge and diamond in the lonsdaleite phase," *Journal of Physics-Condensed Matter*, vol. 26, p. 16, 2014.
- [157] J. D. Joannopoulos and M. L. Cohen, "Electronic Properties of Complex Crystalline and Amorphous Phases of Ge and Si. I. Density of States and Band Structures," *Physical Review B*, vol. 7, no. 6, pp. 2644–2657, 1973.
- [158] D. Shiri, A. Verma, C. R. Selvakumar, and M. P. Anantram, "Reversible Modulation of Spontaneous Emission by Strain in Silicon Nanowires," *Scientific Reports*, vol. 2, 2012.

References

- [159] G. Signorello, E. Lörtscher, P. a. Khomyakov, S. Karg, D. L. Dheeraj, B. Gotsmann, H. Weman, and H. Riel, “Inducing a direct-to-pseudodirect bandgap transition in wurtzite GaAs nanowires with uniaxial stress,” *Nature communications*, vol. 5, no. 7491, p. 3655, 2014.

List of abbreviations

VLS	vapor-liquid-solid
NW	nanowire
WZ	wurtzite
ZB	zinc blende
ML	monolayer (III-V atoms pair)
MOVPE	metalorganic vapor phase epitaxy
TMG	tri-methyl Gallium
EBL	electron beam lithography
SEM	scanning electron microscopy
HRTEM	high resolution transmission electron microscopy
FFT	fast Fourier transform
HAADF	high angle angular dark field
EDX	energy-dispersive X-ray spectroscopy
XRD	X-ray diffraction
CPQW	crystal phase quantum well
PL	photoluminescence spectroscopy
PLE	photoluminescence excitation spectroscopy
IQE	internal quantum efficiency
NRE	non-radiative efficiency
FP	Fabry-Pérot cavity
PEC	photoelectrochemical

Summary

Pure crystal phase nanowires: growth and optical properties

Band gap engineering in semiconductors is obtained by changing the chemical composition of the material, which results in strain at the interface between the different materials. In nanowires, strain is relaxed in the radial direction, avoiding the formation of defects and dislocations. This allows the combination of III-V materials with different lattice constant within the same nanowire. In addition, the possibility to change the crystal structure from zinc blende (ZB) to wurtzite (WZ) during the nanowire growth has a large effect on the opto-electrical properties of the semiconductors. Gallium phosphide (GaP) has an indirect band gap in the green range of the visible spectrum when the material is grown in the ZB crystal structure, which severely limits its use for visible LEDs. However, theoretical band structure calculations for GaP predict a direct band gap when this material is grown with the WZ crystal structure.

In this thesis, we demonstrate for the first time the growth of GaP nanowires with high-purity WZ crystal phase and we investigate the optical properties of WZ GaP. The nanowires are grown from arrays of gold nanoparticles patterned over the GaP substrate using the vapor-liquid-solid (VLS) method in a metalorganic vapor phase epitaxy (MOVPE) reactor. The high growth temperature of 750°C and the low V/III ratio of the precursor gases flow are the key parameters in achieving the pure WZ structure of the wires, as discussed in chapter 4. A wider band gap ternary AlGaP shell is grown around the GaP core to suppress possible undesirable surface effects, which could affect the optical properties of the nanowires.

WZ GaP nanowires could be used as building blocks for the solid state quantum systems. The control of the switch between the WZ and the ZB crystal structures in the nanowires over an atomic scale has been investigated in chapter 5. Atomically sharp and defect-free transitions between the WZ/ZB/WZ crystal structures result in the formation of crystal phase quantum well (CPQW) along the nanowire length. The pure ZB segment in a WZ wire is grown by lowering the temperature to 600°C and using a high V/III ratio, while the length of the ZB segment is controlled by the flow and supply time of the Ga precursor. Similar control is obtained for the WZ growth at 750°C. The growth kinetics of the crystal phase switch are interpreted based on the nucleation model that predicts nucleation at the triple phase line for the WZ, and nucleation at the center of

the droplet for the ZB. With this knowledge, a WZ/ZB superlattice with constant segment length is obtained.

The optical properties of WZ GaP are studied in detail in chapter 6 by performing low-temperature photoluminescence (PL), time-resolved PL, and photoluminescence excitation (PLE) spectroscopy measurements. The high emission intensity, the striking difference in the WZ-ZB lifetimes, and the very good agreement between the experimental and predicted WZ GaP band gap values, strongly suggest the presence of direct band gap transitions in the WZ GaP nanowires. We assign the recombination peak at 2.088 eV as donor-acceptor pair (DAP), while the emission ranging between 2.15 and 2.25 eV as Burstein-Moss band-filling continuum. Moreover, the sharp A- and B-lines emission lines at 2.140 eV and 2.164 eV, respectively, are identified as bound excitons of the direct band gap, with both TA and LO/TO phonon sidebands, and a long lifetime. Instead, the narrow C-line at 2.252 eV with a fast recombination lifetime has the character of a free exciton. Furthermore, we provide experimental indication of the A-, B-, and C-peaks are the excitonic peaks related to the transitions from the three valence bands into the Γ_{8c} conduction band predicted from the band structure calculations of WZ GaP.

The excellent wave-guiding properties of the WZ wire are shown in chapter 7. From the spacing of the Fabry-Pérot cavity modes we estimated the value for the dielectric constant of WZ GaP at 550 nm of $\epsilon = 15 \pm 1$.

In the final chapter 8, we illustrate possible applications of WZ GaP nanowires. The direct band gap of WZ GaP wires is promising for visible LEDs and for photoelectrochemical (PEC) cells for hydrogen production. Tunability of the optical emission across the visible range is achieved by using ternary AlGaP and GaAsP nanowires, providing an important feature for new generation LEDs and PEC devices. Solar water splitting for hydrogen production is demonstrated using p-type WZ GaP wires, achieving a new record efficiency for this material with respect to bulk samples. Furthermore, the lattice match between GaP and Silicon allows epitaxial growth and crystal structure transfer when grown in a core/shell nanowire structure. The growth of core/shell WZ GaP/Si nanowires is shown, reducing the distance between the integration of Silicon with photonics.

Acknowledgements

Team work is the key factor for achieving high quality scientific results. This thesis could not be done without the help of many people, which shared the knowledge in their field of research to improve my own expertise. I would like to take this chance to acknowledge all the persons that contributed to this thesis and supported me across the past four years.

First of all, I would like to thank my promoter and daily supervisor prof. Erik P.A.M. Bakkers, for the great opportunity of working in a top-level research laboratory. Dear Erik, when I started my PhD the nanowire field was completely new to me, but thanks to your guidance I managed to gain knowledge and confidence in my work day by day. I will never forget the countless amount of time spent discussing in your office, during which I always learned something new that could improve my research. No matter how busy you were, you always spared some time to discuss the latest results of my project. In my mind I couldn't think of a better way of supervising me, I'll always be grateful to you for your personal support during those years.

I would like to thank the defense committee for the evaluation of my dissertation: my copromotor dr. Jos Haverkort, prof. Lars Samuelson, prof. Carsten Ronning, prof. Jordi Arbiol, prof. Andries Meijerink, and prof. Andrea Fiore. I'm very grateful for the time you spent in reading my thesis, providing valuable comments that improved the quality of my dissertation.

My thesis wouldn't be the same without the support of dr. Jos Haverkort and dr. Ilaria Zardo with the optical measurements, in particular in the interpretation of the optical data. I can only say thank you, we had tough times in understanding the puzzling optical emission from my samples, but meeting after meeting all our efforts provided very good results.

The TEM measurements largely contributed to my thesis. This was only possible thanks to the infinite time that dr. Marcel Verheijen spent in analyzing my samples. Marcel, the weekly discussions with you were always a source of new ideas to test, and new samples to grow, even knowing that this would result in more time for you in front of the TEM.

My gratitude goes to dr. Sébastien Plissard for supervising me with the development of the nanowire growth. During our discussions I learned many tricks to improve the nanowire growth, always in a joyful atmosphere, we had a lot of fun working together.

I would like to thank all the people that helped in many different aspects of my project. Thanks to dr. Moira Hocesvar for sharing with me her knowledge on the EBL patterning, and for introducing me into the nanowire growth; thanks to René van Veldhoven, my research would have not been possible without having the MOVPE reactor in a perfect condition, and without your advices on the growth recipes; thanks to Yingchao Cui and Luca Gagliano for the nanoimprint patterning; thanks to the nanowire growers Luca Gagliano, Alessandro Cavalli, dr. Ang Li, dr. Jia Wang, Diana Car, Ikaros Hauge, and Tilman Zehender, we had a lot of fun in keeping a busy schedule of the MOVPE and in discussing our growths; thanks to dr. Thuy Vu for your help with the PL setup and for your work on the CPQW, together with Maaïke Bavinck, dr. Klaus Jöns, and dr. Nika Akopian; thanks to my master students Giovanni Giuliano and Michiel de Moor, you did a great work in the development of the PLE setup, solving the bugs of the LabView code and aligning the excitation source; thanks to Dick van Dam for your help in understanding the Fabry-Pérot modes; thanks to dr. Johannes Greil for helping me to give more insight in the optical properties of WZ GaP; thanks to dr. Sonia Conesa-Boj for the TEM studies on the hexagonal Si shell, and for the discussions on the TEM images; thanks to dr. Dominik Kriegner for the XRD measurements; thanks to dr. Francesco Pagliano for showing me the art of aligning the optical setups; thanks to Anthony Standing for your work on the PEC and your amazing PDMS samples; thanks to Douglas Oliveira for the deep understanding that you provided to our work on the crystal phase control; thanks to dr. Lou-Fé Feiner for the chance to correlate my growth experiments with your nucleation model, which provided me a greater knowledge of the nanowire growth; thanks to prof. Friedhelm Bechstedt and dr. Abderrezak Belabbes for the band structure calculations. My gratitude goes to prof. Paul Koenraad, prof. Andrea Fiore, dr. Rob van der Heijden, and dr. Andrei Silov for their support in my research and for the opportunity in the discussions. Additional thanks to Luca, Alessandro, Ang, and Milo Swinkels, we spent so much time together in the cleanroom and labs, late in the evenings and in the weekends, always helping me when it was needed.

The working environment plays a big role in a PhD project, and I couldn't ask for a better group than the PSN. The excellent work of our PSN secretaries Margriet, Annebee, Simone, and Thérèse-Anne created a great atmosphere, further improved by the successful organization of the group outing events. I would like to thank all the present and past members of the PSN group: Leonardo, Davide, Maurangelo, Rianne, Sebastian, Michele, Sasa, Zarko, Giulia, Rosalinda, Erwin, Tian, Zili, Sartoon, Simone, Joost, Christian, Bruno, and many others. Additional thanks to Juanita for your support over the past years. I wish to all of you all the best with your working career and success in life!

Finally, my biggest gratitude goes to my family, for their love and support during all these years, I would have not managed to achieve my doctoral degree without their encouragement.

List of publications

Journal publications:

- A. Standing, S. Assali, L. Gao, M.A. Verheijen, D. van Dam, Y. Cui, P.H.L. Notten, J.E.M. Haverkort, and E.P.A.M. Bakkers, "Efficient water reduction with Gallium Phosphide nanowires", *Nature Communications*, *accepted*.
- H. I. Hauge, M.A. Verheijen, S. Conesa-Boj, T. Etzelstorfer, M. Watzinger, D. Kriegner, I. Zardo, C. Fasolato, F. Capitani, P. Postorino, S. Kölling, A. Li, S. Assali, J. Stangl, and E.P.A.M. Bakkers, "Hexagonal silicon realized", *under review*.
- S. Assali, L. Gagliano, D.S. Oliveira, M.A. Verheijen, L.F. Feiner, S. Plissard, and E.P.A.M. Bakkers, "Decoding crystal phase switching in nanowires", *submitted*.
- S. Assali, J.E.M. Haverkort, M. de Moor, A. Belabbes, F. Bechstedt, I. Zardo, and E.P.A.M. Bakkers, "Photoluminescence of WZ GaP", *in preparation*.
- S. Assali, T.T.T. Vu, M.A. Verheijen, J.E.M. Haverkort, and E.P.A.M. Bakkers, "Crystal phase quantum well emission with digital control", *in preparation*.
- S. Conesa-Boj, H.I.T. Hauge, M. A. Verheijen, S. Assali, A. Li, E.P.A.M. Bakkers, and A. Fontcuberta i Morral, "Cracking the Si shell growth in hexagonal GaP-Si core-shell nanowires", *Nano Letters* 15, 2974-2979 (2015).
- S. Assali, I. Zardo, S. Plissard, D. Kriegner, M.A. Verheijen, G. Bauer, A. Meijerink, A. Belabbes, F. Bechstedt, J.E.M. Haverkort, and E.P.A.M. Bakkers, "Direct band gap wurtzite gallium phosphide nanowires", *Nano letters* 13, 1559-1563 (2013).
- A. Standing, S. Assali, J.E.M. Haverkort, and E.P.A.M. Bakkers, "High yield transfer of ordered nanowire arrays into transparent flexible polymer films", *Nanotechnology* 23, 495305 (2012).

Additional journal publications (not included in this thesis):

- P. Peddibhotla, F. Xue, H.I.T. Hauge, S. Assali, E.P.A.M. Bakkers, and M. Poggio, "Harnessing nuclear spin polarization fluctuations in a semiconductor nanowire", *Nature Physics* 9, 631-635 (2013).
- D. Kriegner, S. Assali, A. Belabbes, T. Etzelstorfer, V. Holy, T. Schüllli, F. Bechstedt, E.P.A.M. Bakkers, G. Bauer, and J. Stangl, "Unit cell structure of the wurtzite phase of GaP nanowires: X-ray diffraction studies and density functional theory calculations", *Physical Review B* 88, 115315 (2013).
- J. Franc, E. Belas, M. Bugár, P. Hlídek, R. Grill, G. Yang, A. Cavallini, B. Fraboni, A. Castaldini and S. Assali. "Semi insulating CdTe:Cl after elimination of inclusions and precipitates by post grown annealing", *Journal of Instrumentation* 7, C11001 (2012).

US patent:

- S. Assali, I. Zardo, J.E.M. Haverkort, and E.P.A.M. Bakkers, "Direct band gap wurtzite semiconductor nanowires", US 20140230720 A1

Conference proceedings:

- S. Assali, D. Kriegner, I. Zardo, S.R. Plissard, M.A. Verheijen, J. Stangl, J.E.M. Haverkort, and E.P.A.M. Bakkers, "Direct band gap wurtzite GaP nanowires for LEDs and quantum devices", *Conference proceeding SPIE Optics+Photonics* (2014).
- S. Assali, I. Zardo, S. Plissard, M.A. Verheijen, J.E.M. Haverkort, and E.P.A.M. Bakkers, "Wurtzite Gallium Phosphide has a direct-band gap", *International conference on Indium Phosphide and related materials (IPRM)* (2013).

Curriculum vitae

Simone Assali was born on 20-08-1987 in Reggio Emilia (Italy).

After finishing Scientific-Technological Lyceum in 2006 at I.I.S. L. Nobili in Reggio Emilia (Italy), he studied Physics at Alma mater studiorum - University of Bologna (Italy). In 2011 he graduated within the Physics of Defects in Semiconductors group on the opto-electrical properties of CdTe detectors.

From September 2011 he started a PhD project at TU/e Eindhoven (Netherlands) of which the results are presented in this dissertation. Since 2011 he is employed at TU/e Eindhoven.

He obtained the scholarship from the Italian Physical Society (SIF) for the academic years 2006-2009.

